# Quantum effects in ultracold collisions of atoms, ions, and molecules

DARIUSZ WIATER

University of Warsaw
Faculty of Physics

Doctor of Philosophy Dissertation

Thesis supervisor:
dr hab. Michał Tomza prof. univ.

Warsaw, December 2022

# ABSTRACT

The doctoral dissertation presents the results of research on the physics of ultracold collisions in systems involving atoms, ions and molecules. The work starts with a historical outline and main results obtained in this field. Then the assumptions of the experiments are presented, which were part of the research work carried out at the stage of preparing the dissertation. In particular, the experiment concerning the first cooling of the mixture of ytterbium ion with lithium atoms to the quantum regime performed in Amsterdam and the results of theoretical research, which guided and confirmed experimental measurement and allowed for the correct interpretation. Moreover, the dissertation presents the path that led to the confirmation of the fact of obtaining ion-tom collisions at a temperature corresponding to the observation of quantum effects, including determination of previously unknown scattering lengths. The second part presents the experiment concerning the first observation of Feshbach resonances in the barium ion system with lithium atoms performed in Freiburg along with the process of estimation the position of resonances, determination of the correct combination of scattering lengths, the number and nature of the observed resonances. Both projects were crucial for the development of the hybrid ion-atom quantum systems and, like in the past, the first cooling of atoms to quantum temperatures opened up a new field of research. The last part presents the analytical calculations of atom-molecule scattering carried out using an anisotropic pseudopotential. The method of an effective potential preserving the mathematical properties of the original interaction was commonly used in the past to the interactions of atoms and allows to gain insight into the nature of the atom-molecule interaction and creates a prerequisite for testing systems with the rotating impurity.

# PUBLICATIONS

Some ideas and figures presented in this thesis have appeared previously in the following publications:

[1] T. Feldker, H. Fürst, H. Hirzler, NV Ewald, M. Mazzanti, D. Wiater, M. Tomza, R. Gerritsma, "Buffer gas cooling of a trapped ion to the quantum regime", **Nature Physics** 16, 413–416 (2020)

[2] P. Weckesser, F. Thielemann, D. Wiater, A. Wojciechowska, L. Karpa, K. Jachymski, M. Tomza, T. Walker, T. Schaetz, "Observation of Feshbach resonances between a single ion and ultracold atoms", **Nature** 600, 429–433 (2021)

Other publications of the author not included in the thesis:

[3] D. Wiater, J. Zakrzewski, "Impact of geometry on many-body localization", **Physical Review B**, 094202 (2018)

[4] D. Wiater, T. Sowiński, J. Zakrzewski, "Two bosonic quantum walkers in one-dimensional optical lattices", **Physical Review A** 96, 043629 (2017)

# ACKNOWLEDGEMENTS

I would like to thank all members of the Quantum Molecular Systems group at the University of Warsaw, with whom I had the opportunity to cooperate and discuss. Especially Michał Tomza, group leader and doctoral dissertation supervisor, for support in scientific research, development opportunities and involvement in international projects. As well as for support in participation in conferences and scientific schools and guidance in applying for research grants.

Thanks to our collaborators from the experimental groups in Amsterdam and Freiburg. Without these wonderful experiments, it would not have been possible to obtain such significant results. Special thanks to Prof. Rene Gerritsma for hosting me during an internship at the University of Amsterdam and the whole group for a great atmosphere.

Thanks to the physicists from the Jagiellonian University and the Polish Academy of Sciences, with whom I had the opportunity to study physics, collaborate, discuss science and many other topics, and participate in conferences and schools together.

Thanks to all the people who were with me, had conversations, spent time during my studies and PhD both in Krakow and Warsaw.

Acknowledgements for the financial support from the National Science Centre Poland (Etiuda grant: 2020/36/T/ST2/00591).

# CONTENTS

# LIST OF FIGURES

---

# LIST OF TABLES

---

# Part I

# ULTRACOLD ATOMS AND IONS

The physics of systems composed of cold atoms, molecules and ions has become a fashionable subject of research in the last twenty years. The field was established at the intersection of atomic physics, solid state physics, quantum optics and quantum information. Modern research is devoted to building solutions and models that can play the role of future quantum technologies. The first part of the doctorate will be an overview of achievements in the field.

# 1

# INTRODUCTION

This thesis covers the topic of the impurity immersed in the gas of cold atoms. In general, the impurity may be an additional atom, molecule, or ion. However, in our case, we will limit ourselves to ions and molecules. The following two types of systems were the subject of the research and will be discussed in this work:

- a single ion immersed in a cloud of ultracold atoms ($\mathrm{Yb}^+/\mathrm{Li}$ and $\mathrm{Ba}^+/\mathrm{Li}$ mixtures)
- a molecule interacting with an atom

The first of the discussed systems was the subject of research together with experimental groups at the University of Amsterdam and the University of Freiburg. The theoretical research was aimed at guiding, explaining and confirming the effects observed in the experiments and conducted in close theoretical-experimental collaboration. The project carried out with the group from Amsterdam (Prof. Rene Gerritsma) concerned the first ever observation of ion-atom collisions in a quantum regime. It was the first time that an ion could be cooled to such low temperatures. The independent project in cooperation with the group from Freiburg (Prof. Tobias Schaetz) was related to the first ever observation of Feshbach resonances in ion-atom systems. From a theoretical point of view, it involved finding resonance positions and exploring additional effects such as spin-orbit coupling.

The second of the considered systems: single atom and molecule was the subject of research from the point of view of potential application to rotating impurities, as a prerequisite for the study of the few-body physics.

This work is divided into chapters. The first, *ultracold atoms and ions*, describes the overall context in which the work is embedded and the most important achievements in the field. The second chapter: *ion-atom interaction and scattering theory* explains the theoretical methods used in the research. The third chapter: *experiments with ion-atom systems* describes the details of the experimental systems that were built in Amsterdam and Freiburg, along with a description of the techniques that are used in the field. Chapter four: *results* contains a theoretical analysis of the studied systems together with an explanation of the processes taking place in them.

## 1.1 ULTRACOLD ATOMS

The emergence of the field of research called ultracold atom physics was the result of many years of development of atomic physics, solid state physics, quantum optics and experimental methods, in particular cooling techniques [1–5]. The development of this field of research was a spectacular event in the 90s, it was met with Nobel prizes for cooling techniques (1997 - Steven Chu, Claude Cohen-Tannoudji, William D. Phillips) or obtaining Bose-Einstein condensate (2001 - Eric Cornell, Carl Wieman, Wolfgang Ketterle). For the first time, it has become possible to think seriously about quantum technologies, quantum simulators and quantum engineering. Over the years, many different arrangements of atoms, ions and molecules have been studied. New experimental configurations were investigated as well as the fundamental laws of quantum mechanics and quantum optics. The physics of cold atoms became a kind of laboratory where it was possible to test ideas from both solid state physics and field theory or the theory of relativity. In this context, optical lattices were particularly important, periodic structures created by laser light, where high tunability allowed with the help of cold atoms to test various theories, including gauge theories. Thus, the key aspect was achieving low enough temperatures to observe quantum effects and a high ability to control systems, including interactions through Feshbach resonances. In this sense, the results concerning the cooling and control of ion-atom systems presented in the work constitute a significant enhancement of the quantum toolbox that scientists have nowadays.

## 1.2 LOW-ENERGY COLLISIONS

The physics of cold atoms is played in systems that are cooled to suitably low temperatures, at least in the microkelvin range, depending on the system. Low temperature allows to achieve relatively low collision energies, which in the language of quantum mechanics translates into scattering in a few lowest partial waves, ultimately in the s-wave. Then the strictly quantum nature of the interacting atoms or molecules can be directly observed in the experiments. The scattering of two atoms in their relative motion can be described by a wave function consisting of a plane wave and a scattered wave

$$\psi = e^{ikz} + \psi_{sc}(r). \tag{1}$$

We assume that the interaction is spherically symmetric, so the scattering amplitude depends only on the scattering angle. Hence the wave function for long range has the form:

$$\psi = e^{ikz} + f(\theta)\frac{e^{ikr}}{r}. \tag{2}$$

At the limit of low energies amplitude $f(\theta)$ is constant and related to $-a$ (scattering lenght). We consider only the so-called s-wave scattering and then the above equation can be approximated:

$$\psi = 1 - \frac{a}{r}. \tag{3}$$

In the general case, the wave function can be decomposed into so-called partial waves through Lagendre polynomials[6]:

$$\psi = \sum_{l=0}^{\infty} A_l P_l(\cos\theta) R_{kl}(r), \tag{4}$$

with radial wave function satisfying the equation:

$$R''_{kl}(r) + \frac{2}{r} R'_{kl}(r) + \left[ k^2 \frac{l(l+1)}{r^2} - \frac{2m}{\hbar^2} U(r) \right] R_{kl}(r) = 0, \tag{5}$$

where $U(r)$ denotes potential and for large r:

$$R_{kl}(r) \approx \frac{1}{kr} \sin(kr - \frac{\pi}{2} l + \delta_l) \tag{6}$$

is given in terms of phase shifts $\delta_l$ and using relations between equations above we obtain amplitude:

$$f(\theta) = \frac{1}{2ik} \sum_{l=0}^{\infty} (2l+1)(e^{i2\delta_l} - 1) P_l(\cos\theta). \tag{7}$$

Using properties of the Legendre polynomials we can calculate total cross section in terms of the phase shifts:

$$\sigma = \frac{4\pi}{k^2} \sum_{l=0}^{\infty} (2l+1) \sin^2 \delta_l. \tag{8}$$

The standard Hamiltonian describing the contact interaction of N particles (which is a good approximation at low temperature) in the external potential takes the form[6]:

$$H = \sum_{i=1}^{N} \left[ \frac{p_i^2}{2m} + V(r_i) \right] + U_0 \sum_{i<j} \delta(r_i - r_j), \tag{9}$$

where V (r) is the external potential. By minimizing the energy of such a system, we obtain the famous Gross–Pitaevskii equation:

$$-\frac{\hbar^2}{2m} \nabla^2 \psi(r) + V(r)\psi(r) + U_0 |\psi(r)|^2 \psi(r) = \mu\psi(r), \tag{10}$$

where $\mu$ denotes chemical potential. The Gross–Pitaevskii equation, which is a nonlinear equation, has numerous solutions in the form of solitons, and in the regime of weakly interacting bosons it also models the wave function of the Bose-Einstein condensate which is the

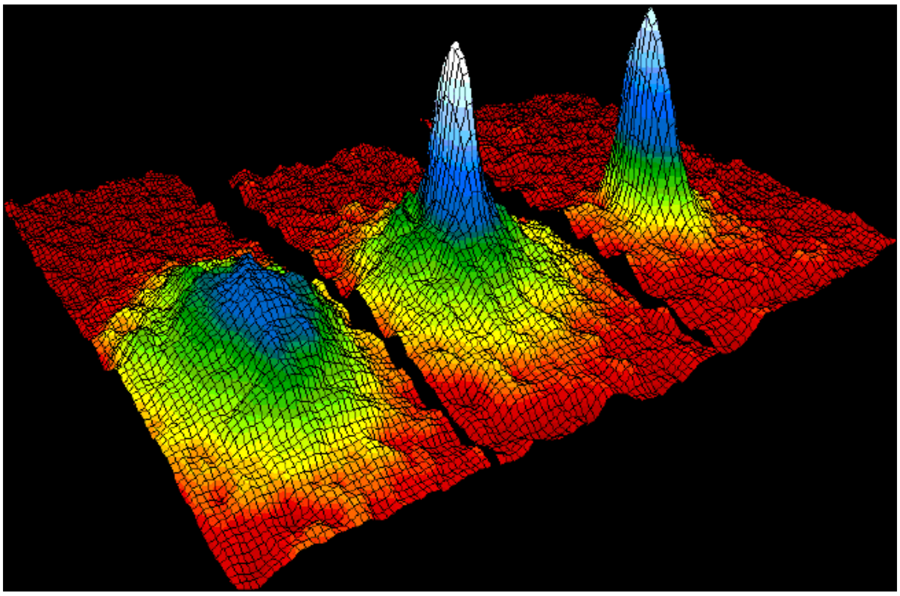

Figure 1: Bose-Einstein condensate 2d velocity distribution: from the left before condesation, in the center when BEC appeared, on the right after further evaporation nearly pure condensate. Picture from NIST/JILA/CU-Boulder materials.

macroscopic state of occupation by bosons their ground state (Fig.1). In the regime of low-energy collisions in the s-wave, an effective contact potential, which reproduces the physical properties of the real potential and provides mathematical corectness is often used. The introduced pseudopotential[7] takes the form commonly used in the field:

$$U(r)\psi = \frac{4\pi\hbar^2 a_0}{m}\delta(r)\frac{\partial}{\partial r}(r\psi). \tag{11}$$

## 1.3 ULTRACOLD GASES IN OPTICAL LATTICES

Ultracold atoms placed in optical lattices have become an fundamental tool in research conducted in the field[3, 5, 8, 9]. Optical lattices are a periodic structure formed by the interference of laser light beams (Fig.2). Periodicity is a well-known phenomenon in solid state physics, however, it is a description of specific materials. For the sake of illustration, we can assume the following form of the optical lattice potential in 3D:

$$V = \sum_{l=x,y,z} = V_{0l}\sin^2(\pi l/a), \tag{12}$$

where $a$ is a lattice constant equal half of the laser wavelength in the standing wave configuration.

In the case of optical lattice, we deal with very high tunability and the possibility of precise system control. This means that, in a

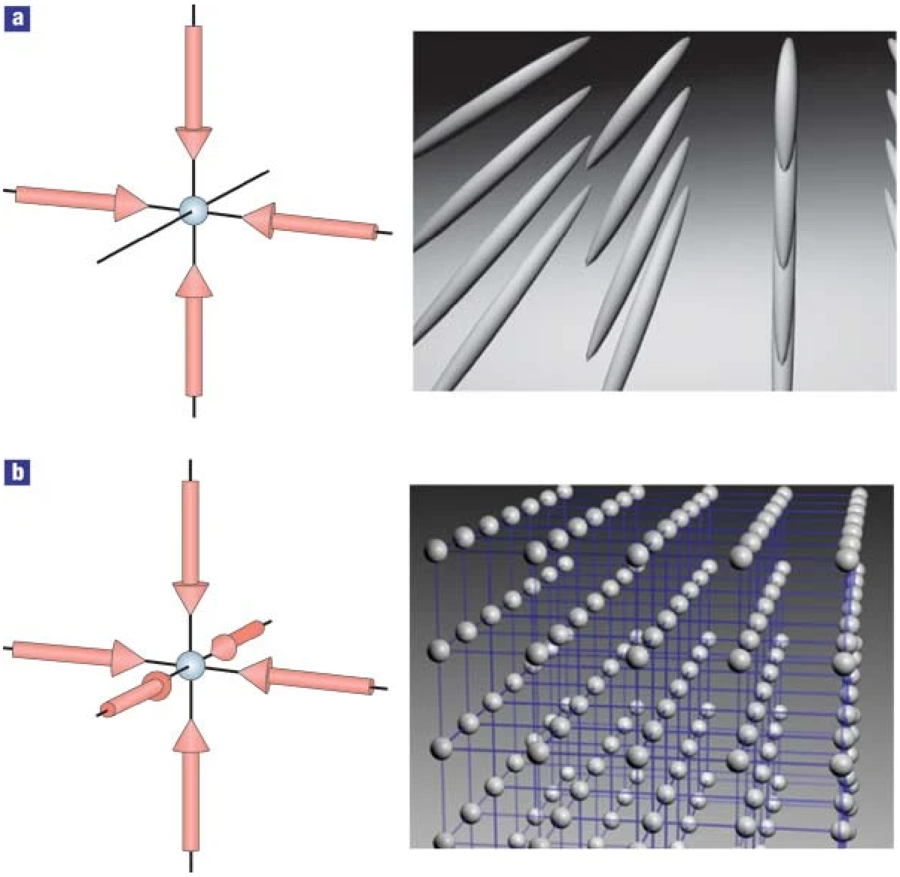

Figure 2: Optical lattice example: a. 2d example, array of tightly confining 1d potential tubes, b. 3d example, optical lattice presented as cubic array of tightly confining harmonic oscillator potentials, figure from Ref.[8]

sense, we can design systems consisting of a selected type of atoms, molecules and control the distance between them. Ultracold, weakly interacting gases placed in an optical lattice can therefore simulate models describing solid state physics systems, such as Hubbard for fermions or Bose-Hubbard model for bosons. These systems exhibit the same characteristics as solid-state systems, for example: band structure and Bloch oscillations. Standard Bose-Hubbard Hamiltonian describes hoping between adjacent sites and the interaction between bosons at ith site

$$H = -J \sum_{<i,j>} \hat{b}_i^\dagger \hat{b}_j + \frac{U}{2} \sum_i \hat{n}_i(\hat{n}_i - 1) - \mu \sum_i \hat{n}_i. \tag{13}$$

The interaction between atoms can be controlled by experimental techniques such as Feschbach resonances[4], which will be discussed in detail in the following chapters. Nevertheless, it is important that they allow to change the interactions from attractive to repulsive and, consequently, to implement many states of the model. The standard interactions between atoms are low-energy contact $\delta$ interactions in the s-wave like in the previous paragraph. Likewise, we can implement a similar model for fermions, keeping in mind the Pauli exclusion principle. In the case of fermions, the interaction in the lattice site takes place between fermions with opposite spin

$$H = -J \sum_{<i,j>,\sigma} \hat{f}^{\dagger}_{i\sigma} \hat{f}_{j\sigma} + \frac{U}{2} \sum_{i} \hat{f}^{\dagger}_{i\uparrow} \hat{f}^{\dagger}_{i\downarrow} \hat{f}_{i\downarrow} \hat{f}_{i\uparrow} - \mu \sum_{i,\sigma} \hat{f}^{\dagger}_{i,\sigma} \hat{f}_{i,\sigma}. \qquad (14)$$

Hubbard model for both fermions and bosons can be extended with additional effects such as pair tunneling, density dependent tunneling or nearest-neighbours interaction.

The realization of optical lattices and the ability to control them also played an important role in the study of the disorder. Beginning with the theoretical foundations of the Anderson localization[10], consisting in the disappearance of diffusion in a system with some forms of disorder and later implementations of this concept in experiments with Bose-Einstein condensate[11, 12]. Coming to the many-body localization [13–15], the state of interacting particles subjected to the disorder, which causes the lack of thermalization in the system, and thus the system will remain in a non-equilibrium initial state[16]. Finally, the phenomenon of the many-body localization was observed in the experiment with ultracold fermions in the optical lattice[17], there were also concepts of models in the optical lattices with random interactions[18], or in other geometries[19, 20].

## 1.4 FEW-BODY PHYSICS

The physics of few-body systems itself, as well as the crossover between few and many bodies[21], is one of the important topics of research in the field of cold atoms. Beginning with the famous theoretical work on two cold atoms in a harmonic trap[22], there have been many subsequent studies extending this research to more particles: bosons and fermions or molecules[23, 24]. At the same time, great experimental progress in the possibilities of controlling cold atomic gases as well as individual few-body systems took place[25–28]. In this context, the use of optical tweezers[29] is also worth mentioning, especially the experiment of creating a single molecule from two atoms[30].

The systems of few bodies are theoretically described by Hamiltonians, which in terms of the second quantization have the form:

$$\begin{aligned} H = \sum_{\sigma} \int dx \psi^{\dagger}_{\sigma}(x) \left( -\frac{\hbar^2}{2m} \frac{\partial^2}{\partial dx^2} + \frac{1}{2} m \omega^2 x^2 \right) \psi_{\sigma}(x) + \\ g \int dx \psi^{\dagger}_{\uparrow}(x) \psi^{\dagger}_{\downarrow}(x) \psi_{\downarrow}(x) \psi_{\uparrow}(x). \end{aligned} \qquad (15)$$

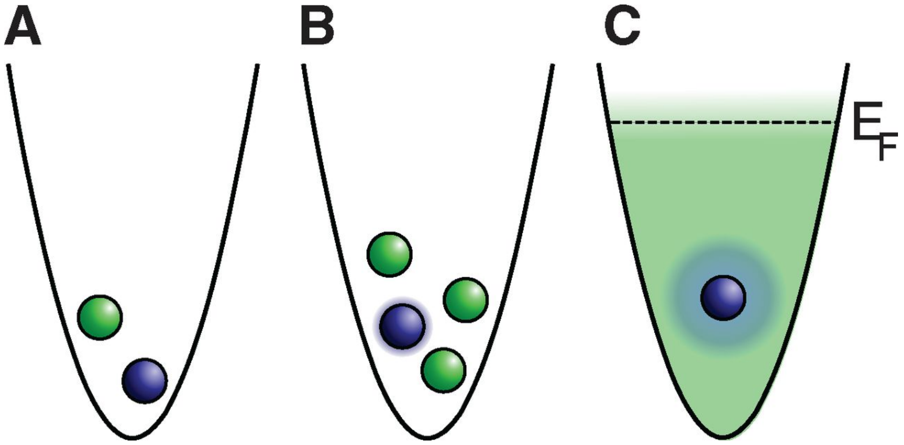

Figure 3: A single impurity (blue) interacting with one, few, and many fermions (green) in a harmonic trapping potential. In the many-body case, the majority component can be described as a Fermi sea with a Fermi energy. From Ref.[31].

In the above equation, we assume that the system is in a harmonic trap and that the particles interact in contact, which is a common assumption. We allow the occurrence of particles of different types: bosons, fermions or fermions with different spin, remembering that for fermions of the same type, the Pauli exclusion principle applies. Consequently, fermions of the same type fill successive levels in the trap, which is related to features of the system such as Fermi energy. The situation is graphically presented in Fig.3, we can see that particles of many types and different number can be present in the trap. In particular, we can imagine the situation that we have one additional particle of a different type called "impurity" in the presence of cloud of other particles.

As mentioned, few-body systems have been studied in many configurations and variants, but a typical example consists of two types of spin $1/2$ fermions. Such physical systems are studied using numerical methods like exact diagonalization and various semi-analytical methods. Calculations even for such small systems very quickly become very complex, due to the rapid increase in the size of Hilbert spaces. Fig.4 shows the energy of such fermions as a function of the strength of contact interactions. It is one of the basic numerical solutions to the few-body problem in a harmonic trap.

## 1.5 TRAPPED IONS

At this stage, it seems necessary to mention briefly the rapidly developing field of trapped ions. In the context of the work, it is crucial, because we want to draw attention to the importance of our results for cold hybrid ion-atom systems, but they would not be possible without the development of both cold atoms and ion trapping

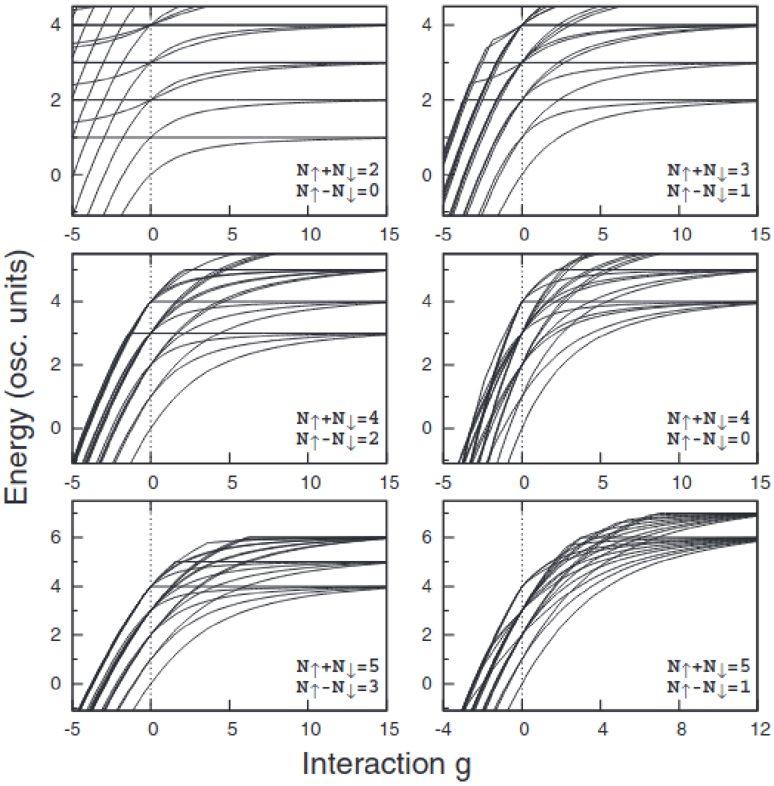

Figure 4: The energy $E - E_F$ as a function of the dimensionless interaction strength $g$ for different combinations of spin-up and spin-down particles. From Ref.[23].

independently[32]. In this sense, the reader should be aware that independent ion trapping is currently an advanced and well-developed field of science and does not present much of a challenge in good experimental groups. It is particularly interesting to note the trapped ions in the context of quantum simulations and potential quantum computers[33] whose qubits are physically represented by the electronic and hyperfine states of the ions. Qubits act as the quantum equivalent of a bit, but are more general because they can exist in states that are quantum superpositions of two base (logical) states, allowing a wider variety of algorithms that are predicted to be orders of magnitude more efficient than the classical ones. In connection with the subject of quantum computers, it is necessary to mention the achievements of the group of Prof. Rainer Blatt and his collaborators who are involved in international projects: An ion-trap quantum computer for Europe (AQTION), Quantum Information Systems Beyond Classical Capabilities: Special Research Programme (SFB) and Industrial ion traps (Piedmons). Their groundbreaking work in the past concerned, among others: Entangled states of trapped atomic ions[34], Universal Digital Quantum Simulation with Trapped Ions[35], Realization of a Quantum Walk with One and Two Trapped Ions[36], Quantum Simulation of Quantum Field Theories in Trapped Ions[37], Quantum simulation of the Dirac equation[38], 14-Qubit Entanglement: Creation and Coherence[39] and Quantum simulations with trapped ions[40].

## 1.6 IMPURITY PHYSICS

### 1.6.1 *Polaron and rotating impurity*

There is a special class of quantum systems which contains so-called "impurity". The history of impurity physics started with introduction of the polaron [41–44] which effectively describes deformation of a crystal because of electric interactions with moving electron (see Fig.5). Another examples of the importance of the impurities are Kondo effect[46] - suppression of electron transport due to magnetic impurities in metals or the Anderson orthogonality catastrophe[47]. Further research has gone beyond traditional solid state physics and became interesting also for experimentalists in ultracold quantum gases[48]. A lot of effort has been made to investigate the polaron problem which is limited to coupling between translational degrees of freedom of the quasiparticle and the bath. New ideas in this field are still under consideration and they are part of active research both in theory and experiments[49–51]. Let us mention: field-theoretical study of the Bose polaron[52], the dynamics of Bose polarons in the vicinity of a Feshbach resonance between the impurity and host atoms[53] or nonperturbative renormalization group approach to the Bose polaron strongly interacting with BEC[54]. In the last years the new idea of rotating molecular impurities has started to be considered[55, 56]. The conception of the rotating impurity is characterized by a quasiparticle called "angulon" which is a collective object consisting of a quantum rotor (molecule) immersed in an atomic gas and characterized by the total angular momentum of the system, of which it is an eigenstate. The main feature of this quasiparticle is a coupling between rotational angular momentum of the molecule and bath's rotational degrees of freedom so the angular

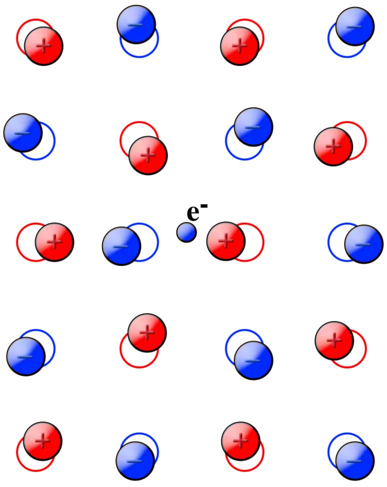

Figure 5: A conduction electron in an ionic crystal or a polar semiconductor repels the negative ions and attracts the positive ions. Figure from Ref.[45].

momentum is shared within the many-particle system. This phenomena allows for redistribution of the angular momentum between the impurity and the bath.

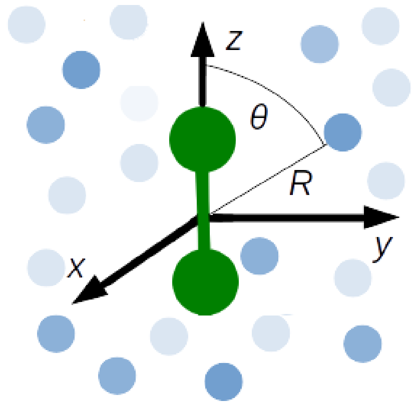

Figure 6: A rotating impurity immersed in ultracold atomic gas.

Despite the fact that angular momentum belongs to the most fundamental quantities in quantum physics, a consistent theory of the redistribution of the angular momentum has not been established yet. The theory of angulon introduced quasiparticle-based approach to the redistribution of the angular momentum between the rotating impurity and the bosonic bath. Furthermore Dr. R. Schmidt and Prof. M. Lemeshko in their work discovered completely new phenomenon without direct analog in isolated systems, namely the rotational Lamb shift and many-body-induced fine structure emerging due to the transfer of the angular momentum. The molecular impurity was immersed in a homogeneous Bose-Einstein condensate and the hamiltonian was expanded in fluctuations around a homogenous BEC of density n. The effective Hamiltonian is realized by the first term corresponding to the kinematics of the impurity and the second to the bath and the last term accounting for the absorption and emission of field quanta by the quantum rotor:

$$H = B\hat{J}^2 + \sum_{k\lambda\mu} \omega_k \hat{b}^\dagger_{k\lambda\mu}\hat{b}_{k\lambda\mu} + \sum_{k\lambda\mu} U_\lambda(k)[Y^*_{\lambda\mu}(\hat{\theta},\hat{\phi})\hat{b}^\dagger_{k\lambda\mu} + Y_{\lambda\mu}(\hat{\theta},\hat{\phi})\hat{b}_{k\lambda\mu}], \tag{16}$$

where $k = |k|$, and $\lambda$ and $\mu$ define, respectively, the phonon angular momentum and its projection onto the z axis and:

$$U_\lambda(k) = u_\lambda[8nk^2\epsilon_k/(\omega_k(2\lambda+1))]^{1/2}\int drr^2 f_\lambda(r)j_\lambda(kr) \tag{17}$$

with $j_\lambda(kr)$ the spethical Bessel function and $f_\lambda(r)$ represent the strength and the shape of the potential in the respective angular momentum channel $\lambda$. In Ref.[55] a variational anzatz for the many-body wavefunction was formulated as an expansion in the bath excitations.

$$|\psi\rangle = Z^{1/2}_{LM}|0\rangle|LM\rangle + \sum_{k\lambda\mu jm} \beta^{LM}_{k\lambda j} C^{LM}_{jm\lambda\mu}\hat{b}^\dagger_{k\lambda\mu}|0\rangle|jm\rangle, \tag{18}$$

where $Z_{LM} = 1 - \sum_{k\lambda}|\beta^{LM}_{k\lambda j}|^2$ and $|0\rangle$ is the the vacuum of bath excitations. Furthermore $L^2|\psi\rangle = L(L+1)|\psi\rangle$ and $L_z|\psi\rangle = M|\psi\rangle$. The properties of the angulon were studied[55, 56] using the spectral function defined by the the retarded Green's function: $A_L = \Im[G_L^{ret}(E)]$. Results are presented in Fig. 2.2. Due to anisotropic molecule-boson intereaction we observe specific for the angulon additional shift whose magnutude depends on L. This effect was called "Rotational Lamb shift" and presented in Fig.7 as $\tilde{\Delta}_L^{RLS} = (E_L - E_0)/B - L(L+1)$.

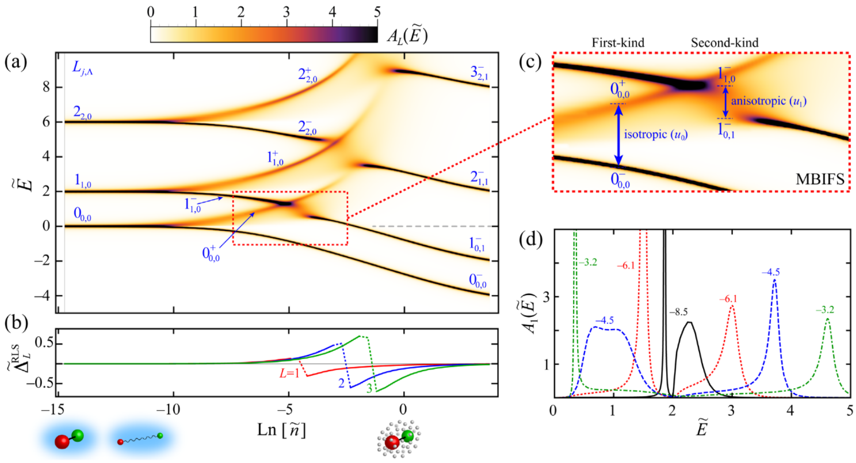

Figure 7: Characteristic of the angulon taken from Ref.[55] (a) The angulon spectral function, $A_L(\tilde{E})$ as a function of the dimensionless density, $\tilde{n} = n(mB)^{-3/2}$ and energy $\tilde{E} = E/B$. (b) Differential rotational Lamb shift for the lowest nonzero-L states. (c) Zoom in illustrating the many-body-induced fine structure (MBIFS) of the first kind, $L_{L,0} \to \{L^-_{L,0}, L^+_{L,0}\}$, and of the second kind, $L^-_{L,0} \to L^-_{L-1,1}$. (d) Spectroscopic signatures of the MBIFS for the $L = 1$ state. The numbers indicate the corresponding values of $\ln(\tilde{n})$.

Additionally with increase of the interaction another feature of the angulon called many-body-induced fine structure (MBIFS) of the first and the second kind appears which are respectively related to the isotropic and the anisotropic part of the interaction. The angulon theory has already had many further application for example: study of the rotational spectrum of a cyanide molecular ion immersed into Bose-Einstein condensates of rubidium and strontium[57], understanding the behavior of molecules interacting with superfluid helium[58, 59], approach to the angulon based on the path-integral formalism, which sets the ground for a systematic, perturbative treatment of the angulon problem[60], diagrammatic Monte Carlo approach to angular momentum properties of quantum many-particle systems possessing a macroscopic number of degrees of freedom[61], approach to rotating impurities based on the notion of quantum groups[62] and recently quantum impurity possessing both translational and internal rotational degrees of freedom interacting with a bosonic bath[63]. All mentioned results are related to the interaction between the impurity and the bosonic bath.

### 1.6.2 *Ion immersed in the atomic bath*

There is a separate class of systems containing ionic impurity and usually immersed in a cloud of cold atoms forming the Bose-Einstein condensate[64–67]. It is worth emphasizing that for a long time such hybrid ion-atom systems were not possible in the experimental implementation in the quantum regime. Due to the difficulty of obtaining sufficiently low temperatures[68], the researchers searched for the best ion-atom mixture which, due to its physical and chemical properties, could be cooled down most easily. Schematically it is presented in Fig.8. We can see that one of the candidates was a mixture of ytterbium ion with lithium[69, 70], which was later used in the first experiment of ion-atom collisions in the quantum regime. Before this experiment, it was also considered to initiate ultracold ion-atom collisions through the use of Rydberg molecules[71]. In this case, the ion-atom collision was supposed to take place between the Rydberg ionic core and the ground-state atom. Meanwhile, other chemical processes such as ion-atom charge transfer [72] or the properties of the ionic polaron in the BEC[66] were also considered.

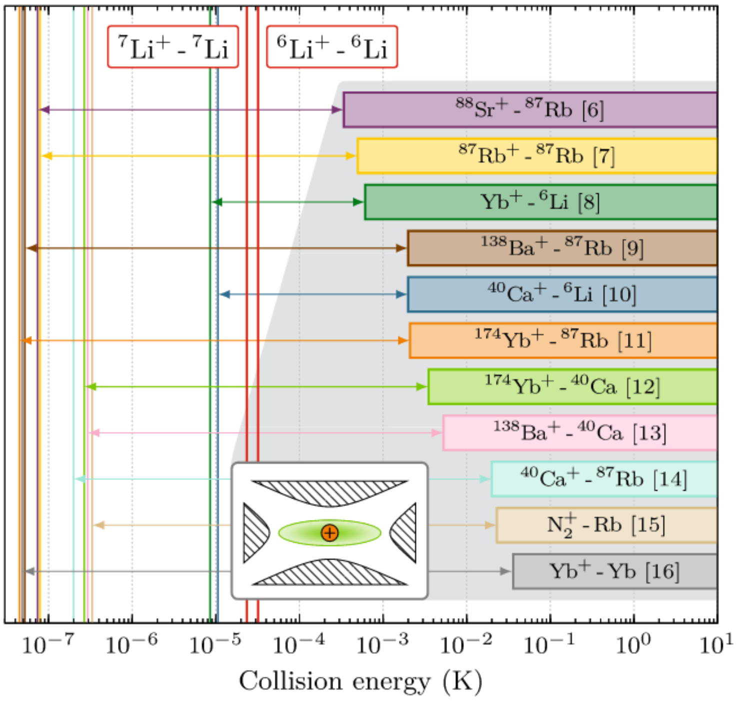

Figure 8: S-wave scattering limits for different ion-atom mixtures. From Ref.[71].

Ion-atom collision processes are currently considered as two-body processes. Three-body computations that could better explain the latest experiments are still underdeveloped. The Fig.9 below shows the results of the scattering calculations[73] performed 2 years before obtaining the quantum regime in the mixture of ytterbium ion with lithium atoms. The figure shows the spin exchange process for various channels depending on the collision energy, at that time still for arbitrarily selected scattering lengths. In later work, it was precisely the matching of the appropriate scattering lengths that turned out to be crucial for the explanation of the experimental results.

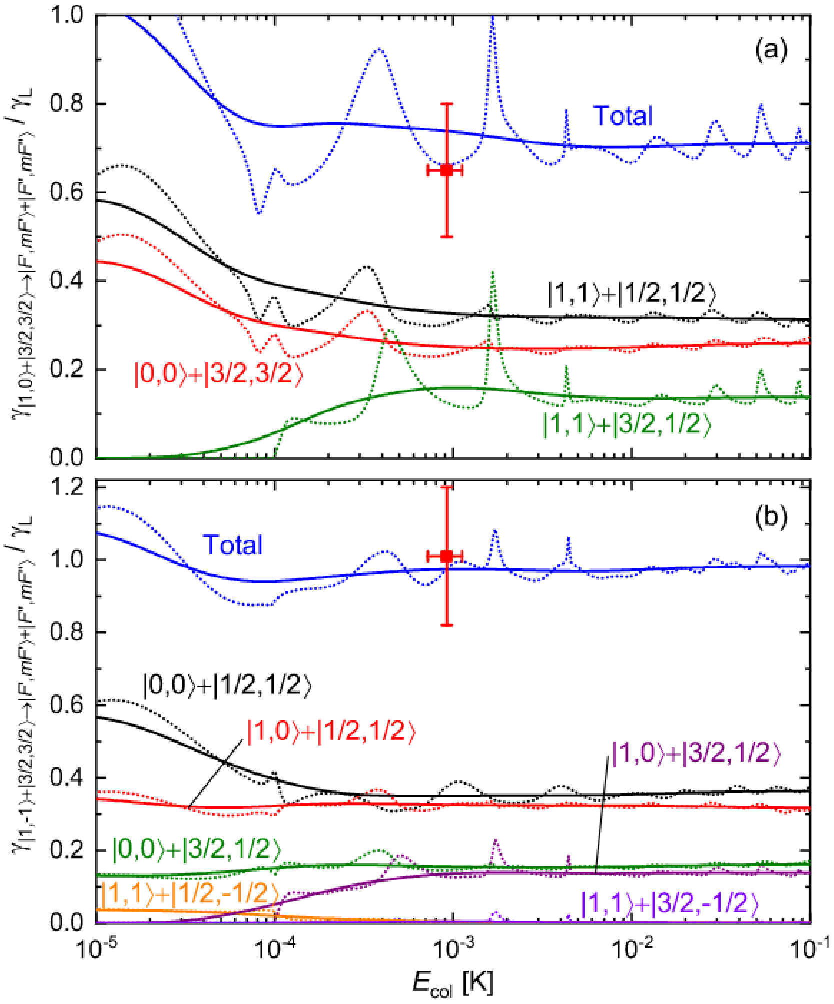

Figure 9: Spin-exchange rates: total and decomposed into different channels for Yb/Li mixture. Coupled-channel scattering calculations, from Ref.[73].

# Part II

# ION-ATOM INTERACTION AND SCATTERING THEORY

The ion-atom interaction is studied using interaction potentials calculated with the electronic structure theory. The interaction curves are calculated for singlet and triplet electronic states. Using multichannel quantum scattering and analysis of bound states, we calculate interesting properties of systems. This chapter describes the methods used.

# 2

# ION-ATOM INTERACTION

This chapter summarizes the basic theoretical methods used in the calculations and describes the phenomena studied.

## 2.1 INTRODUCTION

In nature, there are many types of atoms, molecules, and ions with complex interactions between them. Some of them are described by standard electromagnetism, others require quantum mechanics, quantum chemistry or quantum field theory. The methods discussed in this chapter are relatively standardized, but it is interesting to apply them to new ion-atomic mixtures in conjunction with the experiments performed. It is an effective tool in predicting new effects and explaining the observed phenomena. The following will be discussed: the calculation of potential energy curves, quantum scattering theory and its properties in ion-atom interactions, asymptotic bound state model and Feschbach resonances.

## 2.2 POTENTIAL ENERGY CURVES

Effective performance of scattering calculations requires prior knowledge of the interaction curves with the best possible precision. Obtaining curves for various types of mixtures, for example, atomic ion with an atom or molecular ion with an atom, requires the use of sophisticated quantum chemistry techniques such as calculations of the electronic structure, Hartree-Fock theory, multiconfigurational self-consistent field or coupled-cluster method[74]. These methods have been used many times[75–79] also in the context of ion-atom systems[69, 80]. The ion-atom interaction potential within the Born-Oppenheimer approximation can be calculated as the difference between the energies of the complex and the separated components[1]

$$V_{A^{+}+B} = E_{A^{+}+B} - E_{A^{+}} - E_{B}. \tag{19}$$

This section will characterize the ion-atom interactions and discuss the main assumptions of the coupled-cluster method.

### 2.2.1 *Long-range part of the interaction*

Ion-atom interactions due to the presence of an electric charge are dominated by the induction term. This type of interactions is characterized by the dependence $1/R^4$, which is much stronger than typical van der Waals interactions $1/R^6$. In the simplest situation, i.e. the interaction of an ion in the S-state and an atom in the electronic ground state, the potential can be approximated by the following expression[1]:

$$V(R) \approx -\frac{C_4^{ind}}{R^4} - \frac{C_6^{ind}}{R^6} - \frac{C_6^{disp}}{R^6}, \tag{20}$$

where the leading coefficient has a value related to the static electric dipole polarizability of the atom, $\alpha^{atom}$ and the charge of the ion q:

$$C_4^{ind} = \frac{1}{2} q^2 \alpha^{atom}. \tag{21}$$

It is responsible for the interaction of the ion's charge with the induced dipole moment of the atom. The next term which is related to the quadrupole polarizability of the atom is understood as the interaction of the charge with the induced quadrupole moment,

$$C_6^{ind} = \frac{1}{2} q^2 \beta^{atom}. \tag{22}$$

And the last term describing dispersions, which is the interaction between instantaneous dipole-induced dipole moments of the ion and atom:

$$C_6^{disp} = \frac{3}{\pi} \int_0^\infty \alpha^{ion}(i\omega) \alpha^{atom}(i\omega) d\omega. \tag{23}$$

### 2.2.2 *Molecular electronic structure theory*

Large-scale electronic structure calculations are performed using the coupled-cluster method or multireference methods. The coupled-cluster method and its various variants are a key tool in calculating the interaction potentials in many very complex atomic, ionic and molecular systems[74]. The starting point of the method is the wave function written in the form:

$$|CC\rangle = \exp(T)\,|HF\rangle \tag{24}$$

with $|HF\rangle$ the Hartree-Fock reference state. The cluster operator takes the following form:

$$T = \sum_{\mu} t_\mu \tau_\mu, \tag{25}$$

where operators:

$$[\tau_\mu, \tau_\nu] = 0 \tag{26}$$

These operators, acting on the $|HF\rangle$ state, generate an excited electronic state:

$$\tau_\mu |HF\rangle = |\mu\rangle \,. \tag{27}$$

The cluster operator is divided into:

$$T = T_1 + T_2 + T_3 + ..., \tag{28}$$

where single excitations:

$$T_1 = \sum_{A,I} t_I^A a_A^\dagger a_I, \tag{29}$$

double excitations:

$$T_2 = \sum_{A>B} \sum_{I>J} t_{IJ}^{AB} a_A^\dagger a_I a_B^\dagger a_J, \tag{30}$$

and so on, finally the coupled-cluster energy is given by:

$$E_{CC} = \langle HF| \exp(-T) H_0 \exp(T) |HF\rangle \tag{31}$$

The calculations of the electronic structure of the considered $Ba^+/Li$ and $Yb^+/Li$ mixtures were not the subject of a doctoral dissertation. The data comes from previous publications by Michał Tomza.

## 2.3 QUANTUM SCATTERING THEORY

The theory of scattering in both the classical[81] and quantum world[1, 82–84] plays an important role in the description of phenomena and interactions between bodies. Many physical quantities, such as cross sections or scattering lengths, have their classical and quantum counterparts, but the quantum description of collisions contains much more information, such as the wave function, phase shift, and partial wave expansion. In particular, the presence of higher partial waves in collisions, understood as a non-zero cross section in a given wave, defines the nature of the collision on the energy scale. In collisions that are really low energy in the so-called ultracold regime we deal with collisions in the lowest s-wave, i.e. with zero angular momentum in relative rotational motion.

We start our discussion of collisions between a pair of particles with the general Hamiltonian[82], which can later be specified for the case under study

$$H = -\frac{\hbar^2}{2\mu}\nabla^2 + \hat{H}_{int}(\tau) + V(r, \tau). \tag{32}$$

In the equation above, $\tau$ relates to internal degrees of freedom other than the distance between the particles. Meanwhile, the first term is kinetic energy the next terms in the equation correspond to the internal Hamiltonian of the particles and the interaction potential. The interaction potential between particles in specific spin states is independently calculated using the quantum chemical methods mentioned in the previous section. In general, to perform the scattering calculations and the analysis of the experimental results, we first need to calculate the interaction potential for each considered mixture. At the same time, there is still the freedom to multiply the potential by the constant, which translates into the possibility of setting the desired scattering length, which is essentially unknown. We use this feature to explain the experimental results by treating the scattering lengths as parameters.

In general, the wave function of colliding particles has the following form:

$$\Psi(r,\tau) = r^{-1}\sum_i \phi_i(\tau)\psi_i(r). \tag{33}$$

$\{\phi_i(\tau)\}$ are the base functions in the $\tau$ coordinates. Total wave function has components in each channel i. Since the wavefunction must be regular at the origin, short range boundary conditions are superimposed

$$\psi_i(r) \to 0 \quad \text{as} \quad r \to 0. \tag{34}$$

Using expansion from Eq.(33) in the Schrodinger equation and projecting onto a single channel functions, we obtain a set of coupled scattering equations[82]

$$\left[-\frac{\hbar^2}{2\mu}\frac{d^2}{dr^2} - E\right]\psi_j(r) = -\sum_i W_{ji}\psi_i(r). \tag{35}$$

The i, j indices contain all quantum numbers describing a given channel. Based on the above procedure, we can define the coupling matrix W

$$W_{ji}(r) = \int \phi_j^*(\tau)\left[H_{int}(\tau) + V(r,\tau) + \frac{\hat{L}^2}{2\mu r^2}\right]\phi_i(\tau)d\tau. \tag{36}$$

Additionally, long-range boundary conditions are imposed in the form of:

$$\Psi(r) \underset{r\to\infty}{=} \mathbf{J}(r) + \mathbf{N}(r)\mathbf{K}, \tag{37}$$

where J(r) and N(r) are diagonal matrices which are defined by spherical Bessel functions and K is symmetric matrix which is related do the S-matrix

$$S = (1 + i\mathbf{K})^{-1}(1 - i\mathbf{K}). \tag{38}$$

If the S-matrix has been computed, we can obtain energy-dependent quantities such as:

- scattering length:

$$a_n(E) = \frac{1}{ik_n}\frac{1 - S_{nn}}{1 + S_{nn}}, \tag{39}$$

- partial elastic cross section:

$$\sigma^n_{el}(E) = \frac{\pi}{k_n^2}|1 - S_{nn}|^2, \tag{40}$$

- partial inelastic cross section:

$$\sigma^n_{el}(E) = \frac{\pi}{k_n^2}(1 - |S_{nn}|)^2, \tag{41}$$

where the channel wave vector is defined: $k_n = \sqrt{2\mu(E - E^{\infty}_n/\hbar^2)}$. The calculations made for the experiment actually correspond to the thermally averaged collision rate coefficients defined as: $K = \langle \frac{\hbar k}{\mu}\sigma \rangle_T$. The Hamiltonian describing the collisions of an atomic ion with an atom is commonly used in the literature[1, 69, 85–87] as follows:

$$\hat{H} = -\frac{\hbar^2}{2\mu}\frac{1}{R}\frac{d^2}{dR^2}R + \frac{l^2}{2\mu R^2} + \hat{V}(R) + \hat{V}^{ss}(R) + \hat{V}^{so}(R) + \hat{H}_A + \hat{H}_B \tag{42}$$

The Hamiltonian includes the following terms:

- the interaction potential with dependence on spin $S$ and $M_S$:

$$\hat{V}(R) \sum_{S,M_S} V_S(R)\,|S, M_S\rangle\,\langle S, M_S|, \tag{43}$$

- the spin dipole-dipole interaction:

$$V^{ss}(R) = -\sqrt{\frac{44\pi}{5}\frac{\alpha^2}{R^3}}\sum_q Y^q_2(\hat{R})[\hat{s}_a \otimes \hat{s}_b]^{(2)}_q, \tag{44}$$

- the second-order spin-orbit term:

$$V^{so}(R) = \sqrt{\frac{44\pi}{5}}\lambda_{SO}(R)\sum_q Y^q_2(\hat{R})[\hat{s}_a \otimes \hat{s}_b]^{(2)}_q, \tag{45}$$

- the atomic Hamiltonian with hyperfine and Zeeman terms:

$$\hat{H}_j = \zeta_j \hat{\imath} \cdot \hat{s}_j + g_e \mu_B \hat{s}_j \cdot B + g_j \mu_N \hat{\imath}_j \cdot B. \tag{46}$$

Moreover, in ion-atom interactions we can introduce the interaction lenght scale $R^*_4$ related to the $C_4$ coefficient responsible for the leading contribution to the ion-atom interaction ($V(R) \approx -\frac{C_4}{R^4}$). The coefficient R4 will be useful as a size scale in determining, for example, the ion-atom scattering length. Similarly, we can define the energy scale $E^*$ in the system. In the following equations, $\mu$ is the reduced mass.

$$R^*_4 = \sqrt{\frac{2\mu C_4}{\hbar^2}} \quad \text{and} \quad E^* = \frac{\hbar^2}{2\mu(R^*_4)^2} \tag{47}$$

## 2.4 FESCHBACH RESONACES

Controlling the scattering length using a magnetic field is a technique called Feshbach resonance[88–90] and has been used many times in experiments with cold atoms[91], molecules[92] and more recently ion-atom systems[93]. This is a very important technique that underpins most research in modern ultracold physics. In this section, we will provide a general idea of the formation of Feschbach resonances and how to identify them.

We consider a simple model as shown in the Fig.10 which includes two molecular potentials: $V_{bg}(R)$ - open channel for collisions with small energy E, asymptotically represents two free atoms and $V_c(R)$ - relates to the closed channel.

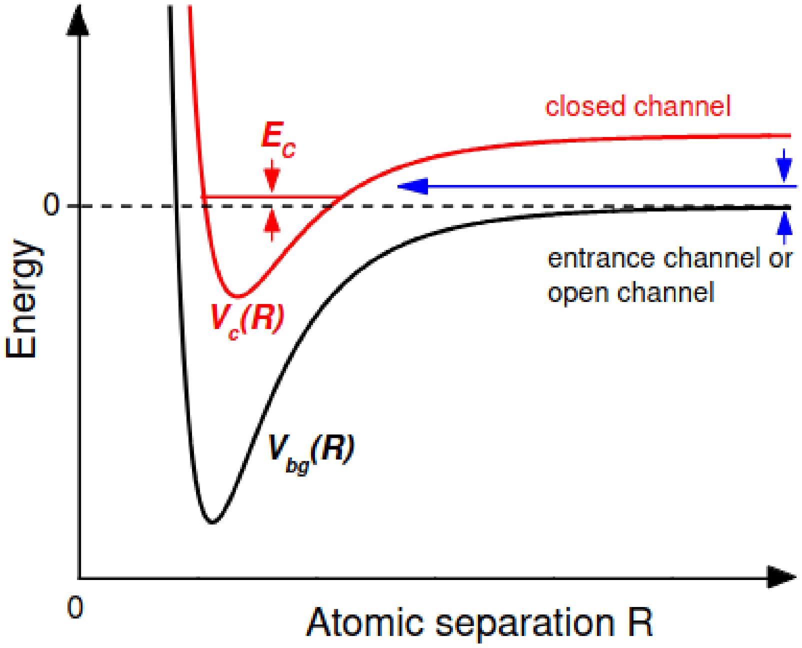

Figure 10: Two-channel Feshbach resonance model. In the figure, the open and closed channels and the coupling between them are marked. From Ref.[4].

The essence of the Feshbach resonance is the ability to control the energy difference if the respective magnetic moments in the channels are different. In such a situation, even a small coupling can lead to resonance and mixing between the channels, this is when the bound molecular state in the closed channel begins to approach the scattering state in the open channel. The Feshbach resonance as a function of the magnetic field is often described by a simple model[4] that expresses the value of the scattering length

$$a(B) = a_{bg}\left(1 - \frac{\Delta}{B - B_0}\right). \tag{48}$$

In the above equation, the parameters mean: $a_{bg}$ - background scattering length, $\Delta$ - resonance width and $B_0$ - position of the resonance. The resonance parameters are visualized on the Fig.11.

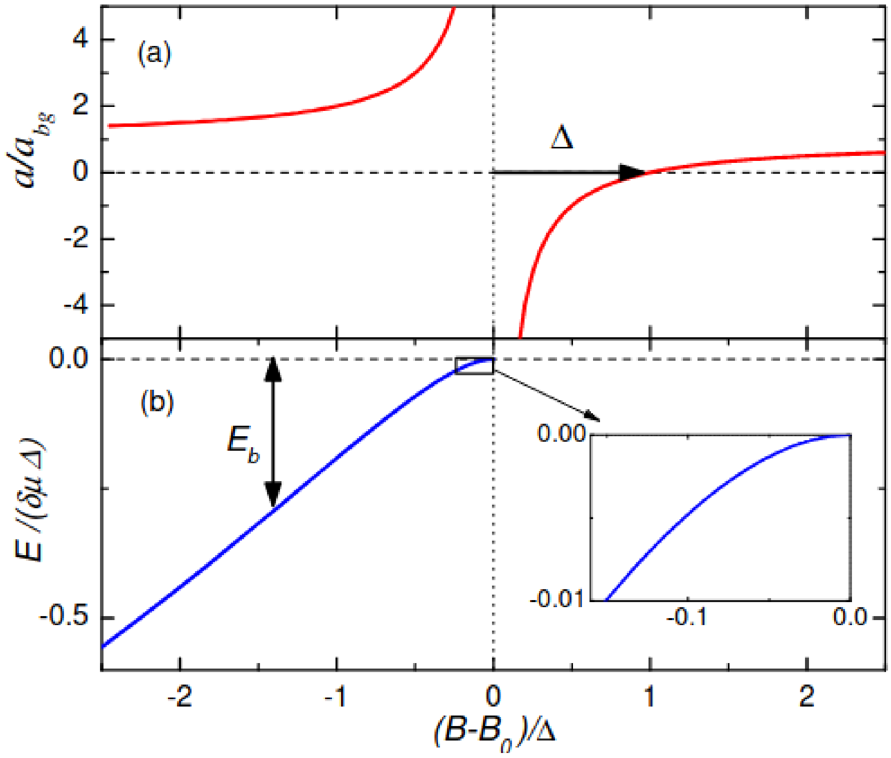

Figure 11: (a) Scattering length as a function of the magnetic field. (b) The binding energy in the molecular state with energy E close to the Feshbach resonance. From Ref.[4]

Moreover, the fact that we can influence the value of the scattering length by means of the magnetic field results in the possibility of controlling and changing the interactions between atoms. This situation also allows for the emergence of molecular bound states and the formation of so-called Feshbach molecules[94–98] both fermionic and bosonic, which have been successfully implemented in experiments with cold atoms and Bose-Einstein condensate. Fig.11b shows the energy of a weakly bound molecular state. Such a state exists in the region of strong coupling on the resonance side, where the scattering length is positive. Binding energy close to the resonance is stated as follows (defined to be positive $E_b = -E$):

$$E_b = \frac{\hbar^2}{2\mu a^2}, \tag{49}$$

where: $\mu$ - the reduced mass and $a$ - the scattering lenght.

The observation of Feshbach resonances in an experiment is often associated with a sharp decrease in the number of atoms at the position of the resonance, which is explained as three-body losses. It is this scenario that was presented in the famous work, where Feshbach resonances were observed in the Bose-Einstein condensate of sodium atoms[89]. The Fig.12 shows that the losses occur exactly at the Feshbach resonance.

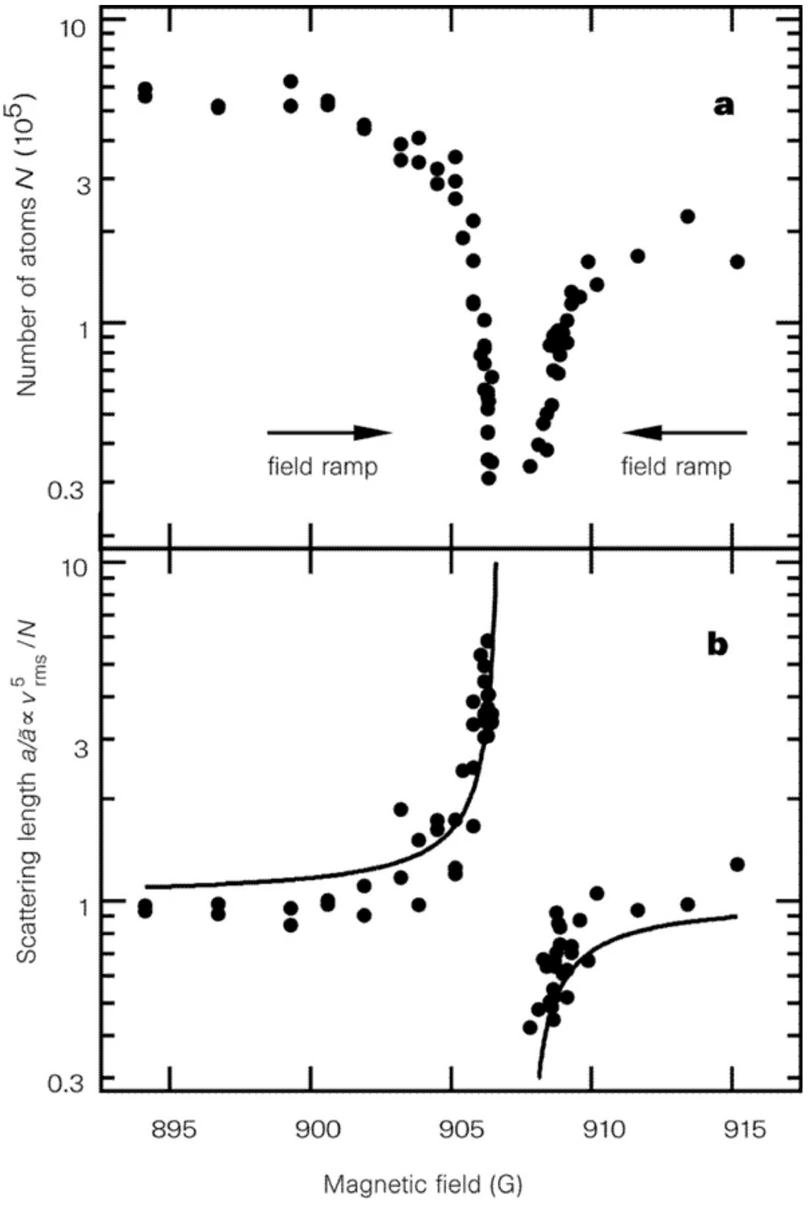

Figure 12: Observation of the Feshbach resonance in BEC, from Ref.[89]. The number of atoms clearly decreases at the resonance point, where the scattering length tends to infinity.

Another particular consequence of the control with Feshbach resonances was the measurement of Efimov states that are associated with the three-body attraction through short-range resonant interactions[99–102]. In order to better understand the importance of Feshbach resonances, it is worth recalling the example of the realization of the

Bose-Einstein condensate of cesium atoms. Due to the very fast two-body inelastic losses, it was impossible to efficiently cool the atoms and, consequently, to obtain condensate, despite having previously received other condensates: rubidium-87[103], lithium-7[104], potassium-41[105], rubidium-85[106], sodium-23[107], hydrogen[108] and metastable helium-4[109]. The condensate of cesium atoms was obtained only by applying the Feshbach resonance technique that allows for re-tuning the scattering length using a magnetic field[110]. Our research, in which we obtained Feshbach resonances for the ion-atom system for the first time, is also motivated by a complementary picture of quantum tools and systems in which such phenomena can be measured. Especially when the resonances in the ion-molecule system[92] and between alkali and closed-shell atoms[111] were measured.

### 2.4.1 *Asymptotic bound state model*

Estimating the position of the Feshbach resonances can be very computationally complex if we do not know parameters such as the scattering lengths, the collision energy or the expected resonance structure. In particular, the appearance of resonances in higher partial waves or the displacement or splitting of resonances related to the spin-orbit coupling. Scattering calculations can answer this problem, however, it requires a lot of computer resources and time. For this reason, the asymptotic bound state model will first be presented that provides an estimate of the resonance positions using less computer resources. This model[112] allows for the calculation of coupled bound states in a two-body system. By analyzing the intersections of the bound states, it is possible to estimate the position of the resonances. In ABM model we devide hamiltonian into relative and internal parts:

$$H = H^{rel} + H^{int}. \tag{50}$$

Relative Hamiltonian describes relative motion in the center of mass system: kinetic energy, effective interaction and internal Hamiltonian: internal energies of colliding atoms. The atomic Hamiltonian consists of hyperfine and Zeeman terms:

$$H^{A} = H^{hf} + H^{Z} = \frac{a_h f}{\hbar^2} i \cdot s + (\gamma_e s - \gamma_i i) \cdot B, \tag{51}$$

where: s,i - electron and nuclear spins, $\gamma_e$, $\gamma_i$ - corresponding gyromagnetic ratios and $H^{int} = H^{A}_{\alpha} + H^{A}_{\beta}$. The colliding atoms are labeled with $\alpha$ and $\beta$ and spin states of the colliding pair are described: $|\alpha\beta\rangle = |f_\alpha m_{f_\alpha} f_\beta m_{f_\beta}\rangle$ Ultimately, the relative Hamiltonian for the singlet or triplet interaction S, the vibrational state $\nu$, and the rotational state $l$, can be written:

$$\left(-\frac{\hbar^2}{2\mu}\frac{d^2}{dr^2} + V^{l}_{S}(r)\right)\psi^{Sl}_{\nu}(r) = \epsilon^{Sl}_{\nu}\psi^{Sl}_{\nu}(r), \tag{52}$$

where $V_S^l(r) = V_S(r) + \frac{l(l+1)\hbar^2}{2\mu r^2}$. In the ABM model, we solve the Schrodinger equation using a limited set of eigenstates: $|\psi_\nu^{Sl}\rangle\,|Y_{m_l}^l\rangle$ of $H^{rel}$ and binding energies $\epsilon_\nu^{Sl}$. Diagonalization of the full Hamiltonian is equivalent to solving following equation with restricted set of bound states $\{|\psi_\nu^{Sl}\rangle\,|\sigma\rangle\}$, where $|\sigma\rangle = |SM_S IM_I\rangle$ with I - the total nuclear spin and $M_I$ - the corresponding magnetic quantum number.

$$\det|(\epsilon_\nu^{Sl} - E_b)\delta_{\nu l\sigma,\nu' l'\sigma'} + \langle\psi_\nu^{Sl}|\psi_{\nu'}^{S'l}\rangle\,\langle\sigma|H^{int}|\sigma'\rangle\,| = 0, \tag{53}$$

where $E_b$ are eigenvalues of the full Hamiltonian. These eigenstates define bound states in the system of coupled channels.

### 2.4.2 *Scattering calculations*

The scattering calculation is a computer demanding task and very often requires the use of large computing clusters. In such calculations, we are interested in obtaining the quantities defined in the subsection 2.3, such as scattering lengths, elastic and inelastic cross sections. They can be interpreted physically as spin-exchange processes or Feshbach resonances. We use the Numerov method[113] to propagate the Schrodinger equation, implemented in our own Python code and in the form of QDYN and Molscat software. We solve a numerical problem in the form:

$$\frac{d^2\Phi(R)}{dR^2} + k^2(R)\Phi(R) = 0, \tag{54}$$

where:

$$k^2(R) = \frac{2\mu}{\hbar}(E - W(R)), \tag{55}$$

and the matrix W contains all the couplings present in the Hamiltonian. The scattering wavefunction is constructed in a fully uncoupled basis set:

$$|i_{ion}, m_{i,ion}\rangle\,|s_{ion}, m_{s,ion}\rangle\,|i_{atom}, m_{i,atom}\rangle\,|s_{atom}, m_{s,atom}\rangle\,|l, m_l\rangle\,, \tag{56}$$

where: s,i refers to spin and nuclear spin for an atom and an ion. Whereas l refers to the relative rotation. Propagating the $F_n = \Phi_{n+1}\Phi_n^{-1}$ ratio provides better numerical stability, so we use it instead of $\Phi$:

$$F_n = \left(1 + \frac{h^2}{12}k_{n+1}^2\right)^{-1}\left(2(1 - \frac{5h^2}{12}k_n^2) - (1 + \frac{h^2}{12}k_{n-1}^2)F_{n-1}^{-1}\right) \tag{57}$$

Propagation starts from the classically forbidden area $R_0$ and ends at a sufficiently long distance $R_{max}$ with variable step h, where $R_n = R_0 + nh$. Knowing the long-range boundary conditions for $\Phi$:

$$\Phi(R) \underset{r\to\infty}{=} \mathbf{J}(r) + \mathbf{N}(r)\mathbf{K}, \tag{58}$$

we can calculate the matrices K and S from $F_n$ propagation. Hence the appropriate cross-sections and scattering lengths in selected channels. In multi-channel quantum scattering calculations, we include all available channels and spin states in which collisions and other processes may occur.

### 2.4.3 *Influence of the spin-orbit coupling*

In calculations for certain systems with a significant spin-orbit coupling, we observe additional effects such as shifting or splitting Feshbach resonances in higher partial waves[114, 115]. We identified a very large spin-orbit coupling in the studied system: $Ba^+/Li$, which will be described in more detail in the following paragraphs. It was typical that despite observing Fesbhach resonances dozens of times in various atomic configurations and arrangements, in most cases the resonances were measured in the s-wave, with some exceptions where the coupling of the s-wave with higher waves was measured. In the article [115] they measured for the first time direct coupling between an open channel d-wave and a closed channel d-wave. The measurement performed on the ultracold mixture of $^{85}Rb$-$^{87}Rb$ atoms showed clearly the splitting of the d-wave resonances, closely related to the spin-orbit coupling. This example served us as an important premise for the correct explanation of the nature of the resonances in the barium ion with lithium atoms system. It can be seen that despite the widespread use of the Feshbach resonance technique, the coupling in higher partial waves, in particular for large spin-orbit couplings, still remains a fresh research topic.

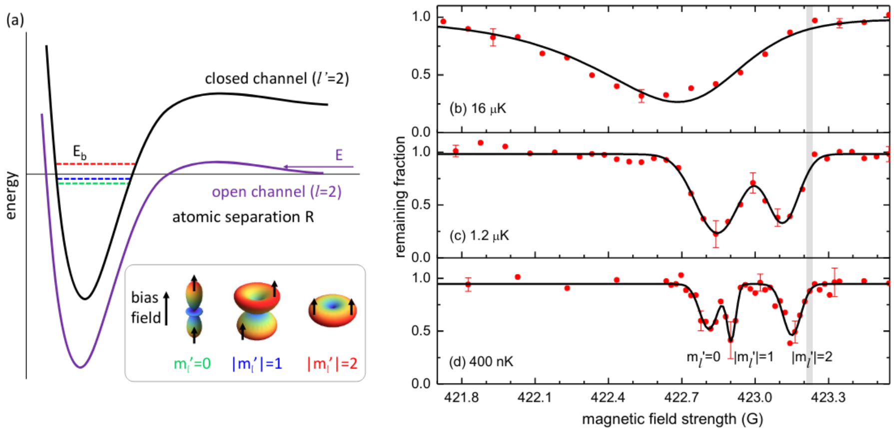

Figure 13: The d-wave Feshbach resonance. The splitting of the bound states causes the splitting of the observed d-wave resonances corresponding to the absolute value of the magnetic number. From Ref.[115].

# Part III

# EXPERIMENTS WITH ION-ATOM SYSTEMS

No theoretical effort is possible without the development of experiments and vice versa. This chapter details the great experiments carried out in Amsterdam and Freiburg. The systems built there allowed to observe, measure and later confirm theoretically the first ever ion-atom collisions in the quantum regime and Feschbach resonances in the ion-atom system.

# 3

# EXPERIMENTAL TECHNIQUES FOR ION-ATOM SYSTEMS

The cooling techniques used in the field of cold atoms have a long tradition[116–120] and their culmination was the first observation of a Bose-Einstein condensate in 1995[103]. Later, various techniques for cooling atoms[121–123] were refined and successively applied in other experiments[124]. The basic methods of achieving the quantum regime in the effective interactions of atoms include: the use of Zeeman slower, Dopler cooling, laser cooling and evaporating cooling. Typically, the atoms are placed in a magneto-optical trap (MOT). These cooling methods will be briefly discussed in this chapter. For ions, Paul or Penning traps are used[125, 126] , and for ion-atom systems, hybrid traps consisting of an ion trap and an atomic trap[1]. However, for ion-atom systems, cooling to temperatures low enough to be considered a quantum regime requires much more effort. It is related to the specificity of an electrically charged ion placed in a trap with an alternating electric field, it causes additional effects that hinder cooling, such as the so-called micromotion. This will also be discussed in this chapter.

## 3.1 COOLING TECHNIQUES

### 3.1.1 *Zeeman slower*

The standard first stage of cooling the atoms is to use the Zeeman slower[116]. This method of cooling makes it possible to cope with the atoms that leave the oven at a temperature of several hundred Kelvin, so even greater than room temperature. Finally, it is possible to reach temperatures even close to 1 K and trap atoms in the magneto-optical trap. By using a laser beam that is opposite to the direction of the atoms’ movement, we can cause the absorption of photons in a selected atomic transition and then spontaneous emission without a specific direction, which will effectively slow down the movement of atoms. The situation is unfortunately more complicated due to the Doppler effect. Therefore, when the atoms decrease their velocity, the frequency of the laser beam is seen differently, which causes the laser beam to no longer match the atomic transition in which we were absorbing the photons. The solution to this problem is the use of spatially inhomogeneous magnetic field that changes along the axis of the cylinder formed by the solenoids. By appropriately adjusting the magnetic field, we can use the Zeeman effect to shift the atomic levels, in this way we obtain the matching of atomic transitions to the laser frequency, eliminating the difficulties caused by the Doppler effect. This is why the technique is called Zeeman slower.

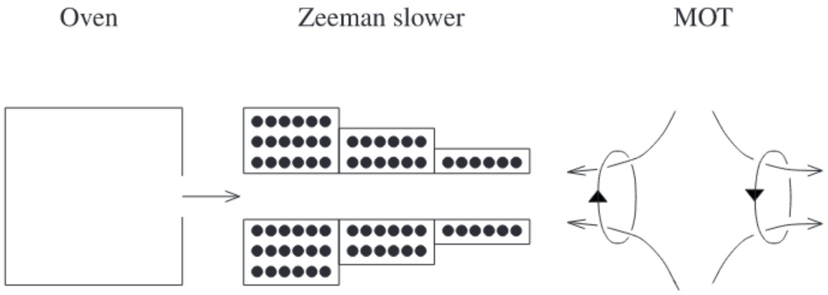

Figure 14: Typical protocol for pre-cooling atoms with Zeeman slower and placing them in a magneto-optical trap. Figure from Ref.[6].

### 3.1.2 *Doppler laser cooling*

The basic idea behind Doppler cooling[119, 120] is the use of counter-propagating laser beams of the same frequency $\omega$. The laser frequency is chosen slightly below the atomic transition frequency that we use in the cooling process, sometimes in such a situation it is said that the laser is red-detuned. This configuration causes atoms to "more readily" absorb photons from beams that are directed opposite to their motion. The effect is related to the shift of the frequency seen by the atoms in the direction appropriate to the occurrence of the atomic transition. The Doppler effect is responsible for this, hence it is often referred to as Doppler cooling. Schematically it is shown in the Fig.15, where we can see the rate of absorption depending on the direction

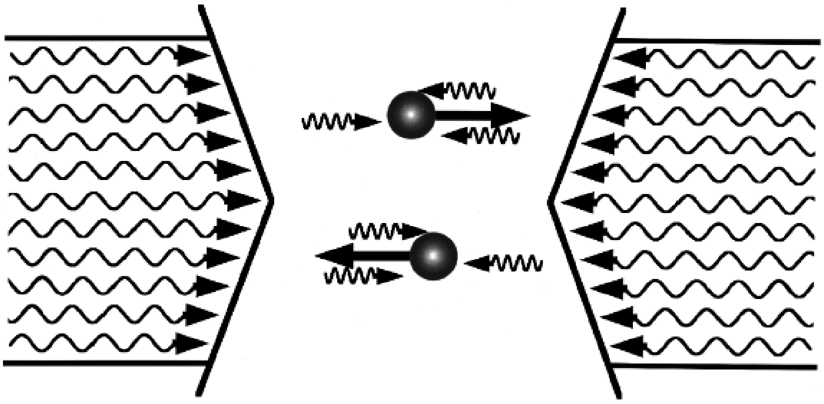

Figure 15: Ilustration of the Doppler cooling. Figure from Ref.[118].

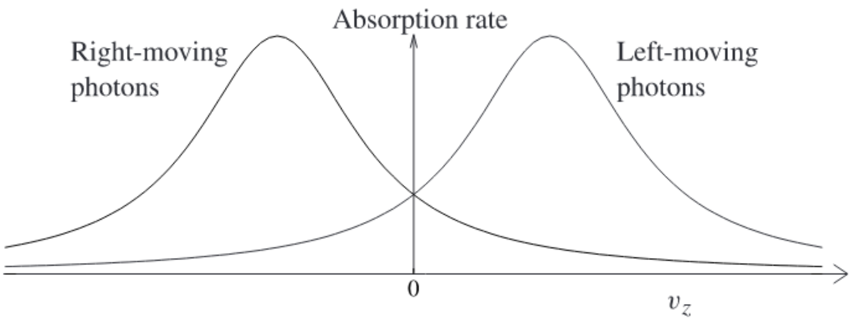

Figure 16: Ilustration of the Doppler cooling. Figure from Ref.[6]

of the velocity of the atom. Since photon absorption is related to the momentum transfer to the atom in the direction of beam propagation, the absorption process from two laser beams can be equated with the frictional force slowing down the movement of atoms.

The final temperature is a product of the equilibrium that forms between the cooling process and the randomness of heating atoms related to the absorption and emission processes. It has been shown that the minimum temperature that we are able to achieve in Doppler cooling is limited by[118, 127]:

$$T_D = \hbar\Gamma/2k_B, \tag{59}$$

where $\hbar$ is the reduced Planck constant and $k_B$ the Boltzmann constant. The parameter $\Gamma$ is the rate of spontaneous emission of the excited state (and $\Gamma^{-1}$ is the excited state lifetime). As can be seen from the above equation, the minimum temperature that can be achieved depends on the choice of the atomic transition, usually around tens to a few hundred microkelvins depending on the atom and transition selected.

### 3.1.3 *Evaporating cooling*

Evaporative cooling[128, 129] is used to achieve even lower temperatures than laser cooling allows. Historically, this has been an important contribution to the Bose-Einstein Condensate experiments. Evaporative cooling is based on the fact that if the particles leaving the system have an energy greater than the average energy in the system, the remaining particles in the trap are cooled down. The reason why such a technique is effective lies in the fact that there are always high-energy particles in the tail of the Maxwell-Boltzman distribution that may exit the trap and allow the system to cool down. Energetic atoms with energy above the threshold can evaporate from the trap, lowering the temperature of the remaining atoms. It can be shown very easily that the evaporation of the most energetic atoms leads to the cooling of the remaining atoms. Assuming that the energy of the particle leaving the trap is:$(1+\beta)\bar{\epsilon}$ [6], we can use the fact that the total energy of all particles should be conserved. We denote the change in the number of particles as dN (negative). The total energy of the particles remaining in the trap is: $E+(1+\beta)\bar{\epsilon}dN$ with number of particles: $N+dN$. Hence the average energy per atom:

$$\bar{\epsilon}+d\bar{\epsilon}=\frac{E+(1+\beta)\bar{\epsilon}dN}{N+dN}, \tag{60}$$

what can be transformed into:

$$\frac{\bar{\epsilon}}{\bar{\epsilon}(0)}=\left(\frac{N}{N(0)}\right)^{\beta}. \tag{61}$$

Now we can see directly that the energy of the particles in the trap decreases as the number of particles decreases, taking into account the $\beta$ exponent.

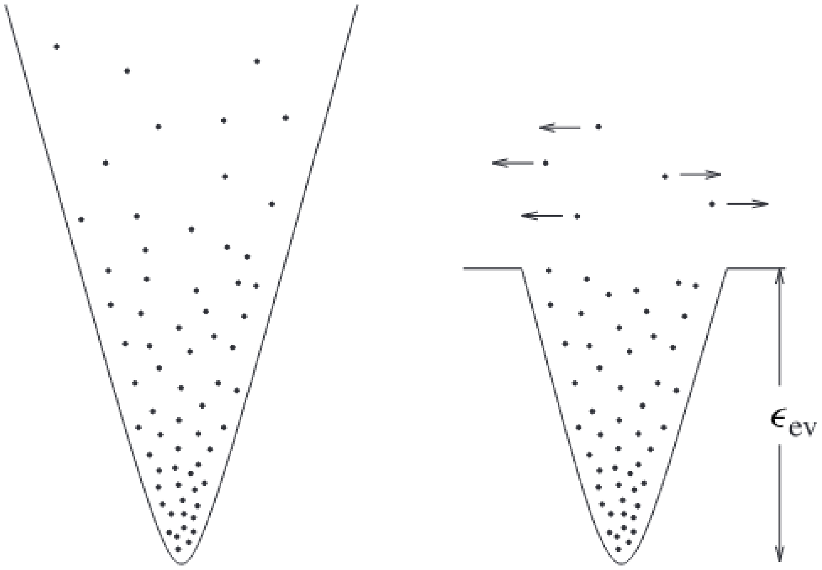

Figure 17: Evaporative cooling scheme, $\epsilon_{ev}$ is the evaporation threshold. Figure from Ref.[6]

### 3.2 HYBRID ION-ATOM TRAPS

In this section ion-atom traps will be announced, without going into technical details, the principles of operation of the basic traps for atoms and ions, and then the hybrid trap. The basic tool used in the physics of cold atoms in almost every experiment at some stage in the preparation of the system for measurements is a magneto-optical trap (schematically presented on Fig.18). The magneto-optical trap

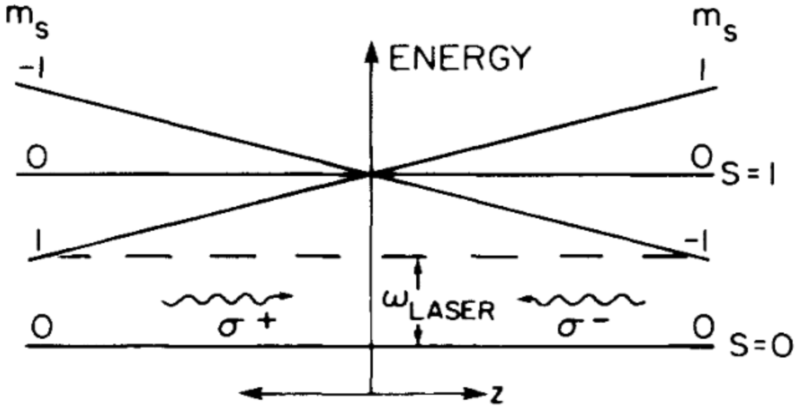

Figure 18: Schematic energy diagram of an atom in a magnetic field affected by counter-rotating laser beams. Illustration of the operation of the magneto-optical trap. Figure from Ref.[130]

uses laser cooling and a spatially-varying magnetic field to keep the neutral atoms inside. The trap is formed by 6 circularly polarized laser beams crossing a quadrupole magnetic field. The principle of operation of the trap is based on the use of the Zeeman effect, non-homogeneous in space, which causes energy levels in atoms to shift. Laser beams moving from opposite sides tuned below the resonance frequency cause the atoms to absorb more photons from the beam $\sigma^-$ on the $z > 0$ side and more photons from the beam $\sigma^+$ on the $z < 0$ side (Fig.18). This creates an effective force in the z = 0 direction that keeps the atoms at the center of the trap.

### 3.2.1 *Optical dipole trap*

Another important element of the systems used to study cold atoms are optical dipole traps[131]. This type of trap, used e.g. in the Freiburg experiment as an alternative to the radio frequency trap for ions, is based on the interaction of laser light with an induced dipole moment. Without going into technical details, we will only show the main feature of this trap. The induced dipole moment of atoms is related to the amplitude of the electric field by the factor $\alpha$, i.e. complex polarizability, dependent on the driving frequency

$$p = \alpha E. \tag{62}$$

The potential of the induced dipole moment in the driving field is as follows[131]:

$$U_{dip} = -\frac{1}{2}\langle pE\rangle = -\frac{1}{2\varepsilon_0 c}\mathrm{Re}(\alpha)I, \tag{63}$$

where the field intensity: $I = 2\varepsilon_0 c|E|^2$. Hence, we obtain a dipole force that is proportional to the field intensity gradient:

$$F_{dip}(r) = -\nabla U_{dip}(r) = \frac{1}{2\varepsilon_0 c}\mathrm{Re}(\alpha)\nabla I(r), \tag{64}$$

which explains in a very simple picture the essence of the operation of the ODT.

### 3.2.2 *Paul trap*

In experiments with hybrid ion-atom systems, the trap that was used as a component to trap the ions was a quadrupole ion trap called the Paul trap. It is well known that it is not possible to trap charged ions in a static electric potential, and the use of optical traps also presents some difficulties. This is the reason why time-varying potentials are used. A typical configuration of a Paul linear trap (also known as a radio-frequency trap) is shown in Fig.19. Schematically in Fig.19: common rf potential $U = U_0 \cos(\omega_{rf} t)$ is connected to the dark electrodes. Lower part of the figure shows x-y electric fields from the applied rf potential when the rf potential is positive relative to the ground. Additionally, a static electric potential is created in the z direction.

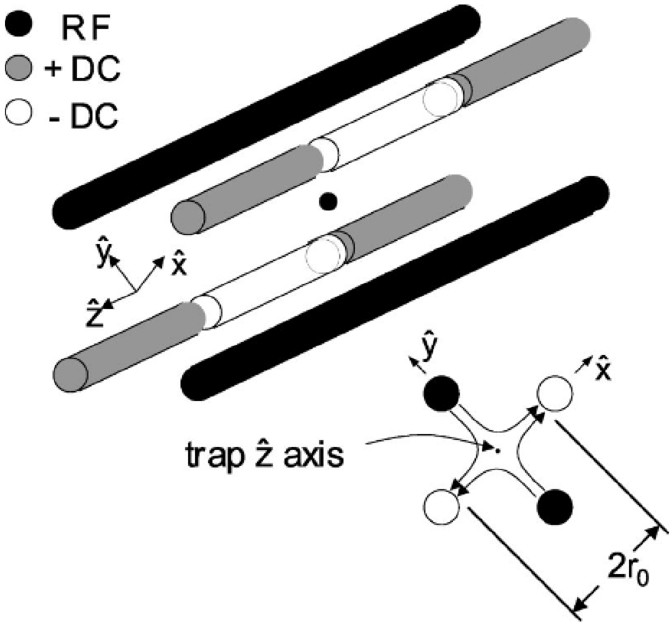

Figure 19: The linear Paul trap for charged ions. Figure from Ref.[32]

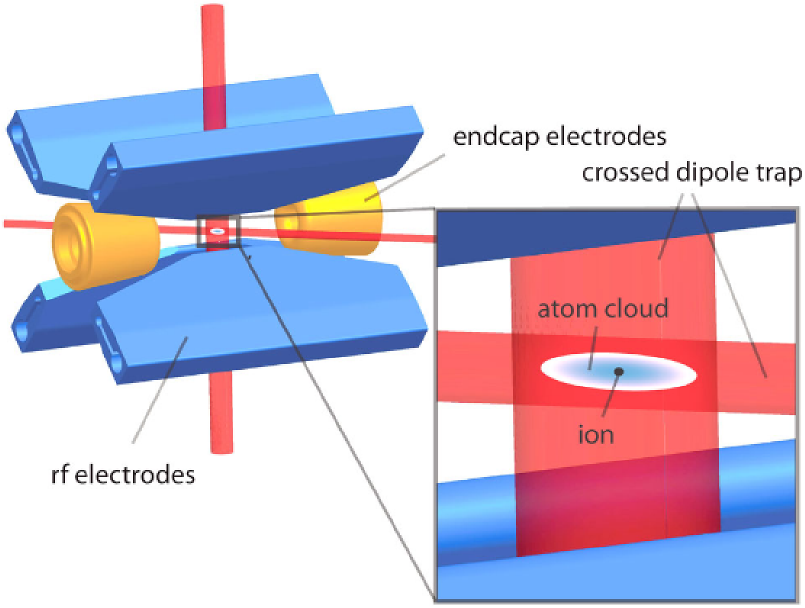

Figure 20: The hybrid ion-atom trap consists of an overlapping Paul ion trap and an optical dipole trap. Figure from Ref.[132]

### 3.2.3 *Hybrid trap*

Finally, we come to the scheme of the hybrid ion-atomic trap. This type of trap is a skilful combination of an optical dipole trap for atoms and a radio-frequeancy trap for ions. Atoms are prepared independently: cooled to ultra-cold temperatures and trapped. The same thing happens with ions, they are prepared in the Paul trap. Only later are two traps experimentally superimposed. The collision process when the traps are crossed is the target of measurement.

## 3.3 MICROMOTION IN ION-ATOM SYSTEMS

One of the side effects of holding an ion in a radio-frequency trap is the appearance of a so-called micromotion, which is associated with the movement of an electric charge in an alternating electric field[1, 133]. Mathematical details aside, the main problem with micromotion is that when an ion-atom collides, additional energy may be released. This issue has long caused a problem with the cooling of ion-atom systems to the quantum regime, because in this case, additionally, the quantum regime requires a lower temperature than for atoms. There are various sophisticated experimental techniques to compensate micromotion, but the best solution was to use a mixture with a very large mass ratio, such as ytterbium and lithium. This was proposed well before the experiment[68].

# 4

# YTTERBIUM ION AND LITHIUM ATOMS IN AMSTERDAM

## 4.1 IDEA OF THE EXPERIMENT

An experiment built at the University of Amsterdam by the Hybrid atom-ion quantum systems group under the supervision of Prof. Rene Gerritsma was crucial in the fundamental research of ion-atom systems. The experimental work on the ytterbium ion immersed in a cloud of ultracold lithium atoms conducted by the group finally led to the first ever observation of ion-atom collisions in the quantum regime, i.e. s-wave collisions. In the context of our collaboration with the Amsterdam group and our theoretical contribution to this achievement, it is reasonable to explain the details of the experimental setup that was built there. In the following sections, information on the idea of the experiment and technical details of its construction will be presented. Moreover, the results obtained in the experiment concerning the cooling process of the ion-atom system and their interpretation will be shown.

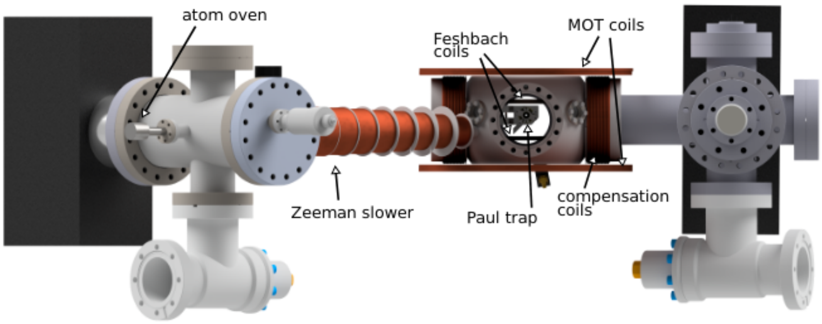

Figure 21: Experimental setup in $Yb^{+}/Li$ experiment in Amsterdam. From Ref.[134]

## 4.2 EXPERIMENTAL SETUP

Both cold atom and trapped ion systems have been successfully studied independently for a long time. Carrying out measurements simultaneously with cold atoms and ions is problematic and, as indicated earlier, it is currently only possible for mixtures with a large mass ratio. This is due to the fact that the charged ion in the Paul trap with an alternating electric field experiences additional movement, which may cause the release of additional energy during collisions with an atom. For this reason, the ion cannot reach a temperature that is low enough to talk about the quantum nature of the collisions. However, in the case of the $\mathrm{Yb}^+/\mathrm{Li}$ mixture, these problems were overcome and the quantum regime was successfully achieved in an experiment performed in Amsterdam. Fig.21 shows sketch of the experiment. Li atoms are heated from an oven and slowed down in a Zeeman slower towards the main chamber. Later they are combined with ytterbium ion trapped in the Paul trap. The trap can operate at frequencies in the range of: a typical radial potential $\omega_{rad} = 2\pi \times 100 - 350\mathrm{KHz}$ and an axial potential up to $\omega_{ax} = 2\pi \times 120\mathrm{kHz}$. The ion is cooled using the Doppler technique, while the cloud of $5 \times 10^3$ to $2 \times 10^4$ lithium atoms per spin in a mixture of states $|1/2, \pm 1/2\rangle$ and temperature of $T_a = 2 - 10\mu\mathrm{K}$ prepared in an optical dipole trap $50\mu m$ below the ion Fig.22. Finally the atoms are transported up by repositioning the dipole trap using piezo-controlled mirrors[135].

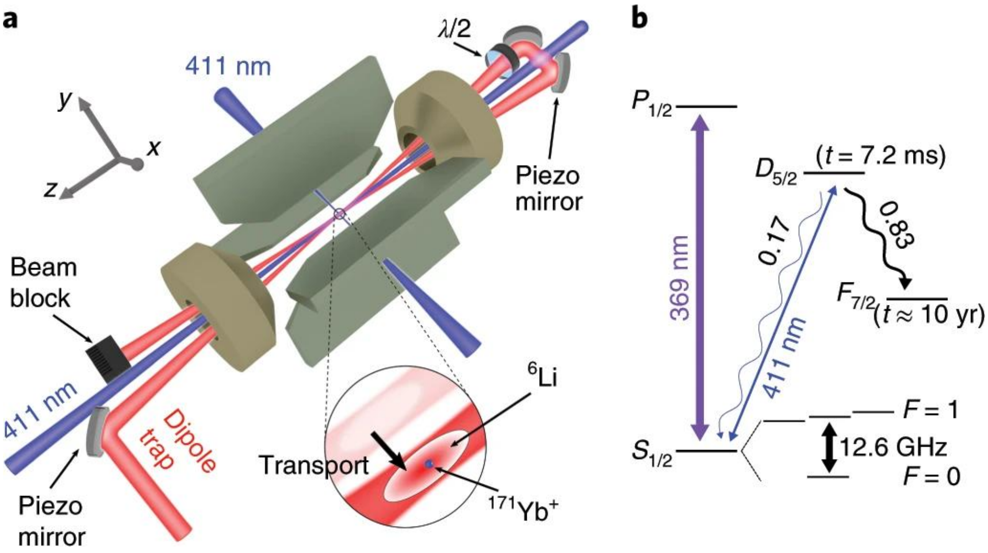

Figure 22: a. A cloud of ultracold $^6$Li atoms is prepared in an optical trap $50\mu m$ below a single ion in a Paul trap. The ion is then immersed in the atomic cloud by transporting the atom trap up using piezo-controlled mirrors. [134, 135] b. Diagram of ytterbium atomic transitions used in cooling and detection. From Ref.[135].

## 4.3 COOLING PROCESS

The experiment used Doppler cooling through the 369-nm atomic transition between states $S_{1/2}$ and $P_{1/2}$. The ion cooling process presented in the Fig.23 begins around 600 µK, which is roughly the Doppler cooling limit for this system. The ion is then immersed in a cloud of ultracold atoms and buffer gas cooling is performed. Af-

| Measured energy budget in terms of kinetic energy and collision energy | | |
|---|---|---|
| type of motion | $E_{kin}/k_B(\mu K)$ | $E_{col}/k_B(\mu K)$ |
| Radial secular ion | $2 \times 21(\pm 9))$ | $1.4(\pm 0.6)$ |
| Intrinsic micromotion | $2 \times 21(\pm 9)$ | $1.4(\pm 0.6)$ |
| Axial secular ion | $65(\pm 18)$ | $2.2(\pm 0.4)$ |
| Excess micromotion | $44(\pm 13)$ | $1.5(\pm 0.4)$ |
| Total ion energy | $193(\pm 42)$ | $6.6(\pm 1.4)$ |
| Atom temperature | $3/2 \times 2.3(\pm 0.4)$ | $3.3(\pm 0.6)$ |
| Total collision energy | - | $9.9(\pm 2.0)$ |

Table 1: Measured energy budget in terms of kinetic energy and collision energy in the $Yb^+/Li$ system. Data from Ref.[135].

ter a variable interaction time, the dipole optical trap is turned off, while the ion is transferred from the ground $S_{1/2}$ state to the long-lived $D_{5/2}$ state using the 411 nm atomic transition. Average kinetic energy is obtained by studying laser excitations as a function of pulse width. In particular, the occupation of thermally excited states causes mixing of the frequency components and thus damping of Rabi oscillations. Hence, information about temperature can be obtained by relating the observed excitations to a model assuming thermal distribution. Finally assuming ion's energy: $E_i = E_{sec} + E_{iMM} + E_{eMM}$, that is, the secular energy plus the energy due to the intrinsic (iMM) and excess micromotion (eMM) and collision energy given by: $E_{col} = \frac{\mu}{m_i}E_i + \frac{\mu}{m_a}E_a$ with $E_a = 3k_BT_a/2$, large mass ratio: $\mu \approx m_a \ll m_i$ we obtain relative collision energy in the quantum regime (see in Tab.1).

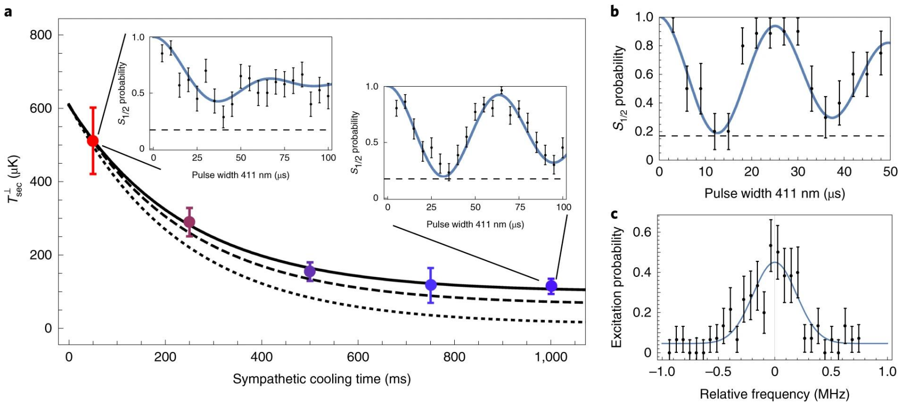

Figure 23: Ion cooling process: a. Ion temperature as a function of atom–ion interaction time, b,c, Measurement of radial ( $T^{\perp}_{sec} = 42(\pm 19)\mu K$) (b) and axial ( $T^{ax}_{sec} = 130(\pm 35)\mu K$) (c) temperatures after 1s of interaction time with an atomic cloud with $T_a = 2.3(\pm 0.4)\mu K$ and after adiabatic decompression of the radial ion trap potential. From Ref.[135].

# 5

# BARIUM ION AND LITHIUM ATOMS IN FREIBURG

## 5.1 IDEA OF THE EXPERIMENT

The experimental setup built in Freiburg allowed for the first ever observation of Feshbach ion-atom resonances using barium ion with lithium atoms. In this chapter, the concept of this experiment will be presented and the differences from the system built in Amsterdam will be indicated. We have seen before that in ion-atom sys-

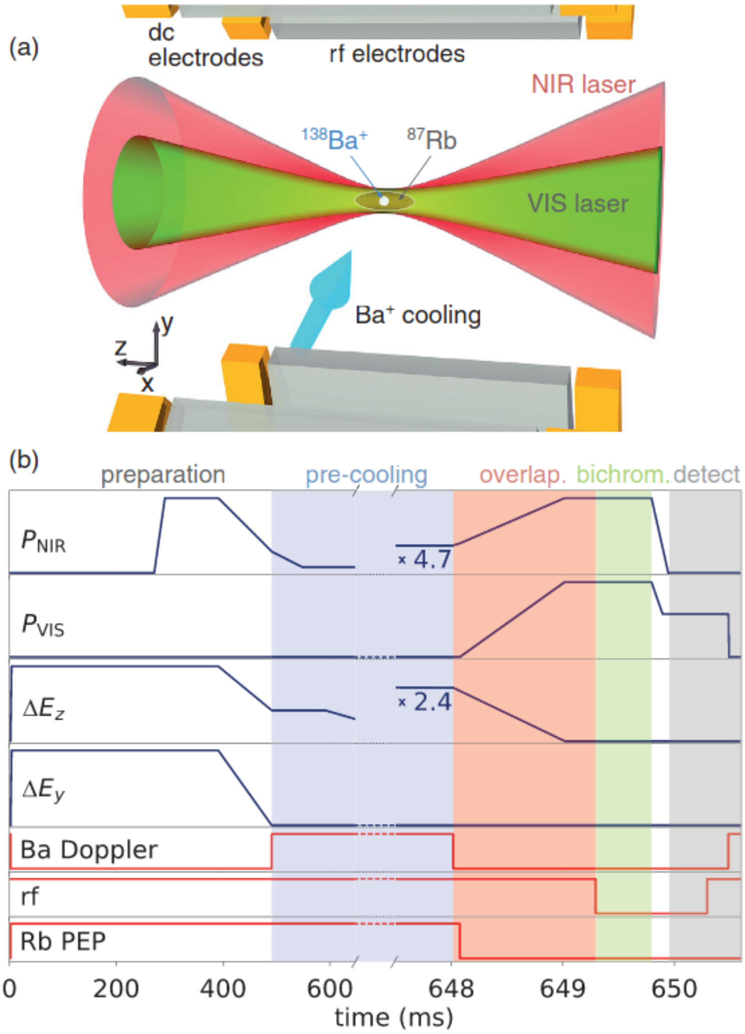

Figure 24: The experimental setup in Freiburg: bichromatic dipole traps (a) and the experimental protocol (b), details in text. Figure from Ref.[136].

tems, a significant obstacle in achieving the quantum regime is the so-called micromotion related to the presence of the radio-frequency trap. In Freiburg, even before measuring resonances, they tried a different approach based on the use of optical traps for both the ion and atoms. This approach has already been demonstrated in an experiment with the sympathetic cooling of barium ion in a rubidium atomic cloud[136], which was built on the basis of their previous experiments[137, 138]. The experimental setup is schematically shown in Fig.24. The experimental process consists of four successive stages: preparation, precooling, overlapping and bichromatic phase. They use two lasers VIS and NIR to simultaneously trap the barium ion and the rubidium atomic cloud. Initially, the barium ion is trapped in the linear Paul trap where the Doppler cooling process is carried out. Later the ion is transported to a bichromatic optical dipole trap, where the radio-frequency trap is turned off. They use $\Delta E_z$ and $\Delta E_y$ electric offset fields in the z and y directions. Finally, they measure the survival of the ion by transport back to the radio-frequency trap and fluorescence imaging on charge-coupled device. This experiment, in which the Freiburg group prepared a mixture of barium ion with a cloud of rubidium atoms at $370\mu K$ after Doppler cooling and then demonstrated $100\mu K$ cooling after one collision, was a prerequisite for the resonance measurement.

## 5.2 EXPERIMENTAL SETUP

The experimental setup designed to observe the Feshbach resonances[93] (Fig.25) is based on the previously discussed scheme. The lithium-6 atomic cloud is initially prepared in a magneto-optical trap and then transferred to the crossed optical dipole trap (xODT). Using optical pumping, the atoms are prepared in the lowest hyperfine states: $|1\rangle = |f_{Li} = 1/2, m_f^{Li} = 1/2\rangle$ and $|2\rangle = |f_{Li} = 1/2, m_f^{Li} = -1/2\rangle$. Using evaporative cooling, we get $40 \times 10^3$ $^6$Li atoms at a temperature of $(1-3)\mu K$. The lithium atomic cloud is finally prepared in the $|2\rangle$ state by using spin-selective absorption imaging of the state $|1\rangle$. A single barium-138 ion is loaded into the radio-frequency trap ($\Omega_{rf} = 2\pi \times 1.433 MHz$, and secular frequencies $\omega_{x,y,z}^{Ba^+} = 2\pi \times \{123, 122, 7.6\} kHz$). The ion is cooled down to the Doppler limit (about $365\mu K$) using the $6S_{1/2} \rightarrow 6P_{1/2}$ transition ($493nm$). Finally, the ion is prepared in an incoherent mixture of states: $|6S_{1/2}; s^{Ba^+} = 1/2, m_s^{Ba^+} \pm 1/2\rangle$. The barium ion is efficiently polarized into state: $|s^{Ba^+} = 1/2, m_s^{Ba^+} - 1/2\rangle$ during first few collisions. The ion and atoms can interact with each other for a time in the range of [100,300] ms.

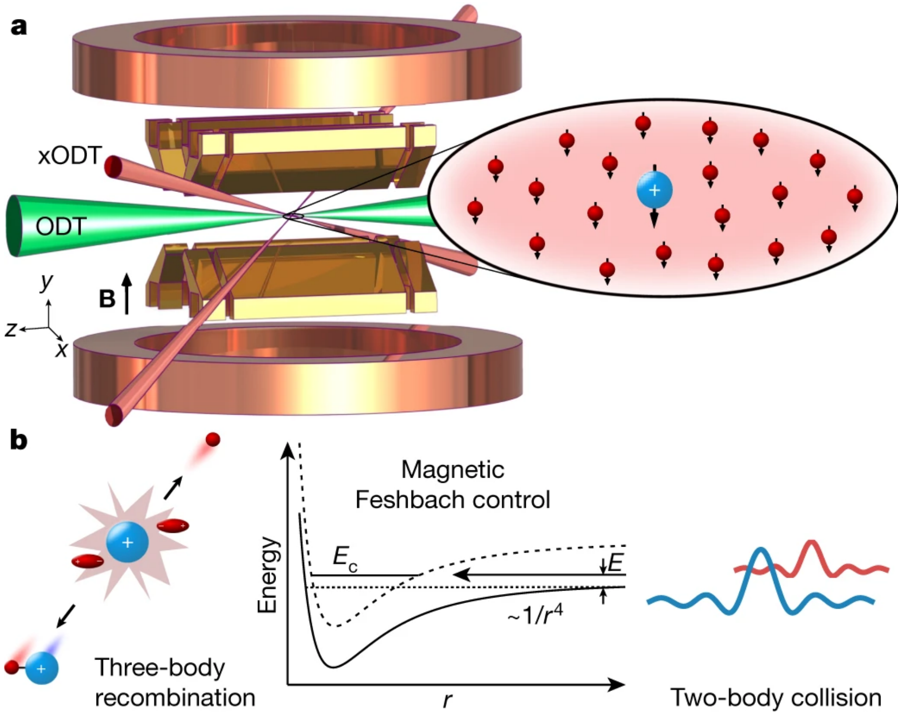

Figure 25: Observation of Feshbach resonances between a single ion and ultracold atoms: experimental setup (a), barium ion stored in rf-trap or optical dipole trap and atomic cloud in the crossed optical dipole trap (xODT), a homogeneous magnetic field generated by set of Helmholtz-coils. By tuning magnetic field, interaction time or atomic density we observe different processes like two-body elastic collision or inelastic three-body recombination (b). Figure from Ref.[93]

## 5.3 DETECTION OF ATOM-ION FESHBACH RESONANCES

Feshbach resonances are identified by barium ion loss spectroscopy. In order to find the position of the resonances, the magnetic field values are searched for step by step every 400 mG. For each localized resonance, the interaction time is selected so as to obtain a survival probability of the ion less than 50%. During the experimental process, the range of the magnetic field [70,330] G was investigated and 11 resonances were found. The survival probability of the ion in a radio-frequency trap is measured using a fluorescence detection, another possibility is to transfer the ion to the optical dipole trap (ODT). The relatively shallow ODT causes a limit on kinetic energy, resulting in a finite optical trapping probability, which allows the efficiency of sympathetic cooling to be tested. Details on identifying the nature of individual resonances are presented in the following chapters.

# Part IV

# RESULTS

# 6

# BUFFER GAS COOLING OF A TRAPPED ION TO THE QUANTUM REGIME

In this chapter we will present the results of the performed calculations and the details of the simulations made for the experiment with cooling the mixture of ytterbium ion and lithium atoms to the quantum regime. The results presented here were the basis for the work with the experimental group from Amsterdam[135]. Not all calculations presented here were included in the publication, but they were necessary because in fact guiding and confirmation of the experimental results was a longer way.

## 6.1 INTRODUCTION

The starting point for calculating the ion-atom collision properties is to identify the appropriate electronic states and to have interaction potentials.

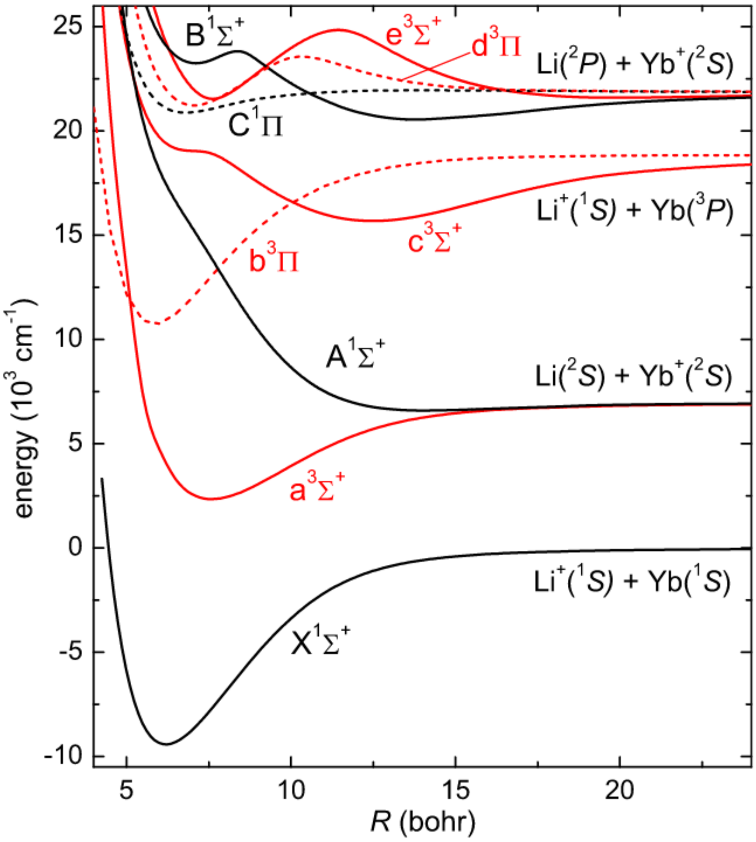

Figure 26: Nonrelativistic potential energy for $(\mathrm{LiYb})^+$. From Ref.[69].

The interaction potentials have already been calculated by Michał Tomza and applied in the work on the cooling perspectives of the ytterb-lithium mixture[69] and in the theoretical work predicting certain collision properties[73]. In our case, we are interested in the interaction between the ground state ytterbium ion with the ground state lithium atom (Fig.26). The result is an interaction in two electronic states: singlet ($A^1\Sigma^+$) and triplet ($a^3\Sigma^+$). The binding energies of both states differ significantly[69], the singlet state is weakly bound, having the binding energy: $358 \mathrm{cm}^{-1}$. In the case of the triplet state, the binding energy is: $4609\ \mathrm{cm}^{-1}$, what can be justified on the basis of molecular orbitals analysis.

## 6.2 HYPERFINE STRUCTURE OF THE YB$^+$/LI MIXTURE

In order to simulate ion-atom collisions, we need knowledge about the structure of the energy levels of the colliding components and the mixture. This is necessary because we want to choose the proper parameters corresponding to the experimental situation. In experimental conditions, collisions take place in a magnetic field, so the energy states we are interested in are the appropriate configurations of electron and nuclear spins, in effect creating hyperfine states. We diagonalize the following Hamiltonian in the basis of electron and nuclear spins: $|\psi\rangle = |S, m_S\rangle\, |I, m_I\rangle$

$$\hat{H} = g_e \mu_B B_0 \hat{S}_z - g_n \mu_N B_0 \hat{I}_z + hA \hat{I} \cdot \hat{S}, \tag{65}$$

where: $g_e, g_N$ - electron and nucler g-factor, $\mu_B, \mu_N$ - Bohr and nuclear magneton, $B_0$ - magnetic field and $A$ - hyperfine coupling. We take advantage of the fact that the hyperfine-coupling part of the Hamiltonian can be written using the ladder operators:

$$\hat{H}_{hf} = hA \left( \hat{I}_z \cdot \hat{S}_z + \frac{1}{2} \left( \hat{I}_+ \cdot \hat{S}_- + \hat{I}_- \cdot \hat{S}_+ \right) \right). \tag{66}$$

Since the Zeeman terms are diagonal in the chosen basis, this form of hyperfine coupling results in a convenient form of the Hamiltonian matrix from which we easily get hyperfine states for Lithium, Iterbium, Lithium-Iterbium mixture, and Barium in the next chapter. On the following pages we present the hyperfine structure of Lithium-6, Lithium-7, Ytterbium-171 and Ytterbium-174, and then mixtures of Lithium-6 with Ytterbium-171 and 174, which were considered in the experiment in Amsterdam. The presented results are divided depending on the total spin projection of the mixture, which is conserved in this type of collision. The knowledge of hyperfine states of mixtures is necessary in guiding and analysis of spin exchange processes observed in the experiment.

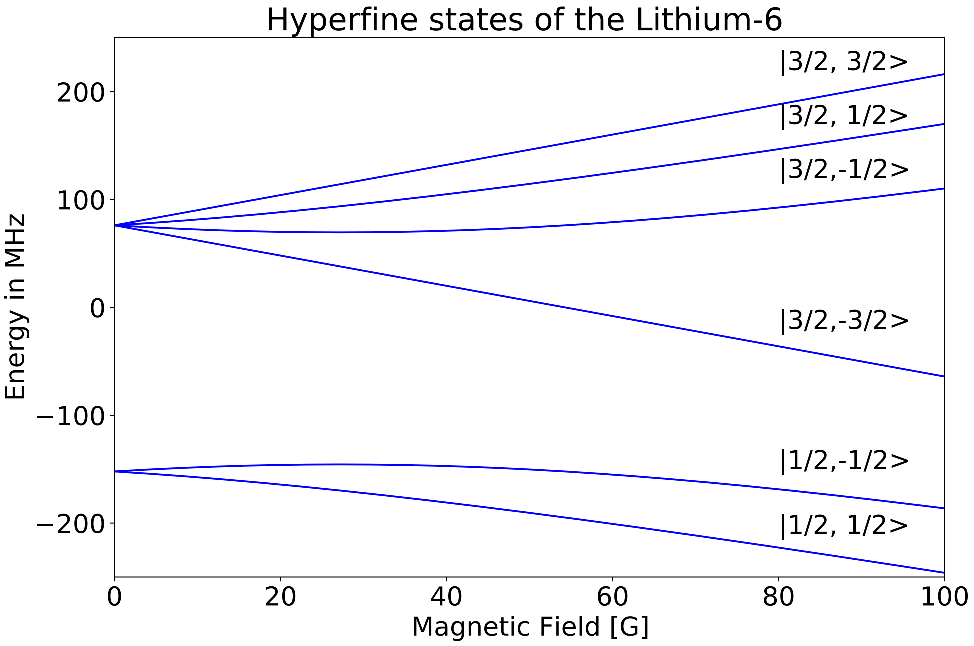

Figure 27: Hyperfine states of the Lithium-6 with labels $|f, m_f\rangle$.

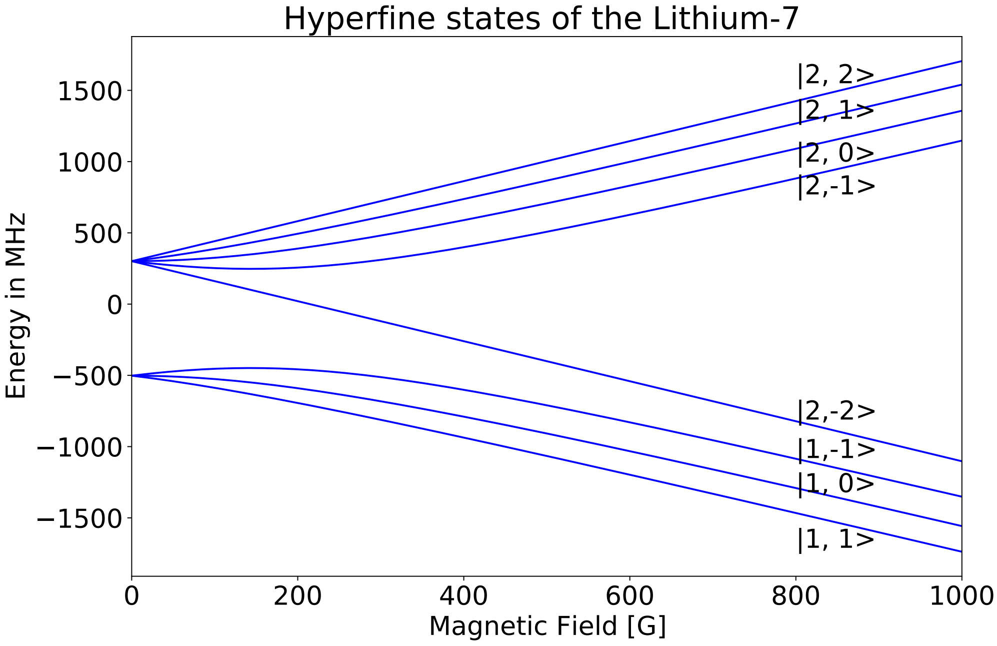

Figure 28: Hyperfine states of the Lithium-7 with labels $|f, m_f\rangle$.

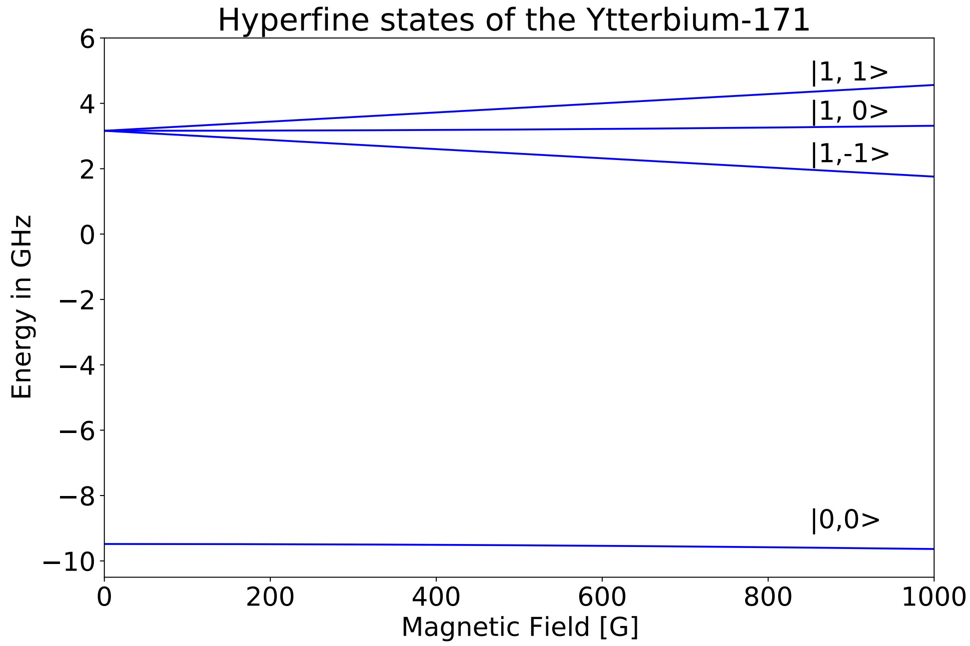

Figure 29: Hyperfine states of the Ytterbium-171 with labels $|f, m_f\rangle$.

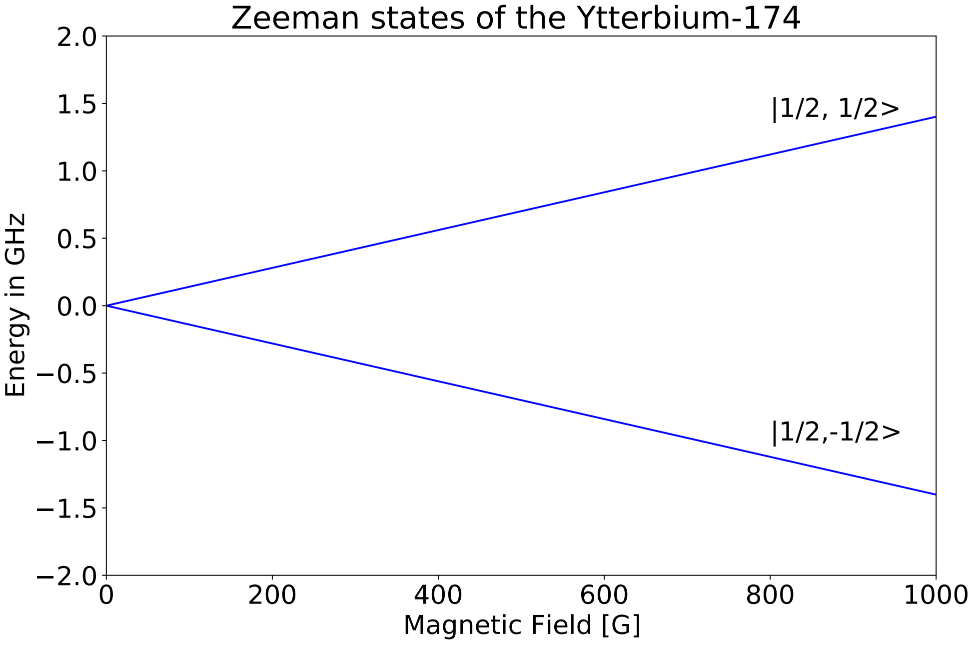

Figure 30: Hyperfine states of the Ytterbium-174 with labels $|f, m_f\rangle$.

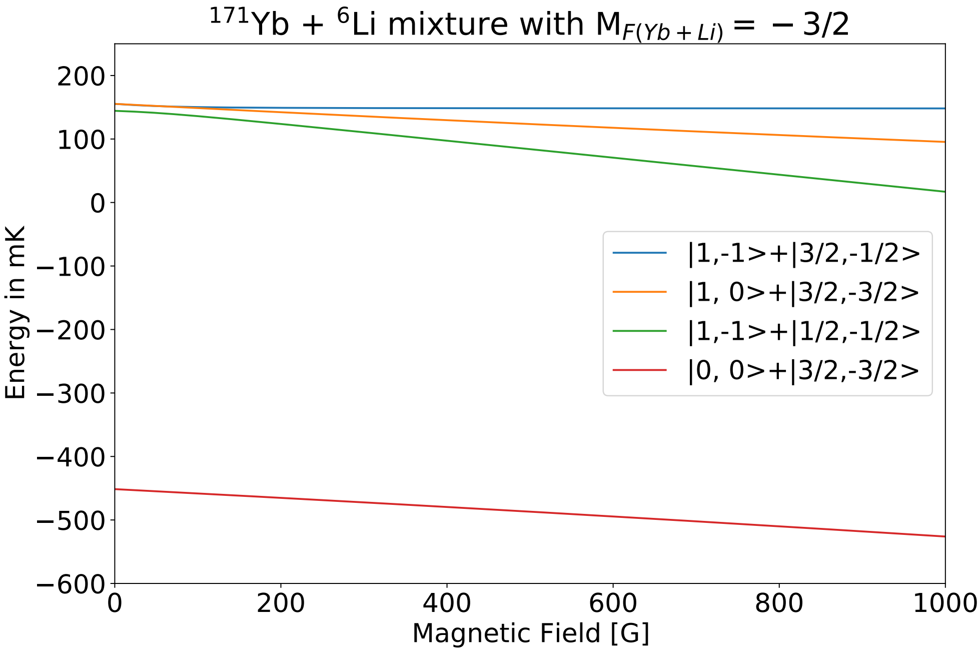

Figure 31: Hyperfine states of the Ytterbium-Lithium mixture with total $M_F = -3/2$.

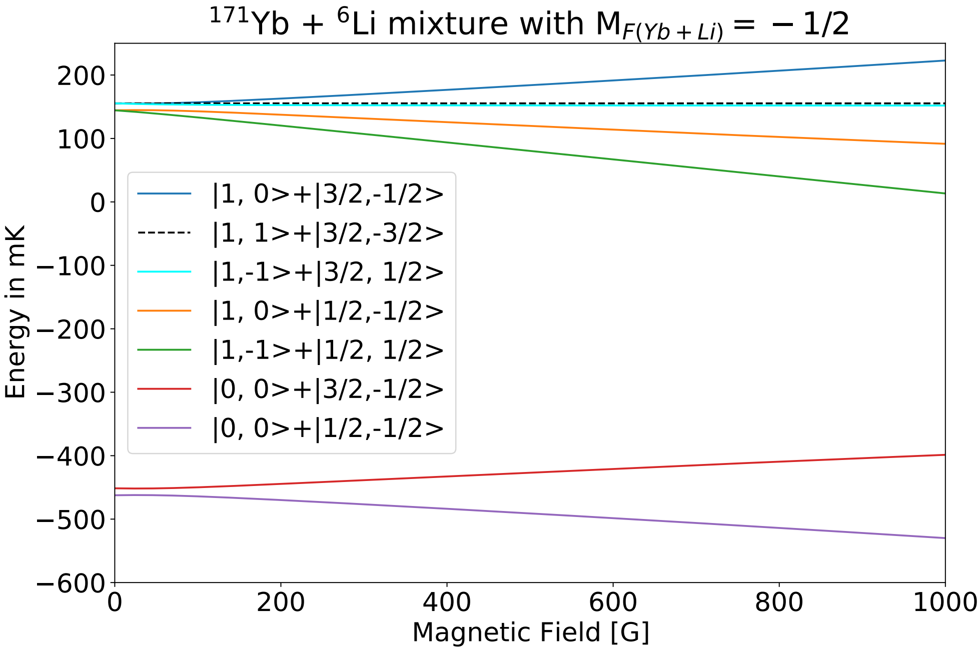

Figure 32: Hyperfine states of the Ytterbium-Lithium mixture with total $M_F = -1/2$.

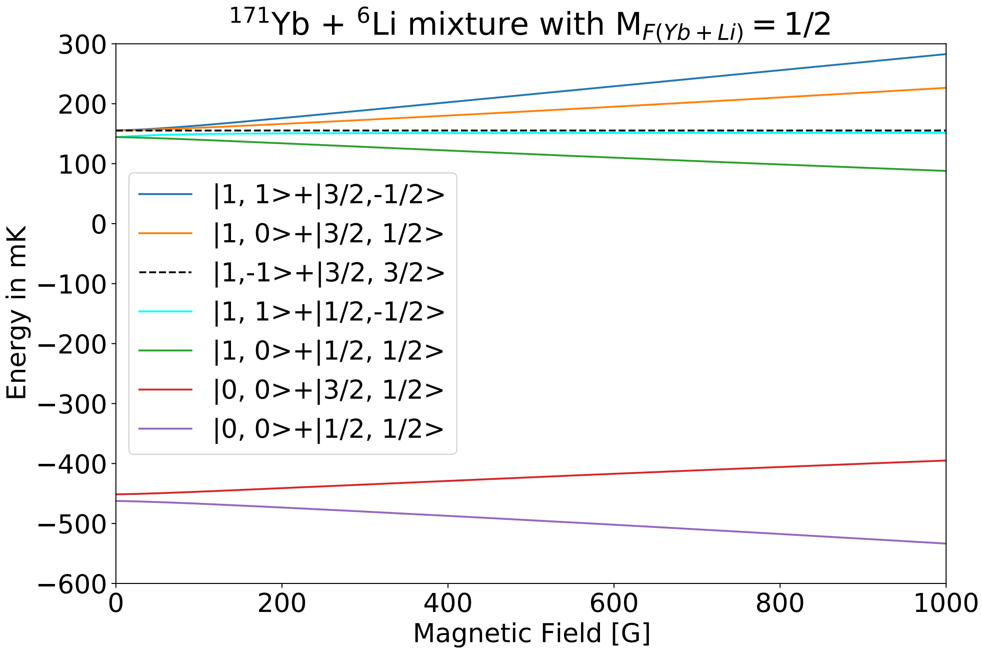

Figure 33: Hyperfine states of the Ytterbium-Lithium mixture with total $M_F = 1/2$.

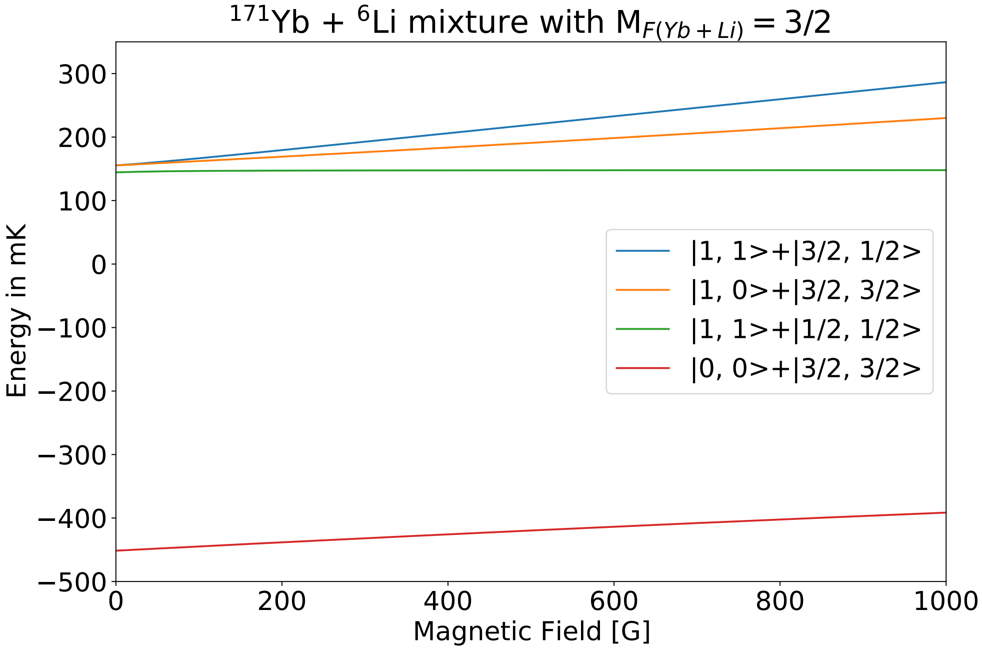

Figure 34: Hyperfine states of the Ytterbium-Lithium mixture with total $M_F = 3/2$.

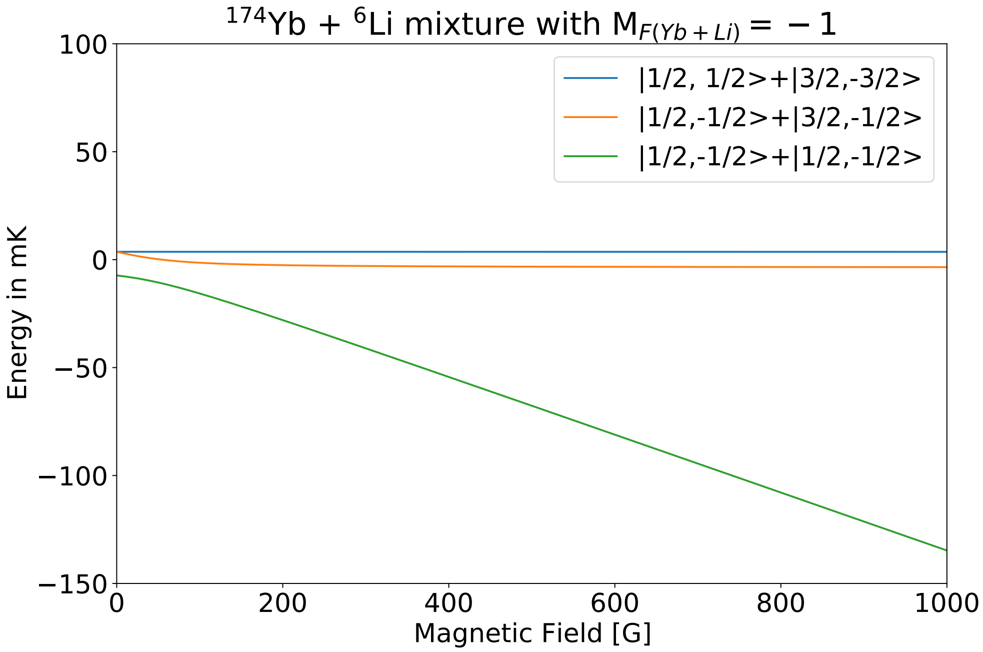

Figure 35: Hyperfine states of the Ytterbium-Lithium mixture with total $M_F = -1$.

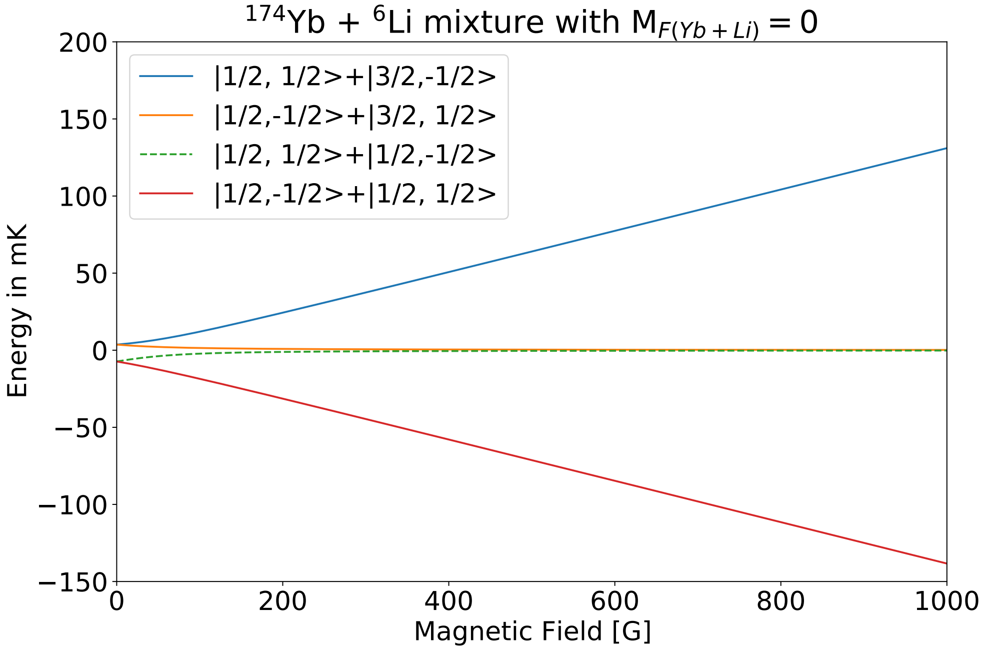

Figure 36: Hyperfine states of the Ytterbium-Lithium mixture with total $M_F = 0$.

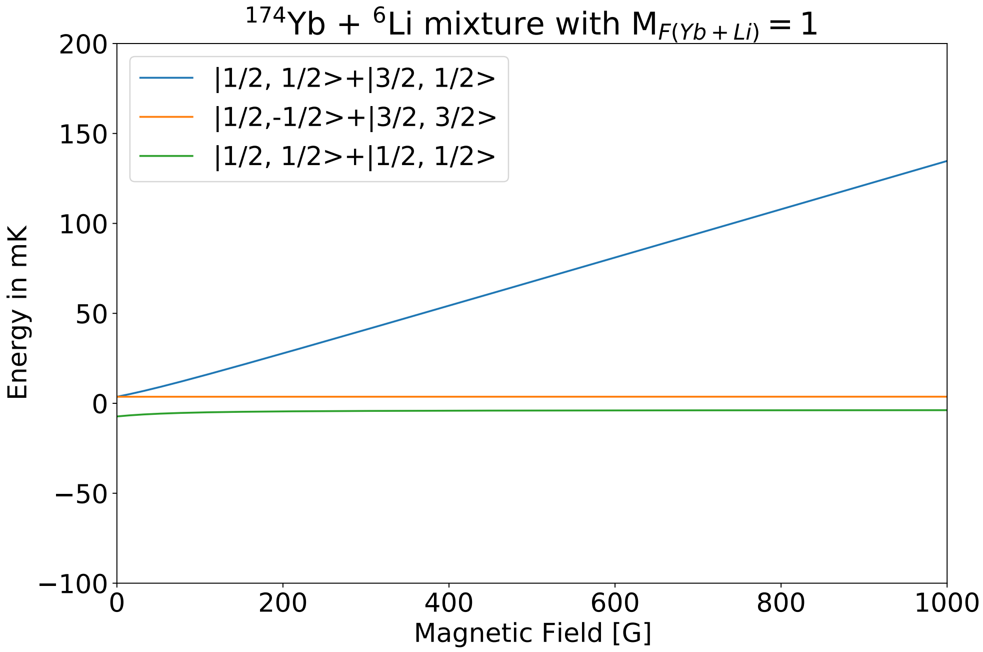

Figure 37: Hyperfine states of the Ytterbium-Lithium mixture with total $M_F = 1$.

## 6.3 MULTICHANNNEL QUANTUM SCATTERING CALCULATIONS

In this section, we present the quantum scattering calculations made for a mixture of Lithium-6 with Ytterbium-171. This mixture, due to its very large mass ratio, was proposed as one of the promising candidates for cooling an ion-atom system to a quantum regime. It is this feature that allows to minimize the micromotion in the ion trap turned out to be the key in the experiment.The calculations that were made for the experiment were initially burdened with inaccuracies related to the lack of knowledge of the scattering lengths and the number of Langevin collisions. This is due to the fact that the interaction potentials are not precise enough to calculate the theoretical value of the singlet and triplet scattering lengths. Instead, the scattering length can be set to a specific value by scaling the potential. Then, with such a selected potential, we solve the Schrodinger equation in the full spin base by its propagation using the Numerov method as described in the previous chapters. In this way, we can create a grid representing the scattering length values for which we have calculated values of the spin exchange probability corresponding to the successive collision energies. The third parameter remains the unknown number of Langevin collisions, which must also be calculated. It is not possible without the use of experimental data, they are included in the analysis by applying the $\chi^2$ function to test the consistency of the spin-exchange probability prediction for a given

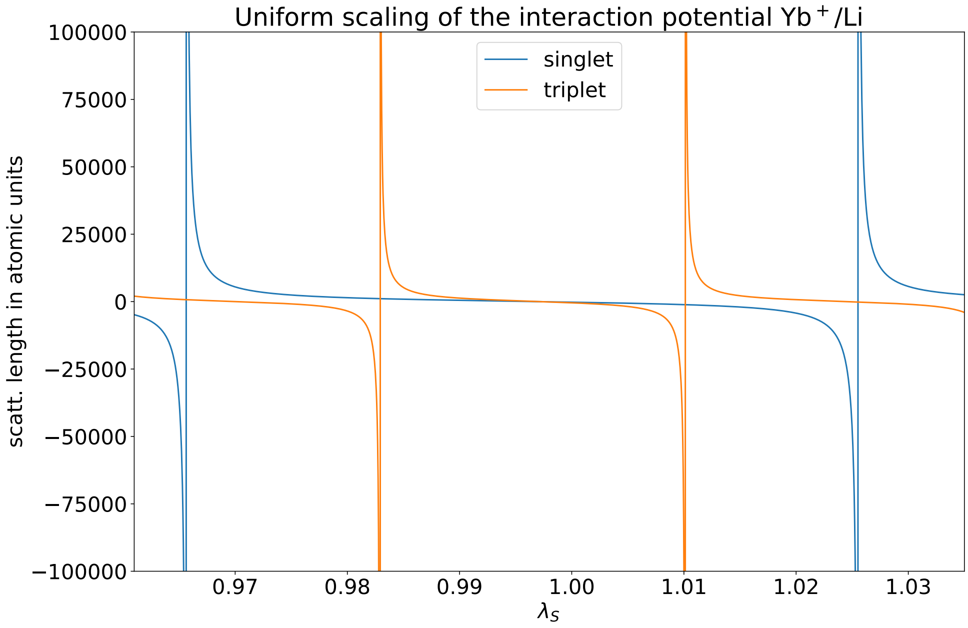

Figure 38: Uniform scaling of the Yb$^+$/Li interaction potential.

collision energy with respect to the experimental observation. The $\chi^2$ function was calculated in the space of the three parameters by the interpolation techniques used, it allowed to locate the global minimum that corresponds to the theoretical parameters describing the experimental observation. Then, for the minimum found in this way, a number of tests were carried out, including direct simulation with the parameters found to exclude errors related to interpolation. The found minimum clearly indicates one possible set of parameters. The curve of the dependence of the spin-exchange probability versus the collision energy fits very well with the experimental data and confirms their quantum character. In the classical theory of ion-atom collisions, the above dependence should remain constant, here we see a clear dependence on the collision energy.

### 6.3.1 *Uniform scaling of the potential*

As mentioned earlier, the interaction potentials are not precise enough to calculate the scattering lengths. Instead, we use uniform potential scaling to set a given scattering length

$$V_S(r) \to \lambda_S V_S(r). \tag{67}$$

The scattering lengths for uniform singlet and triplet potential scaling are shown above (Fig.38). The scattering lengths are given in atomic units, in further analyzes we will use the scattering lengths expressed by the characteristic length scale for the $\mathrm{Yb}^+/\mathrm{Li}$ system: $R_4 = \sqrt{\frac{2\mu C_4}{\hbar^2}} = 1319.2\mathrm{a.u.}$ .

### 6.3.2 *Spin-exchange rates*

As we know from the description of the experiment, the cloud of cold lithium atoms is prepared in a 50/50 ratio in the two lowest spin states: $|1/2, 1/2\rangle$ and $|1/2, -1/2\rangle$. At the same time, we start the measurement with the ytterbium ion in the state: $|1, -1\rangle$. Therefore, we consider the spin-exchange processes that change the initial state of the ytterbium ion to the state: $|0, 0\rangle$, including the transition through state $|1, 0\rangle$ and a much faster decay to $|0, 0\rangle$. Taking into account the above conclusions and corresponding atomic states, we finally operate in two subspaces of the total angular momentum projection: $M_F = -1/2$ nad $M_F = -3/2$. Fig.39 shows schematically how multichannel quantum scattering calculations were performed. Namely, we start with the input state marked in red in the middle, then we examine the transitions both directly to $|0, 0\rangle$ and transitions through $|1, 0\rangle$. Since we have a mixture of lithium atoms with equal spin state proportions, we add both spin exchange rate paths with equal weights. Theoretical calculations are made for a collision energy ranging from a few microkelvins to over a thousand microkelvins, including 20 partial waves. As mentioned earlier, the scattering lengths were used as parameters in the calculations. Then the calculated values were convoluted with the energy distribution of the ion associated with the applied external electric field

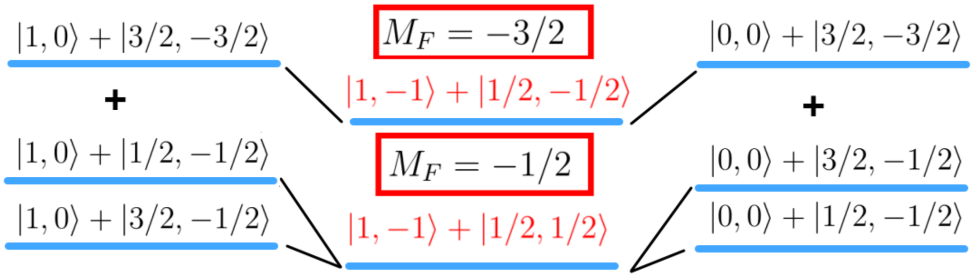

Figure 39: Structure of energy levels studied in the spin-exchange processes observed in Amsterdam.

$$\bar{K}(\bar{E}, a_S, a_T) = \int_{E_0}^{E_0+E_{eMM}} P_{E_{eMM}}(E - E_0) K(E, a_S, a_T) dE. \tag{68}$$

And finally, the probability of detecting the ion in the $|0, 0\rangle$ spin state after preparing it in the $|1, -1\rangle$ state:

$$S(\bar{E}, a_S, a_T, n_L) = 1 - \exp(-n_L \bar{K}(\bar{E}, a_S, a_T)/K_L), \tag{69}$$

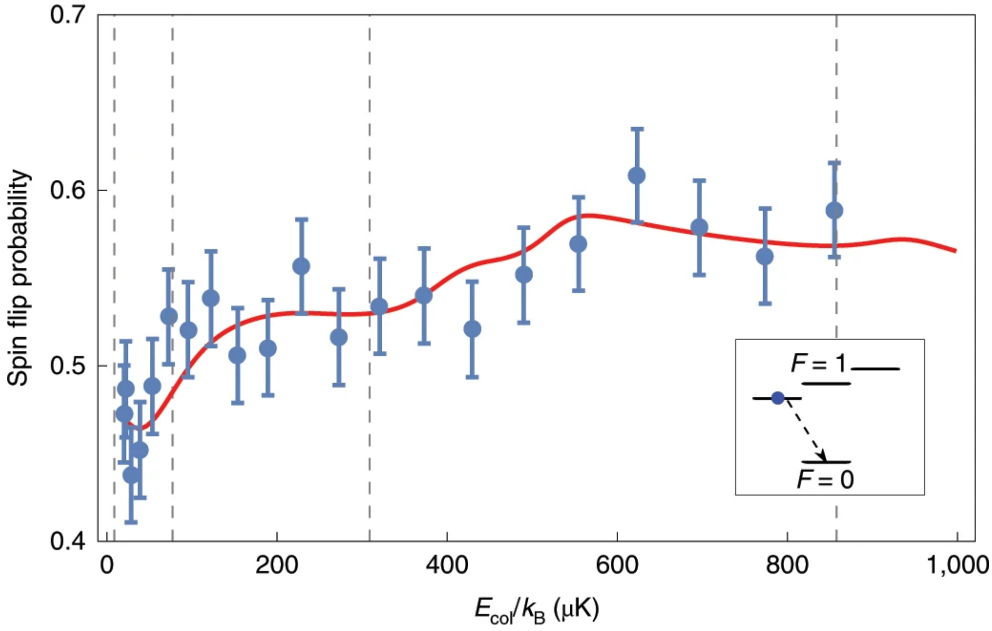

Figure 40: Spin exchange rate in $Yb^+/Li$ experiment in Amsterdam. Experimental points and theoretical curve. From Ref.[135].

where $n_L$ is the number of Langevin collisions and $K_L = 2\pi\sqrt{C_4/\mu}$ is the Langevin collision rate coefficient.

Final spin-exchange probabilities optimized for the best parameter configuration are shown together with the experimental data in Fig.40. We see the direct dependence of spin exchange on the collision energy, which is a feature of quantum scattering. According to Langevin's theory[139], a similar behaviour is not observed in classical ion-atom collisions. This gives us together with observation of shape resonances a significant confirmation on the theoretical and experimental level that we are dealing with collisions in the quantum regime. The figure above additionally shows the height of the centrifugal barrier for partial waves with l = 1,2,3,4 which is defined[1]:

$$E_l^{max} = \frac{l^2(l+1)^2}{4}E_4 \tag{70}$$

where: $E_4 = \frac{\hbar^2}{2\mu R_4^2}$. Hence it can be seen that we are indeed in a regime of few partial waves. However, as mentioned earlier, the red curve in the figure corresponds to the optimal parameters, in order to find it, calculations had to be made for the full set of possible parameters. For each set of parameters, convolutions were performed with the experimental ion energy distribution, and then the spin exchange probability was calculated. On the basis of these results, using

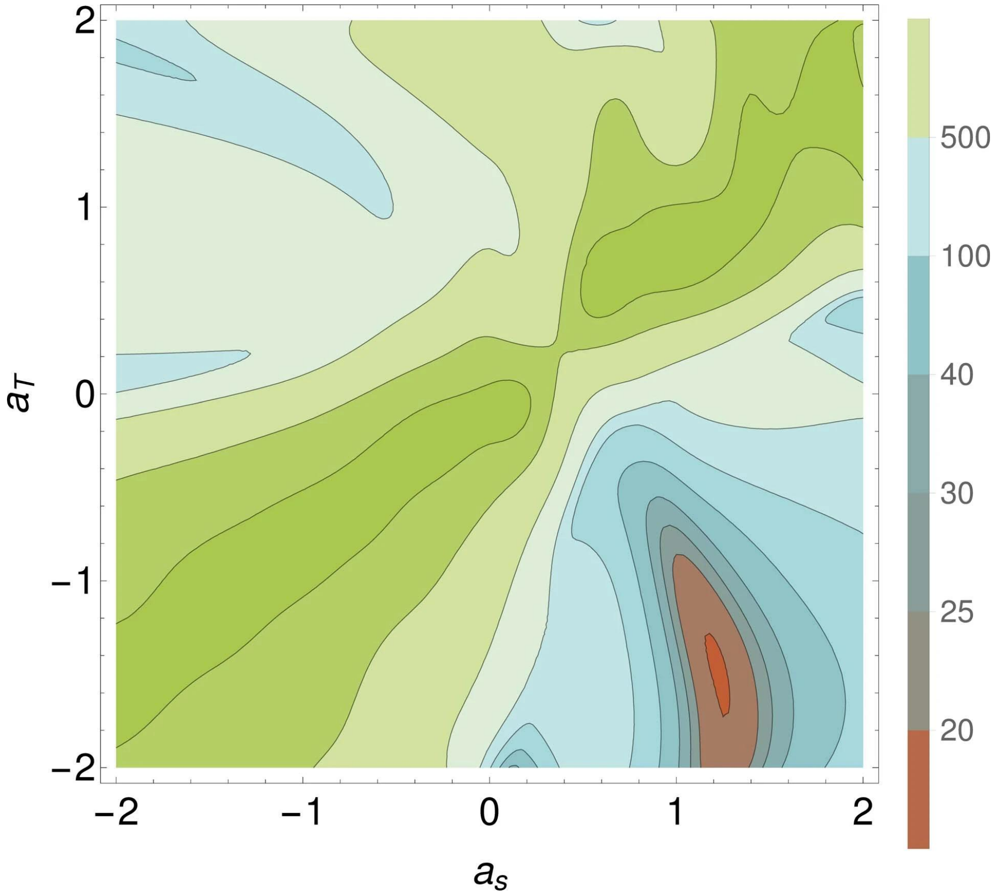

Figure 41: $\chi^2$ as a function of the singlet $a_S$ and triplet $a_T$ scattering lengths with the number of Langevin collisions optimized for each set of scattering lengths. From Ref.[135].

$\chi^2$ analysis, a map was obtained indicating the most optimal region in the parameter space

$$\chi^2(a_S, a_T, n_L) = \sum_{i=1}^{N_{exp}} \left( \frac{S_{exp}(\bar{E}_i) - S(\bar{E}_i, a_S, a_T, n_L)}{\sigma_i} \right)^2 . \tag{71}$$

These results are shown in Fig41, where they clearly indicate the area ($\chi^2$ minimum) around scattering lengths: $a_S = 1.2(\pm 0.3)R_4$, $a_T = -1.5(\pm 0.7)R_4$ and number of Langevin collisions: $n_L = 1.2(\pm 0.4)$. The uncertainties of the predicted values were obtained by imposing that $\chi 2$ gives a P value equal to or better than 0.05.

To better illustrate the fact that the above parameters were the only optimal ones, we present Fig.42 and Fig.43 of the spin exchange probability depending on the scattering lengths and the number of collisions in comparison to the optimal value and experimental data.

We can see that a small change in the parameters causes a significant deviation of the curve from the experimental data. When we change the number of collisions, having the scattering lengths optimal, the curve moves up or down. On the other hand, in the case of

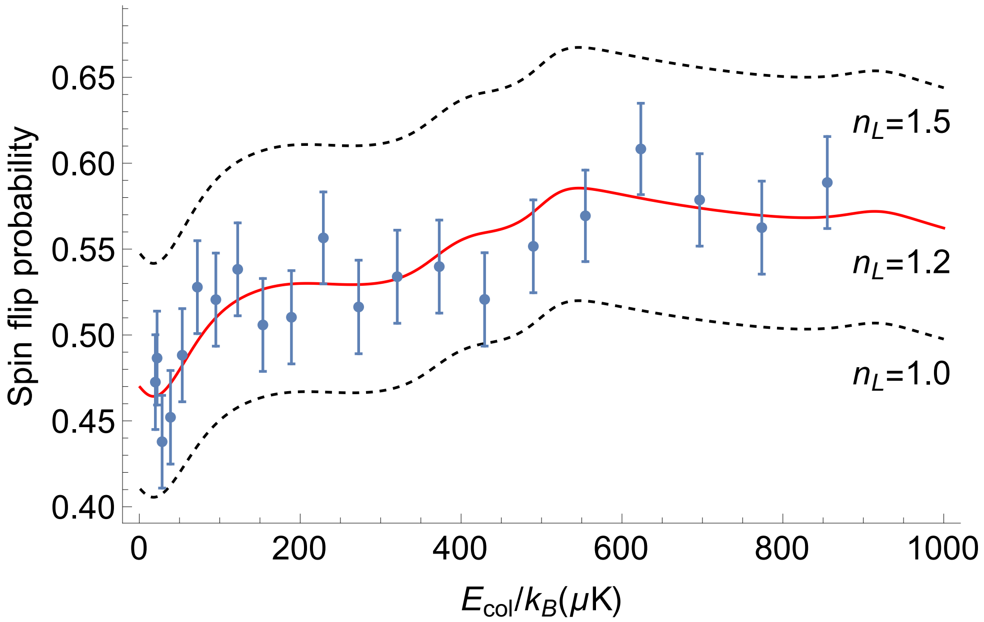

Figure 42: Spin exchange rate in Yb$^+$/Li experiment in Amsterdam: dependence on number of collisions.

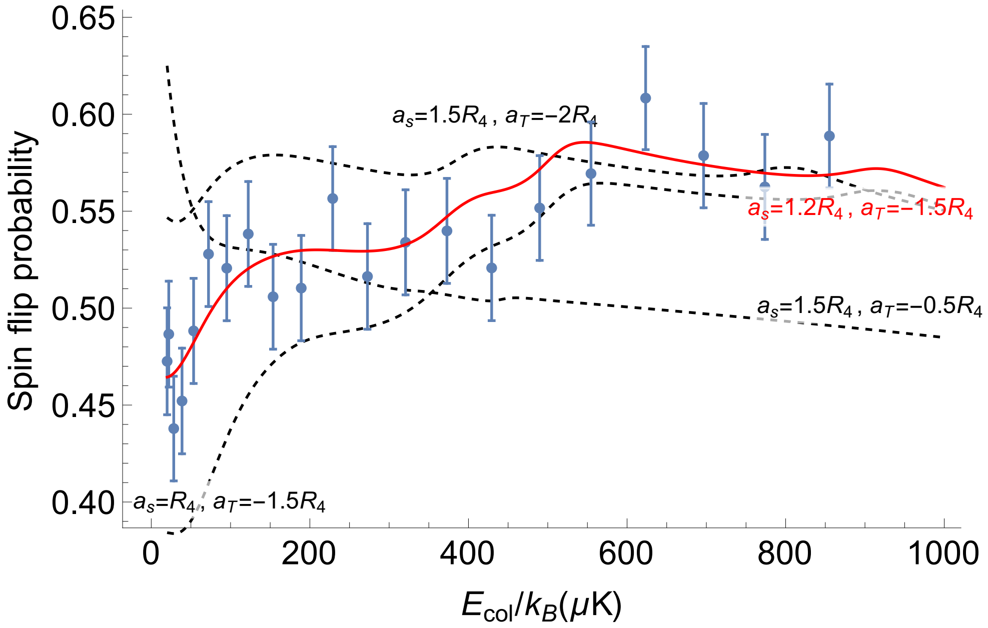

Figure 43: Spin exchange rate in Yb$^+$/Li experiment in Amsterdam: dependence on scattering length.

changing the scattering length while maintaining the optimal number of collisions, the curve both shifts and changes its shape completely. The behavior of the spin exchange curve is fully consistent with the image that emerges from the $\chi^2$ map. We have only one optimal set of parameters, moving in each direction causes a drastic increase in $\chi^2$, thus completely departing from the explanation of the experimental results. Thus, we justified the actual first observation of ion-atom collisions in the quantum regime and first-ever shape resonances in such a system.

### 6.3.3 *Feshbach resonances*

In this paragraph, the last one about the ytterbium-lithium mixture, we will provide an estimate of the position of the Feshbach resonances. Using the universal properties of the ion-atom interactions and the quantum-defect theory, a universal spectrum of bound states can be obtained[140]. Based on the above publication, we can estimate the limitation for the least-bound vibrational states in the ion-atom system. Then the intersection of bound states corresponding to the Feshbach resonance should take place between these energies. For the few of the least-bound states, we have the following estimate:

$$\begin{aligned} B_{-1} &= -105.81 * E_4, \\ B_{-2} &= -1179.9 * E_4, \\ B_{-3} &= -5207.5 * E_4, \\ B_{-4} &= -15308 * E_4. \end{aligned} \tag{72}$$

This approach was selected for the initial phase of identifying areas where Feshbach resonances may be present in an experimental context. The results are shown in Figs.44-49, which relates to the combination of Ytterbium-171 and Ytterbium-174 with lithium-6, all spin projections are included. The analysis of the Feshbach resonances carried out in this way had some value when we did not know the scattering lengths. This gave us an overall estimate of potentially interesting ranges of magnetic fields. Once we had theoretical scattering lengths values, we were able to perform more accurate calculations, results were presented in Figs.50-51 for Ytterbium-171 and $M_F = 1/2$ or $M_F = -1/2$. The elastic collision rate was calculated as a function of the magnetic field, these are two-body processes, but they provide information on the occurrence of resonance, also associated with the scattering length explosion, for a specific value of the magnetic field. Ultimately, the Feshbach resonances were not measured in Amsterdam in the system of Ytterbium-Lithium mixture yet. For technical and other reasons, the group focused on other project than the Feshbach resonances project. At the same time, our collaboration with the Freiburg group resulted in the first measurement of resonances in $Ba^+/Li$ mixture, what will be the subject of the next chapter.

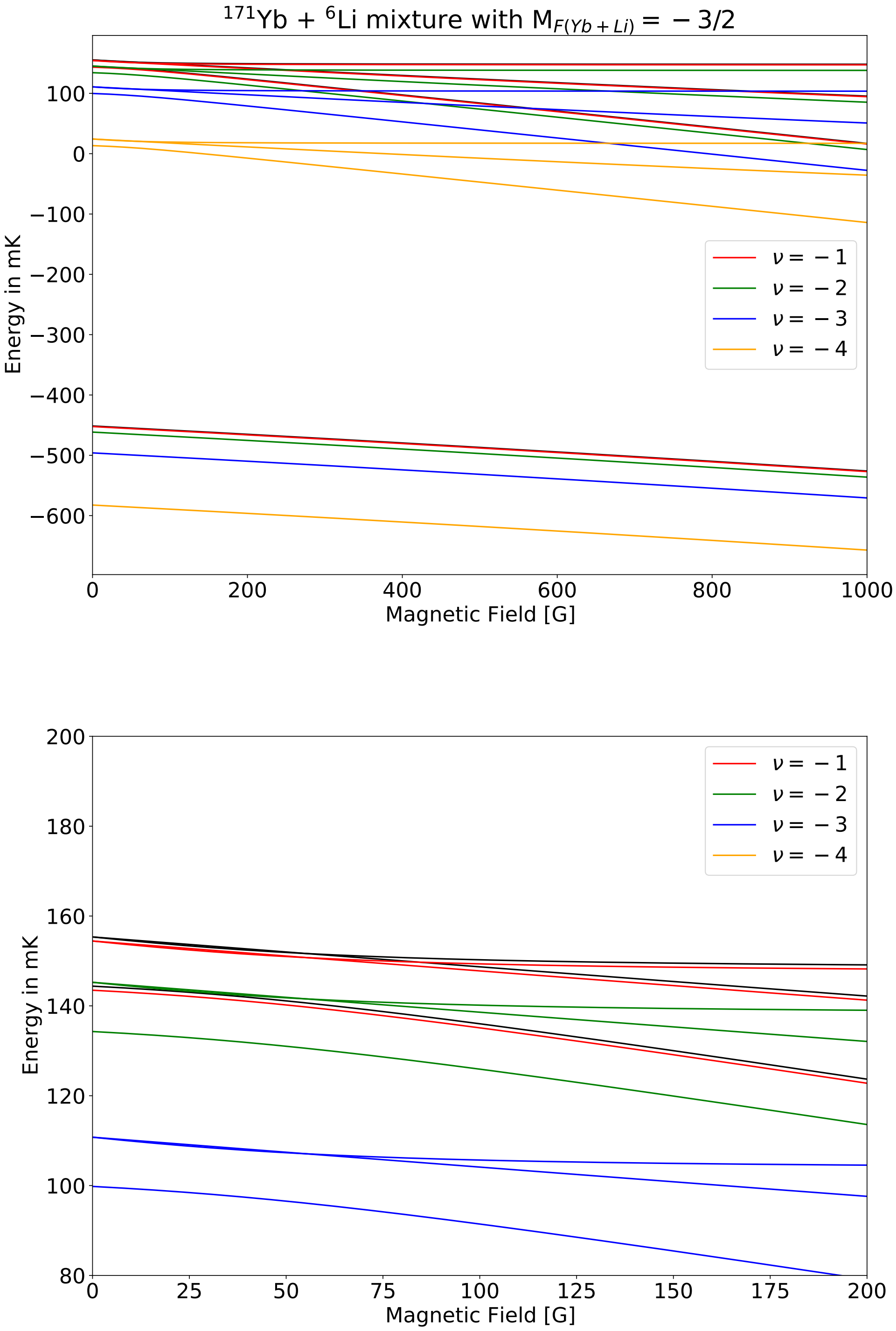

Figure 44: Hyperfine states of the Ytterbium-Lithium mixture with $M_F = -3/2$ and four the least-bound states: full range and zoom.

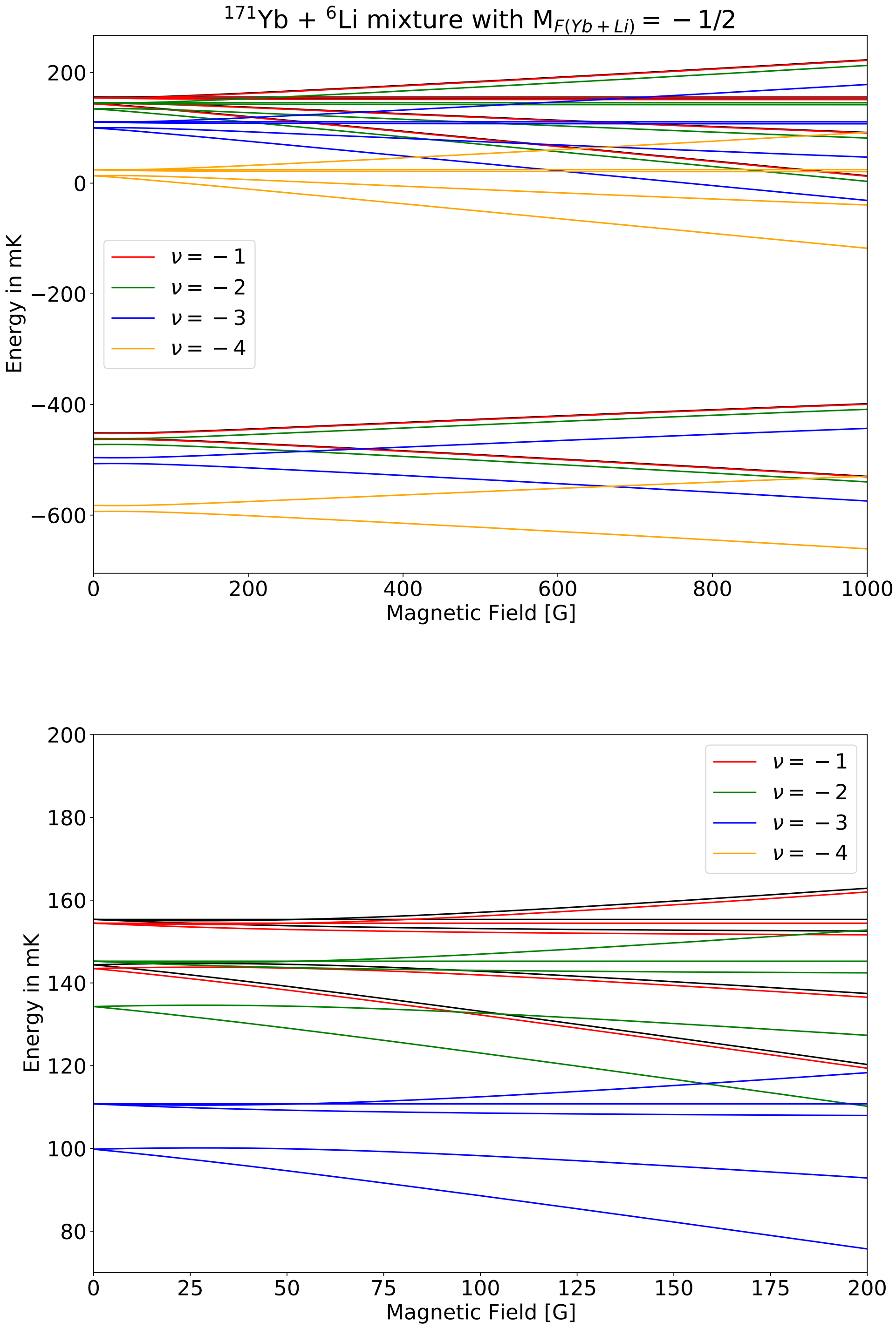

Figure 45: Hyperfine states of the Ytterbium-Lithium mixture with $M_F = -1/2$ and four the least-bound states: full range and zoom.

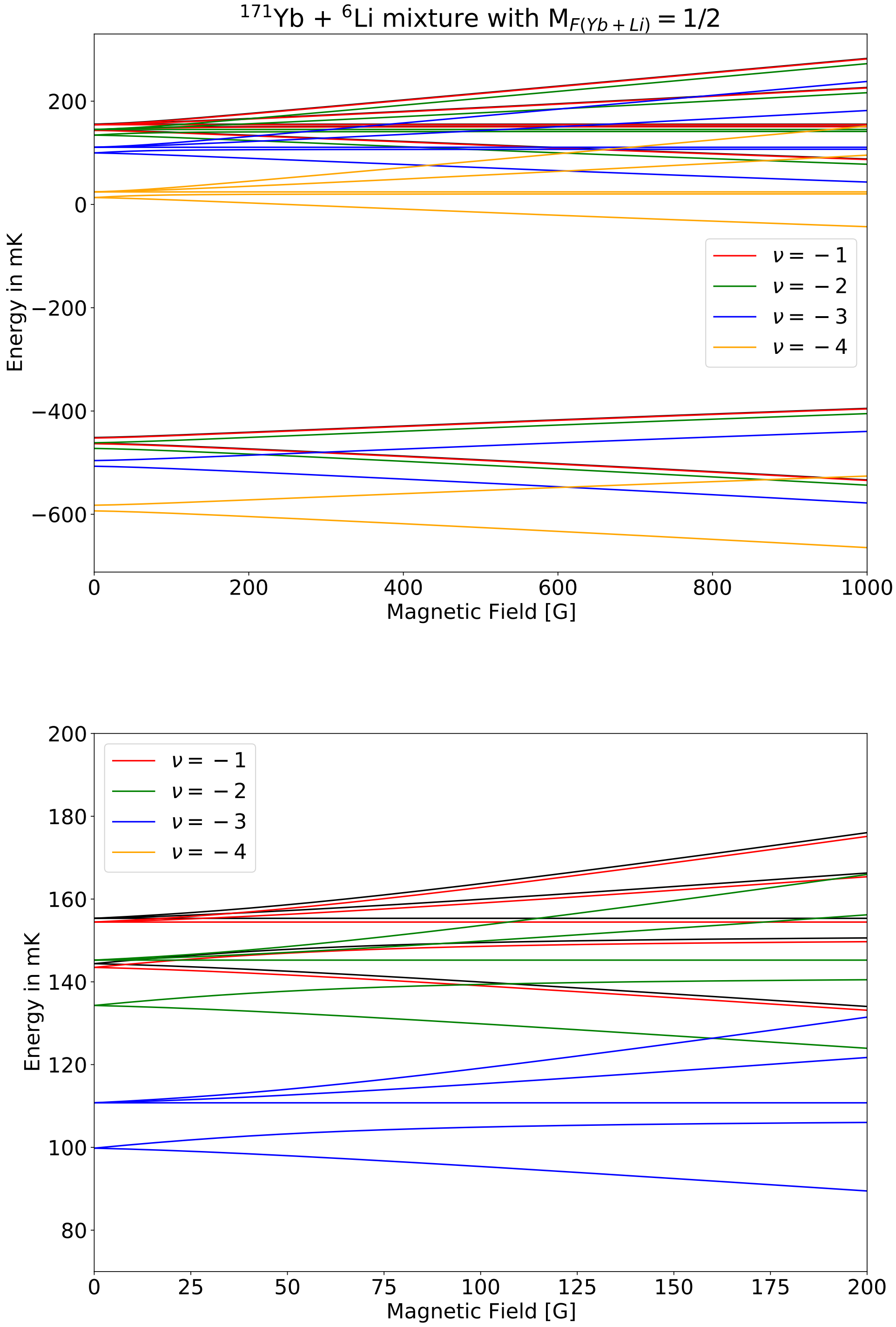

Figure 46: Hyperfine states of the Ytterbium-Lithiumm mixture with $M_F = 1/2$ and four the least-bound states: full range and zoom.

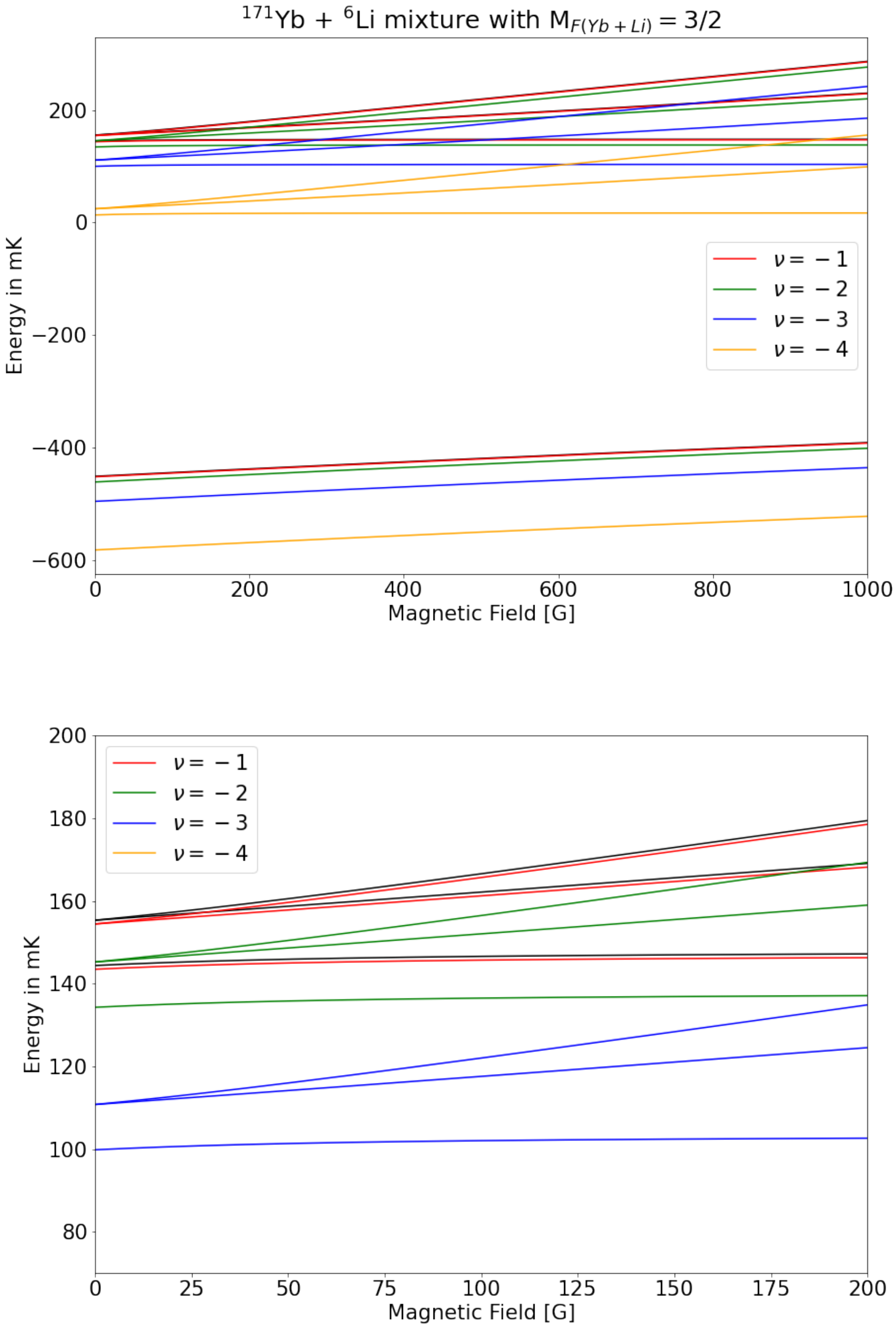

Figure 47: Hyperfine states of the Ytterbium-Lithium mixture with $M_F = 3/2$ and four the least-bound states: full range and zoom.

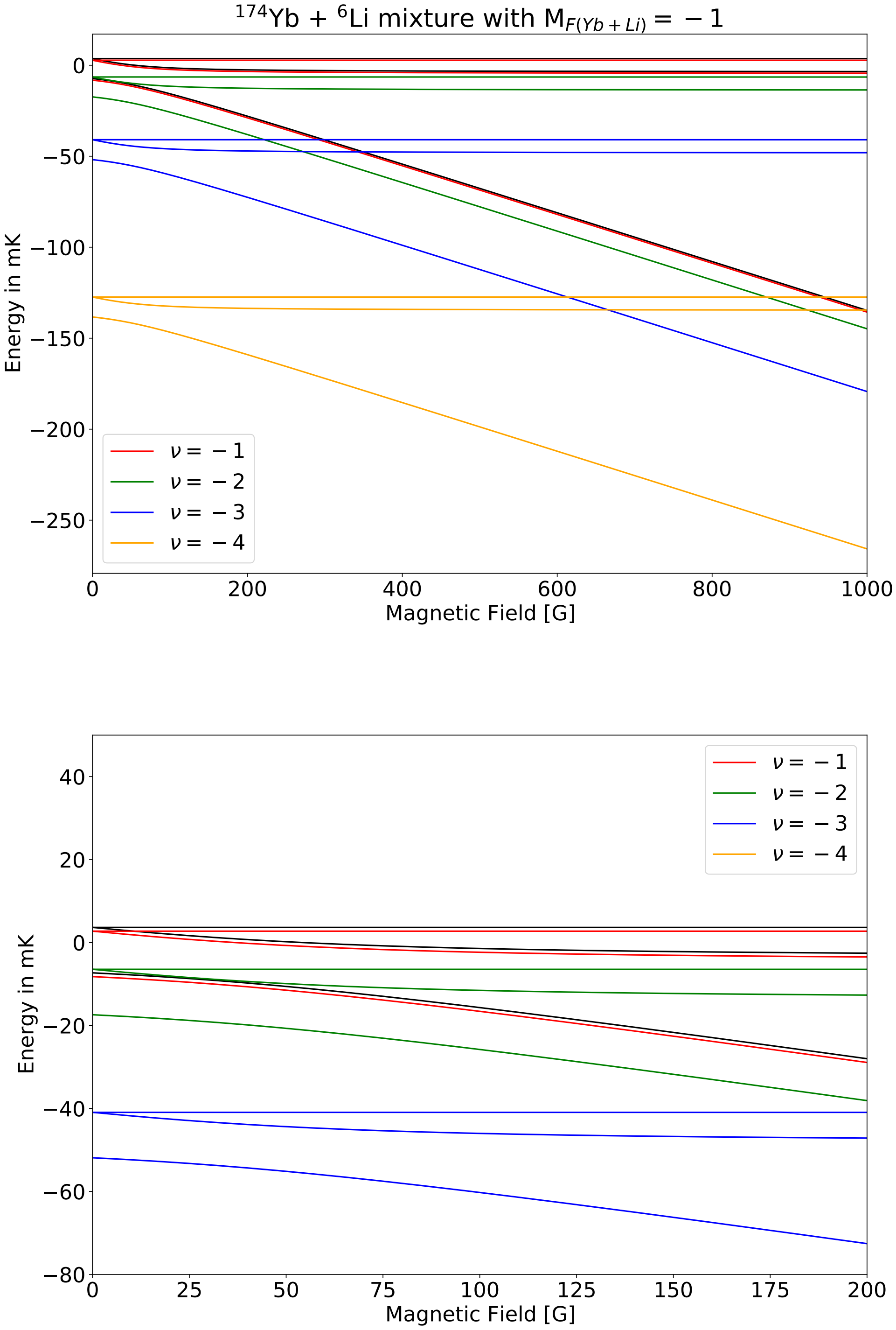

Figure 48: Hyperfine states of the Ytterbium-Lithium mixture with $M_F = -1$ and four the least-bound states: full range and zoom.

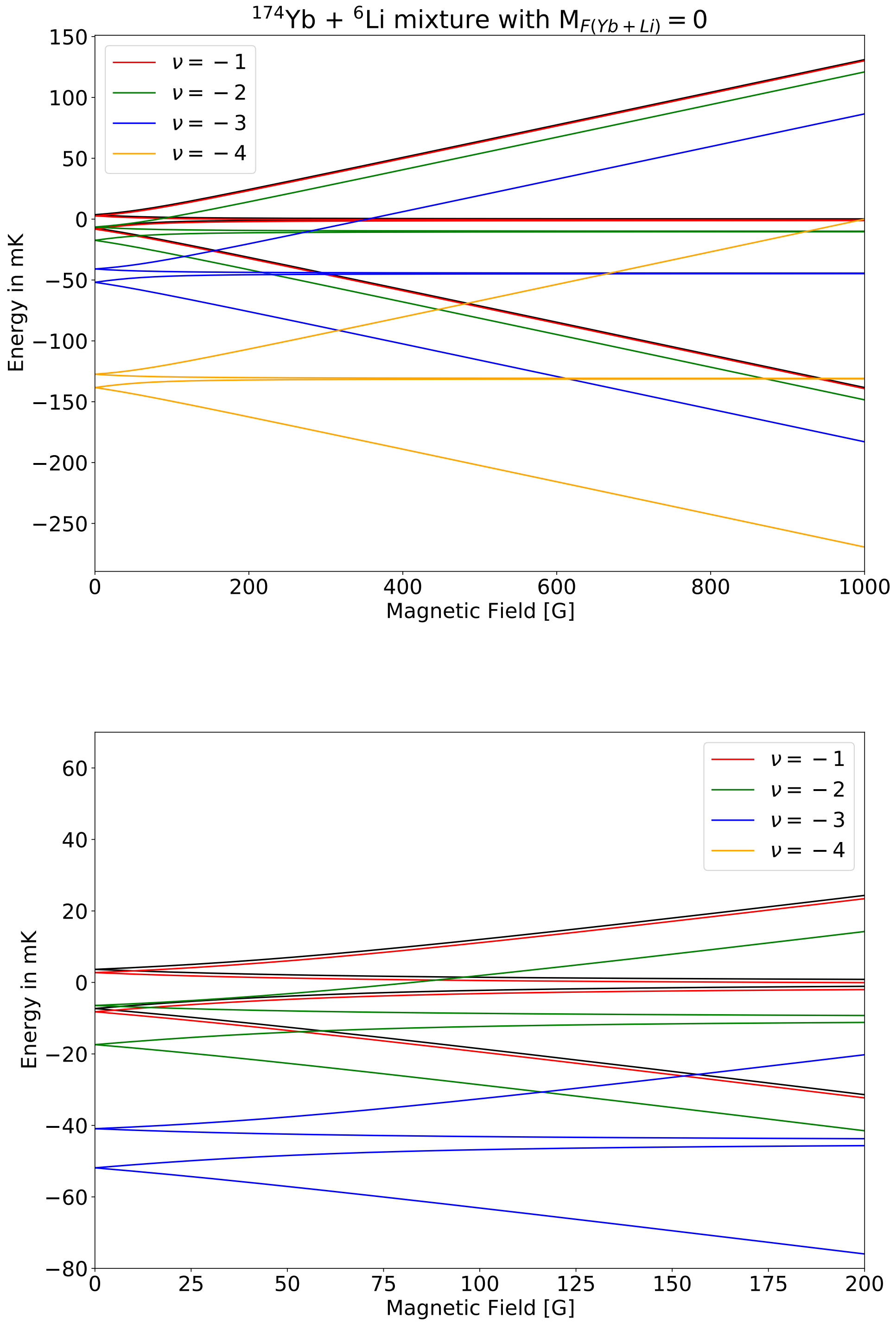

Figure 49: Hyperfine states of the Ytterbium-Lithium mixture with $M_F = 0$ and four the least-bound states: full range and zoom.

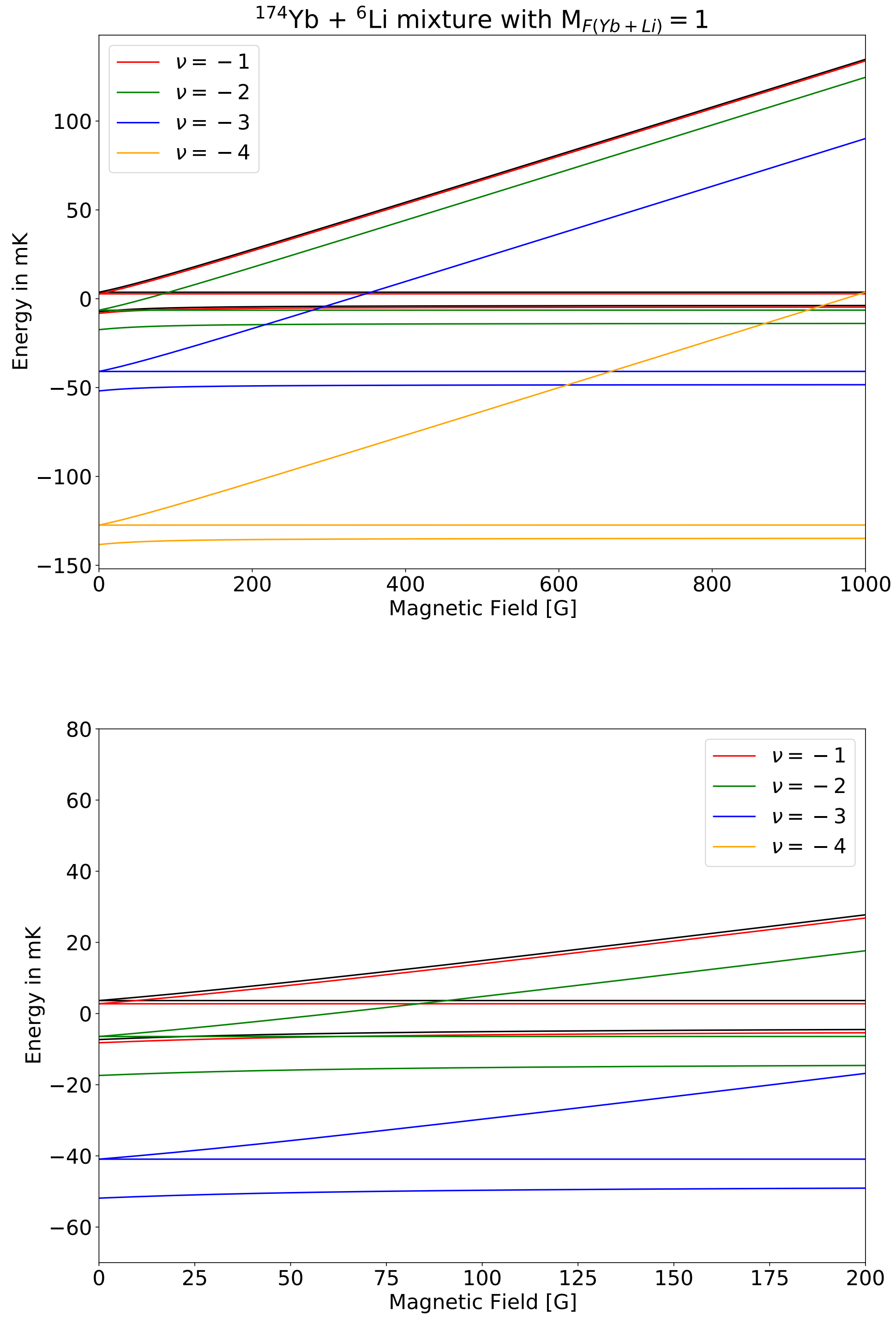

Figure 50: Hyperfine states of the Ytterbium-Lithium mixture with $M_F = 1$ and four the least-bound states: full range and zoom.

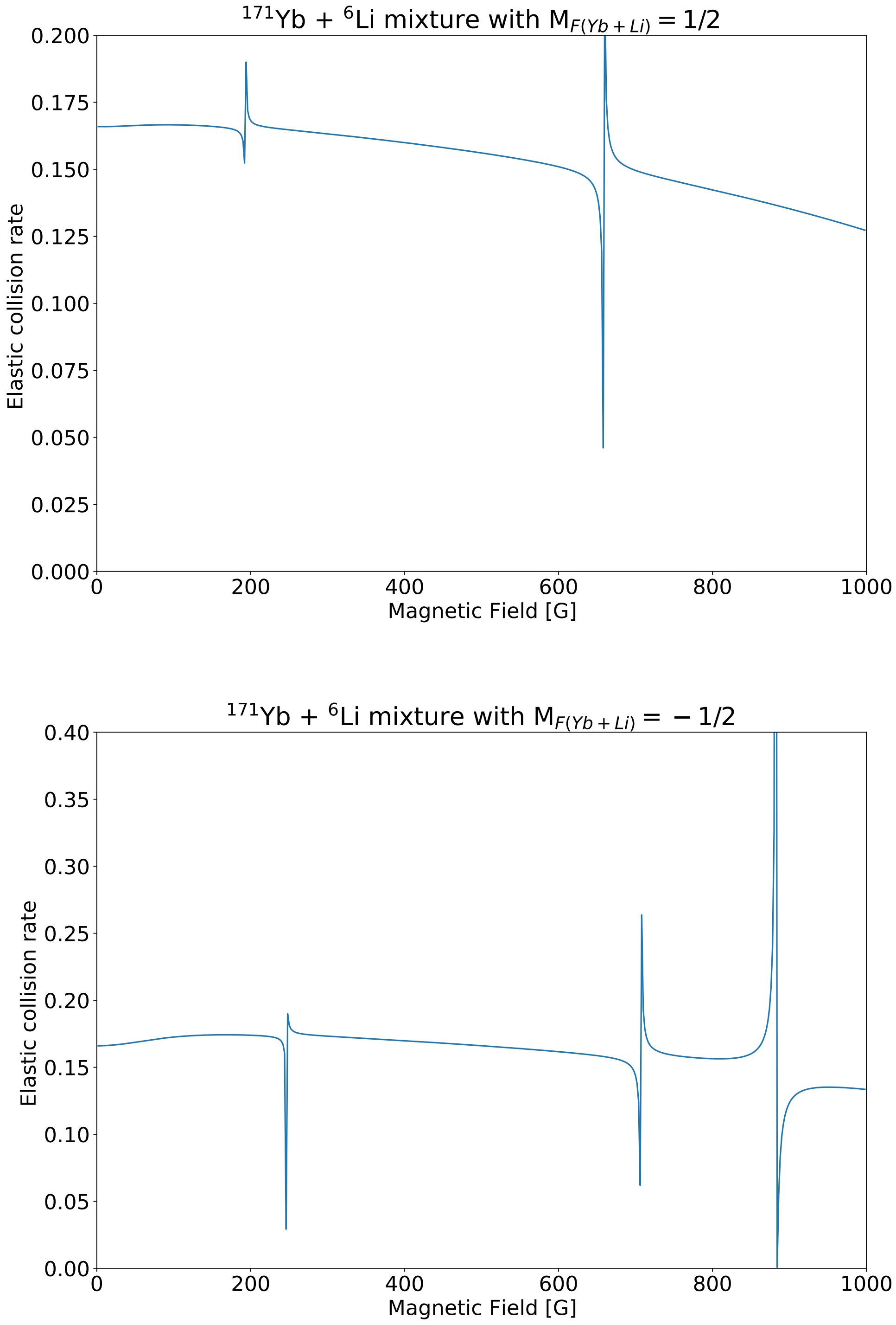

Figure 51: Feshbach resonances in Ytterbium-Lithium mixture for optimal set of scattering lengths for $M_F = 1/2$ and $M_F = -1/2$.

# 7

# OBSERVATION OF FESHBACH RESONANCES BETWEEN A SINGLE ION AND ULTRACOLD ATOMS

## 7.1 INTRODUCTION

Obtaining the quantum regime in ion-atom collisions in the experiment in Amsterdam with the ytterbium ion immersed in a cloud of lithium atoms was a great achievement. As in the case of neutral systems of cold atoms in the 1990s, when it opened a new field of research, now it also brings further perspectives. Hence, the most natural and desirable step was to show the possibility of observing Fesh-

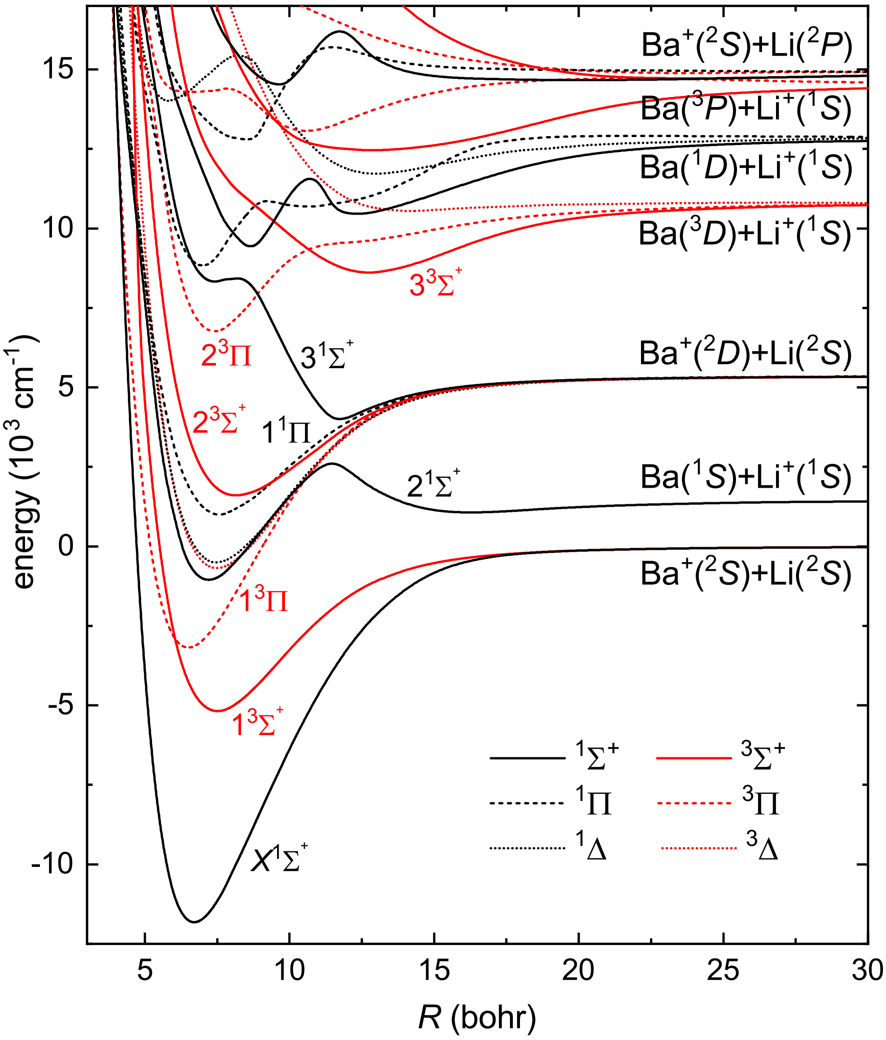

Figure 52: Nonrelativistic potential energy for $(\mathrm{LiBa})^+$.

bach resonances in the ion-atom system. In the past, the Feshbach resonance technique was an essential tool for controlling the neutral interaction of atoms, so also now it is one of the key tools for hybrid systems. In the experimental field, several leading research groups were interested in observing resonances, including: Amsterdam, Freiburg, Florence. Finally, the group from Freiburg working with a barium ion immersed in a cloud of lithium atoms, supported by our theoretical calculations, was the first. The mixture of barium and lithium was, next to ytterbium, indicated as one of the most promising in the context of cooling to low temperatures and the observation of resonances. This was mainly due to the large ion-atom mass ratio. In the calculations, we use potentials in the singlet and triplet states, which are the molecular ground state for this mixture (Fig.52). Unfortunately, due to the intersection of these states with excited states and the large spin-orbit coupling, the real physical mechanism of resonances turned out to be more complex than originally expected. The role of spin-orbit coupling in this system is still under investigation.

## 7.2 HYPERFINE STRUCTURE OF THE BA$^+$/LI MIXTURE

As in the case of the Lithium-Ytterbium system, the starting point is to investigate the structure of hyperfine levels. In the basis of electron and nuclear spin states we diagonalize the Hamiltonian describing the Zeeman effect and hyperfine coupling (eq.66). First, we present the results for Barium-138 (Fig.53) and Barium-137 (Fig.54), in the case of the first, the situation is extremely simple due to the lack of a nuclear spin. The results for lithium are not repeated as they were already shown in the previous section (Figs.27-28). In the next step, the hyperfine states for all the considered isotopes of the mixture of barium and lithium were presented. Starting with the ion-atom mixture used in the experiment, i.e. Barium-138 with Lithium-6 (Figs.55-57). Before the experiment was performed, however, we also considered other potential possibilities for ion-atom mixtures of these isotopes. Hence, for the purpose of having complete documentation of the tested systems and looking towards future calculations, the hyperfine states for the remaining mixtures of Barium-137, Lithium-6 and Lithium-7 isotopes are presented further in the section. Namely, Figs.58-63 show a mixture of Barium-137 and Lithium-6 for different total spin projections. Similarly Figs.64-67 correspond to barium-138 and lithium-7 mixture. Finally, Fig.68-74 describe a mixture of Barium-137 and Lithium-7 isotopes. The above-mentioned hyperfine states were first used to estimate the position of resonances, when their mechanism was not known yet, and the scattering lengths remained unknown.

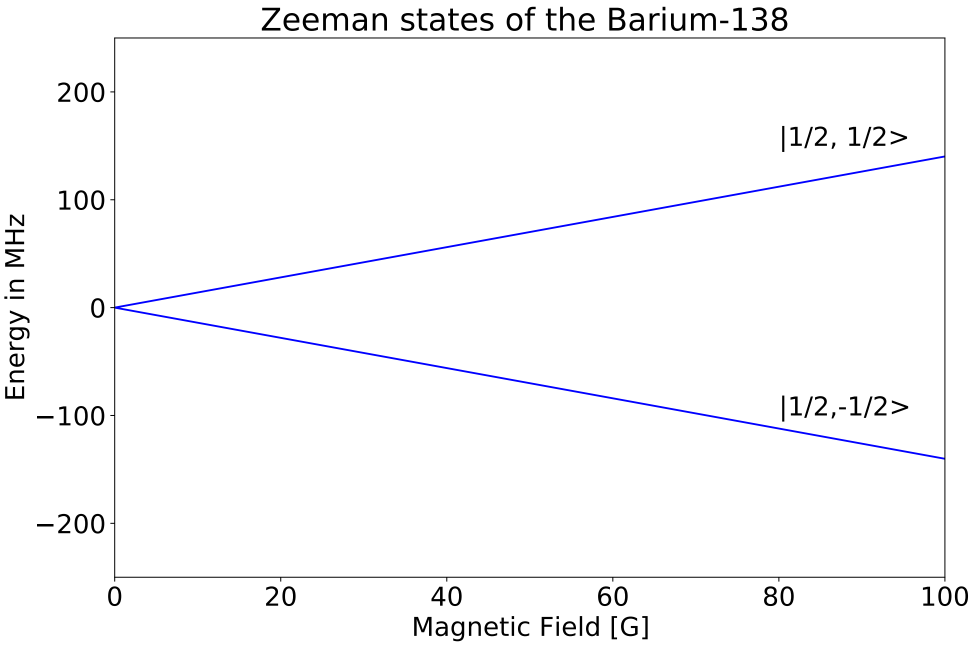

Figure 53: Zeeman states of the Barium-138 with labels $|f, m_f\rangle$.

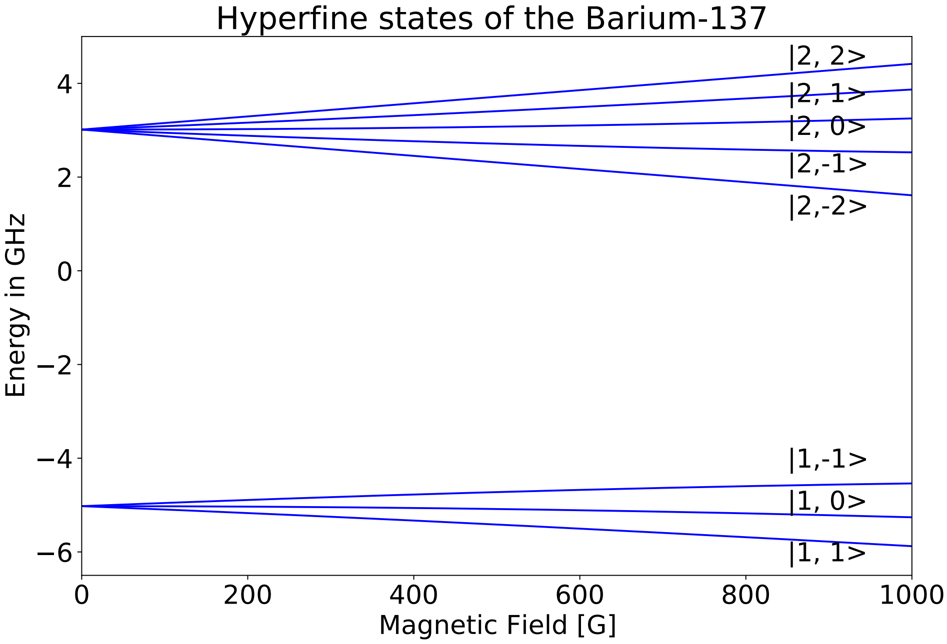

Figure 54: Hyperfine states of the Barium-137 with labels $|f, m_f\rangle$.

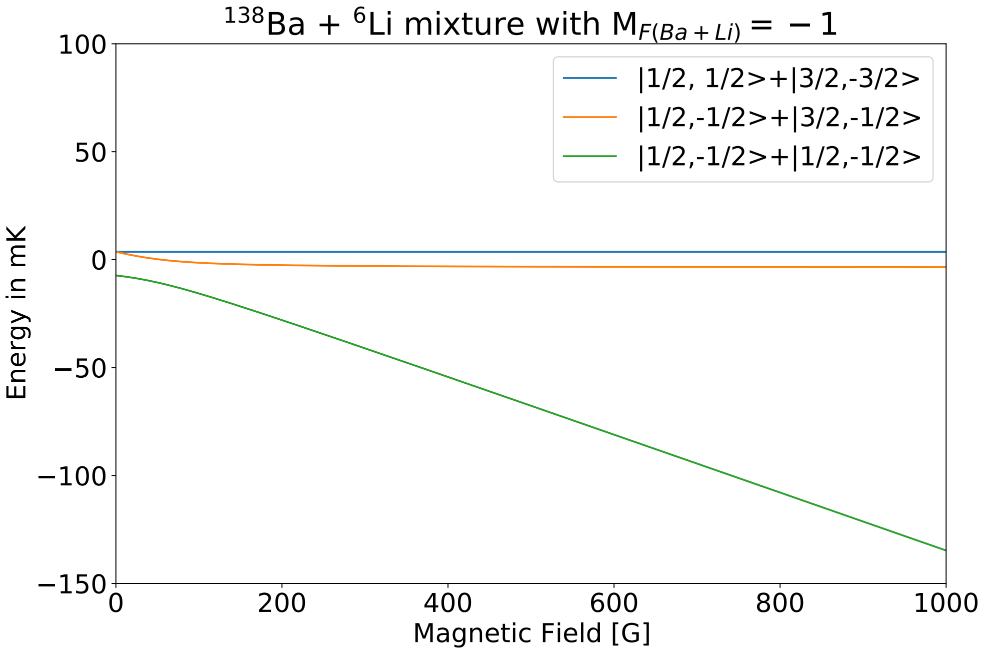

Figure 55: Hyperfine states of the Barium-Lithium mixture with total $M_F = -1$.

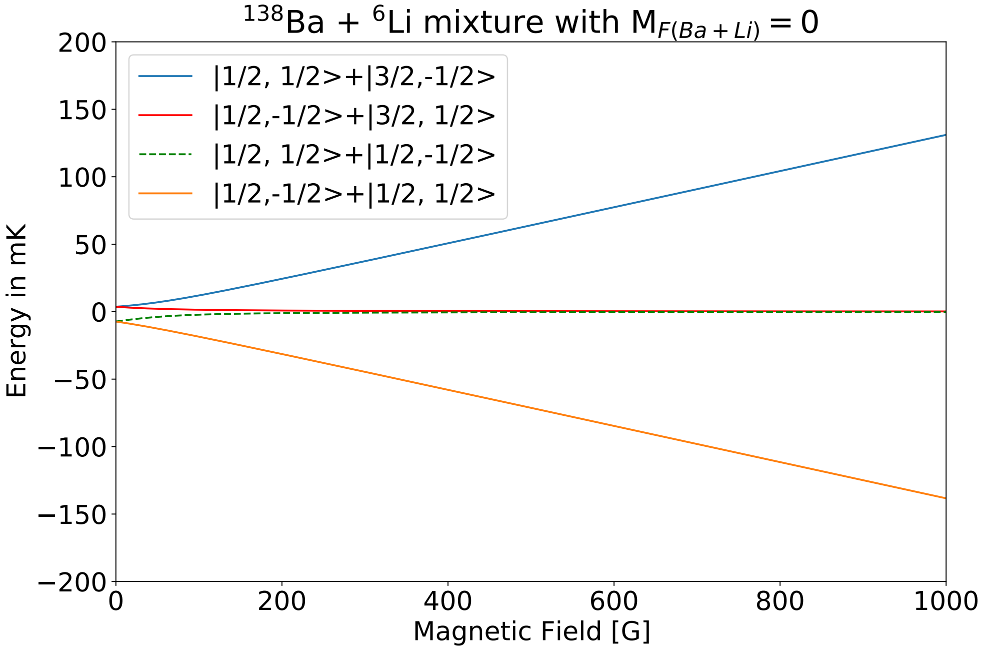

Figure 56: Hyperfine states of the Barium-Lithium mixture with total $M_F = 0$.

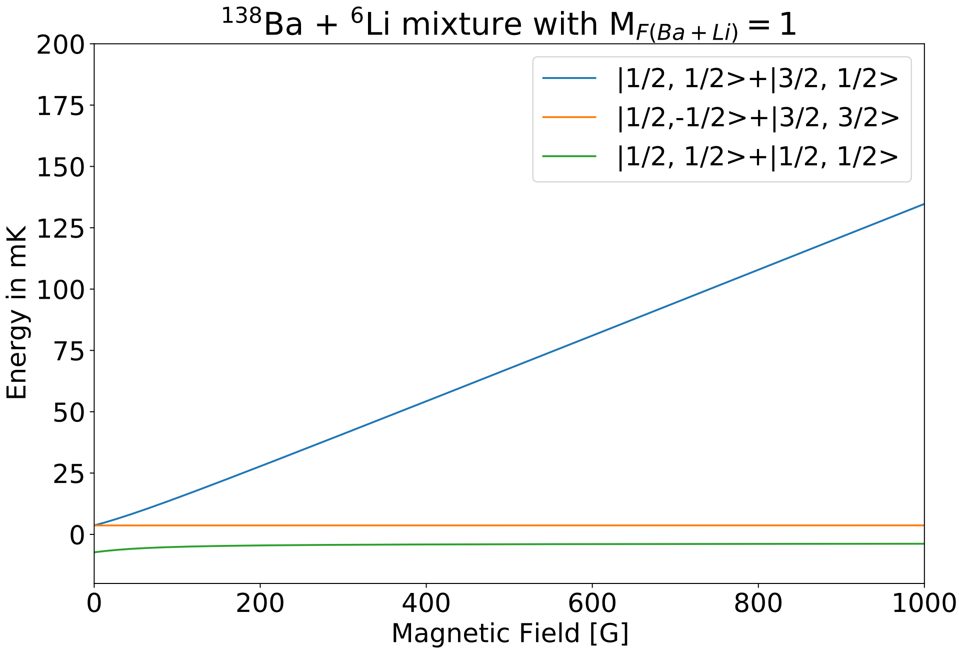

Figure 57: Hyperfine states of the Barium-Lithium mixture with total $M_F = 1$.

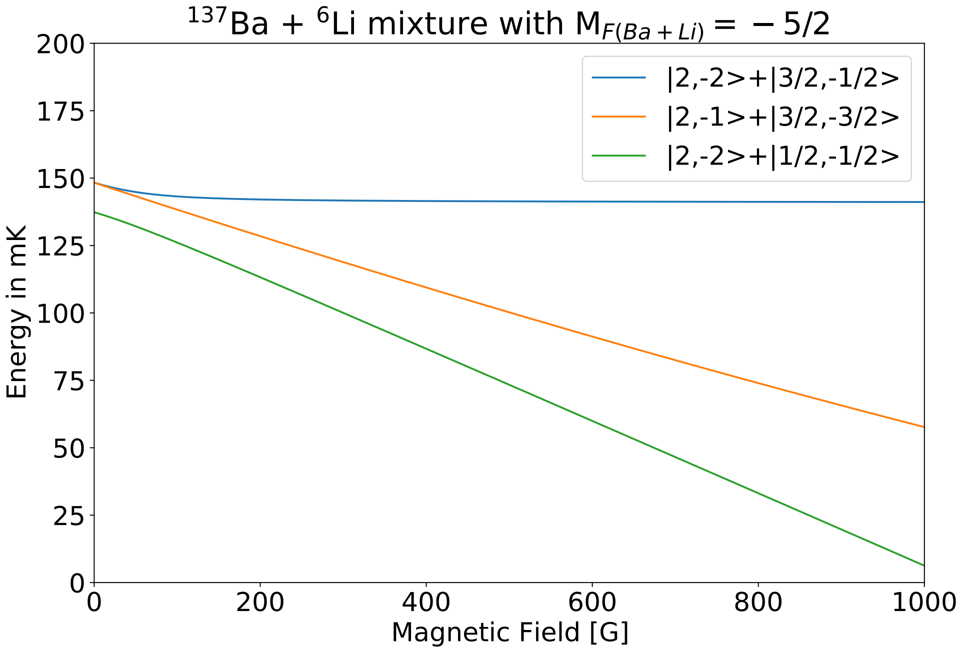

Figure 58: Hyperfine states of the Barium-Lithium mixture with total $M_F = -5/2$.

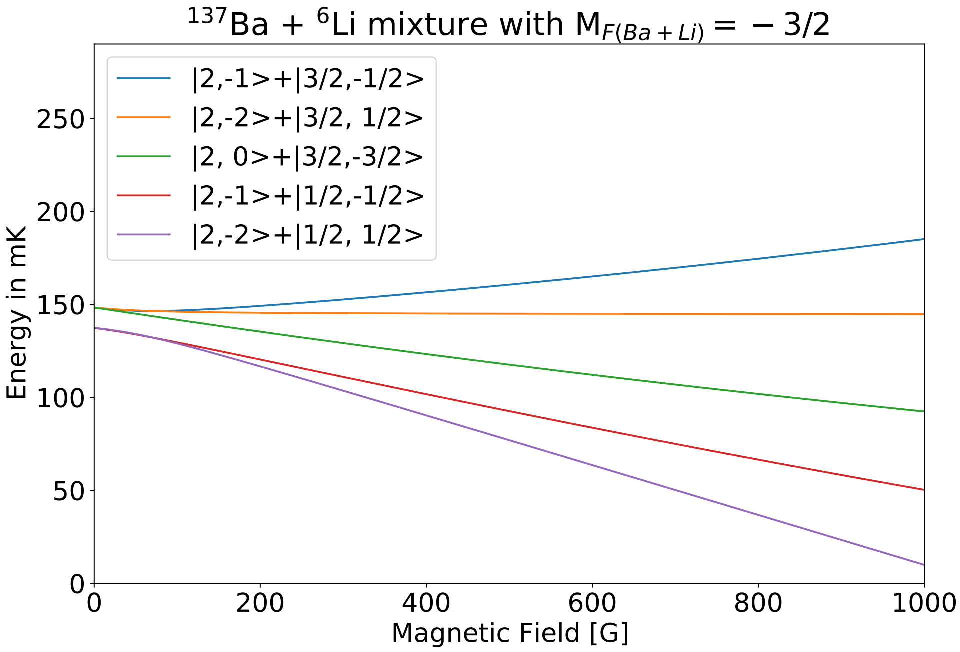

Figure 59: Hyperfine states of the Barium-Lithium mixture with total $M_F = -3/2$.

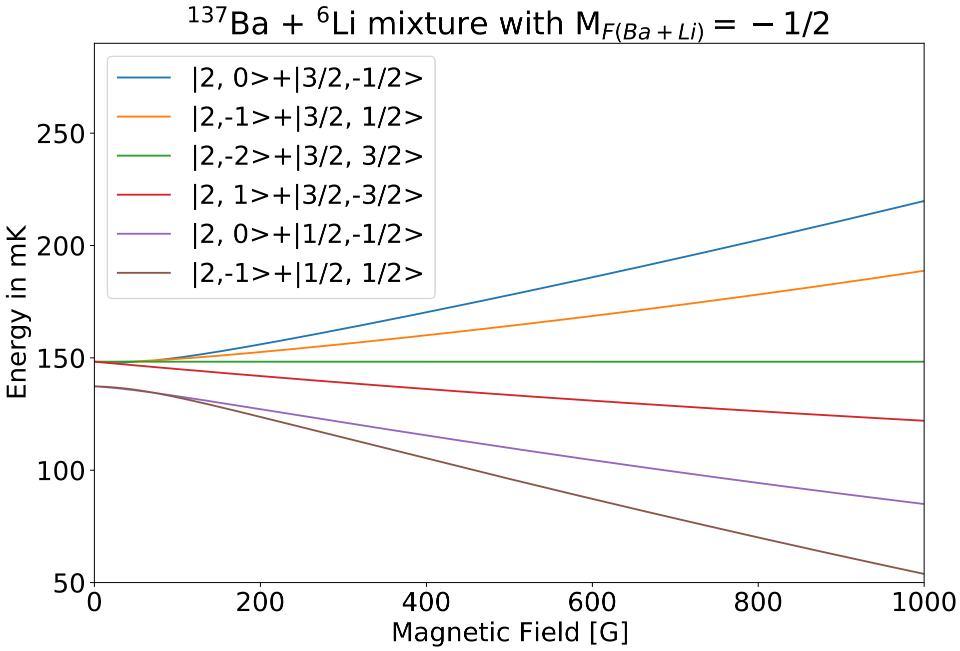

Figure 60: Hyperfine states of the Barium-Lithium mixture with total $M_F = -1/2$.

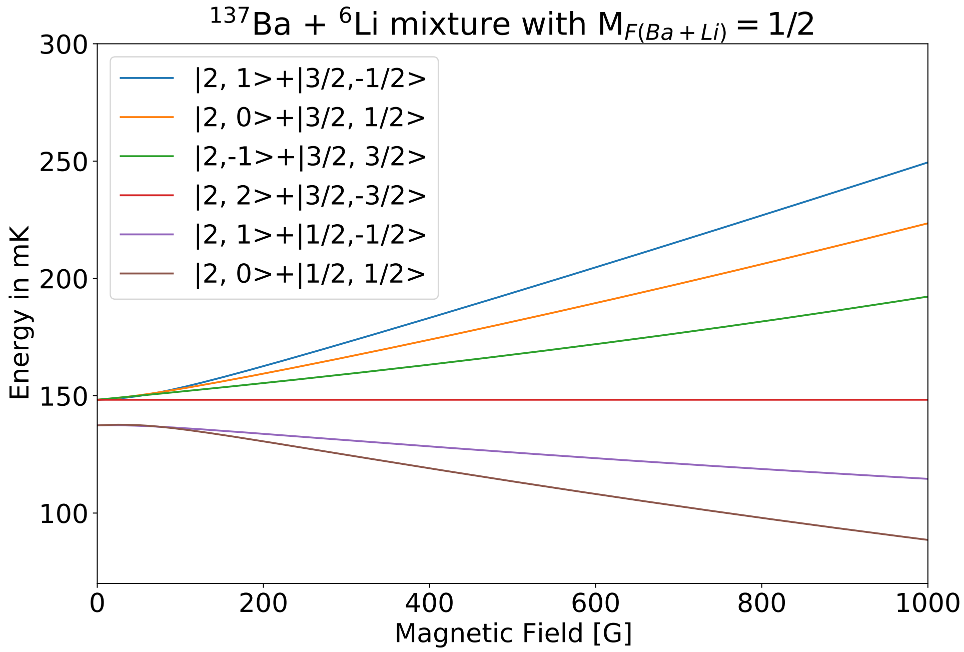

Figure 61: Hyperfine states of the Barium-Lithium mixture with total $M_F = 1/2$.

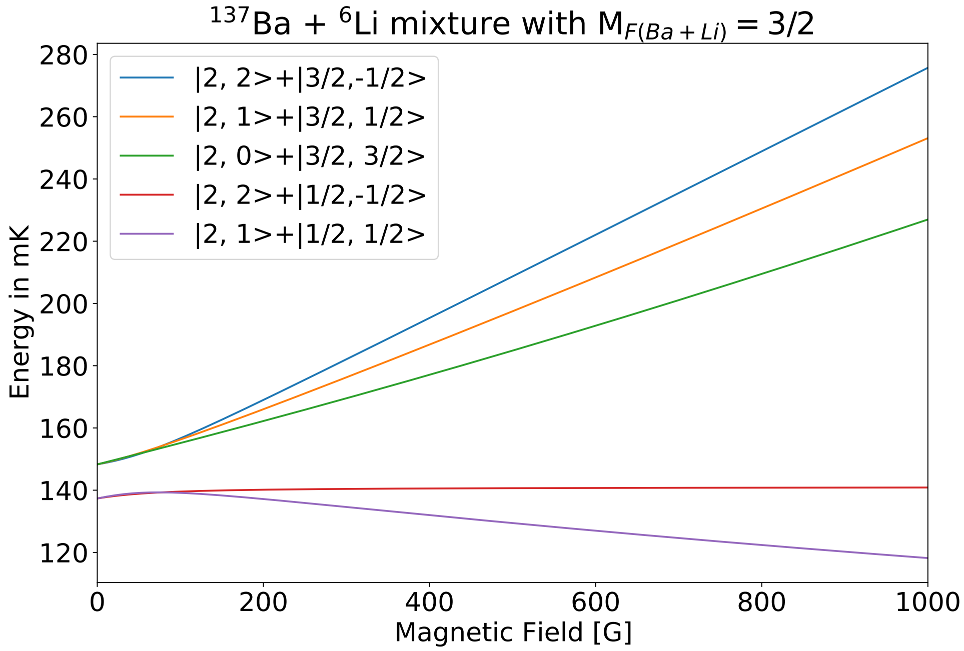

Figure 62: Hyperfine states of the Barium-Lithium mixture with total $M_F = 3/2$.

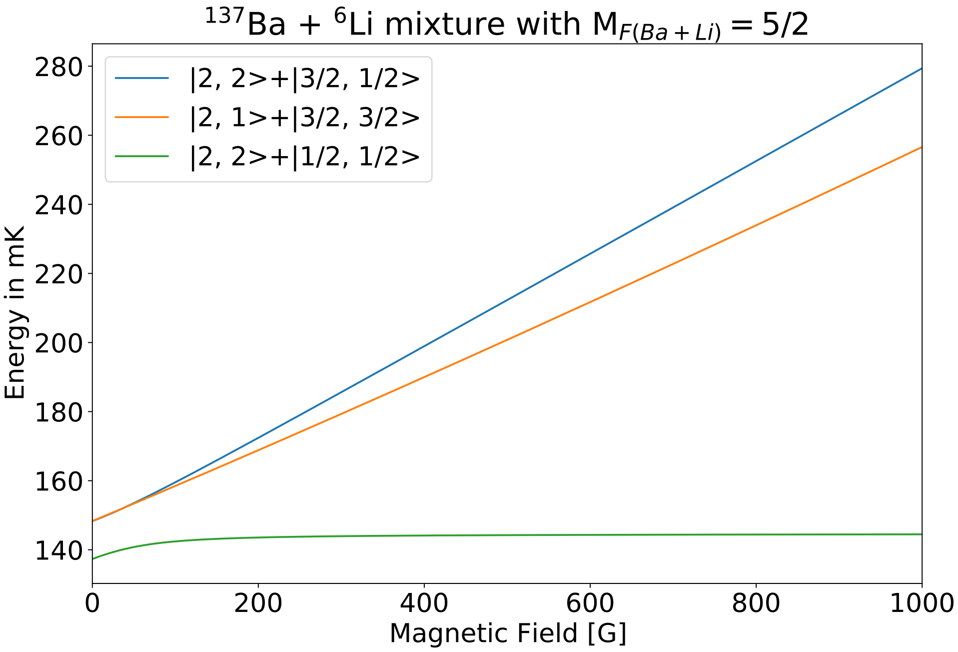

Figure 63: Hyperfine states of the Barium-Lithium mixture with total $M_F = 5/2$.

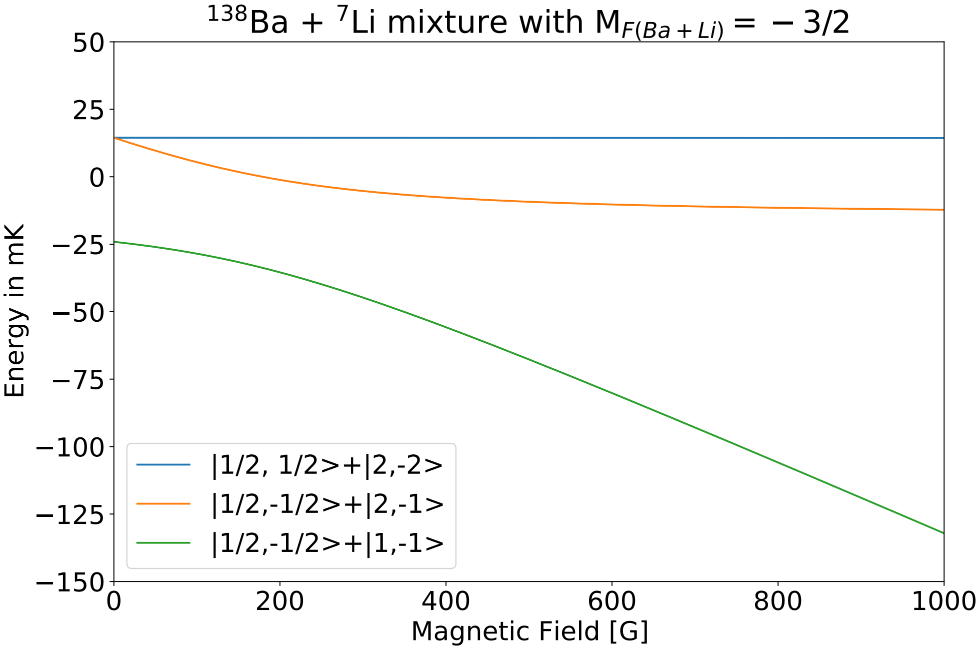

Figure 64: Hyperfine states of the Barium-Lithium mixture with total $M_F = -3/2$.

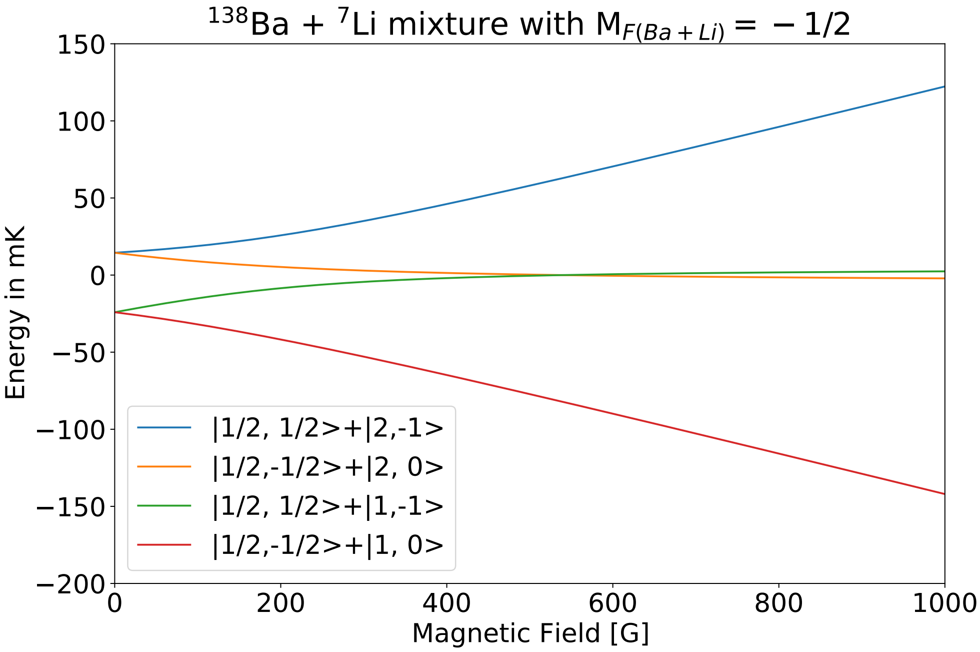

Figure 65: Hyperfine states of the Barium-Lithium mixture with total $M_F = -1/2$.

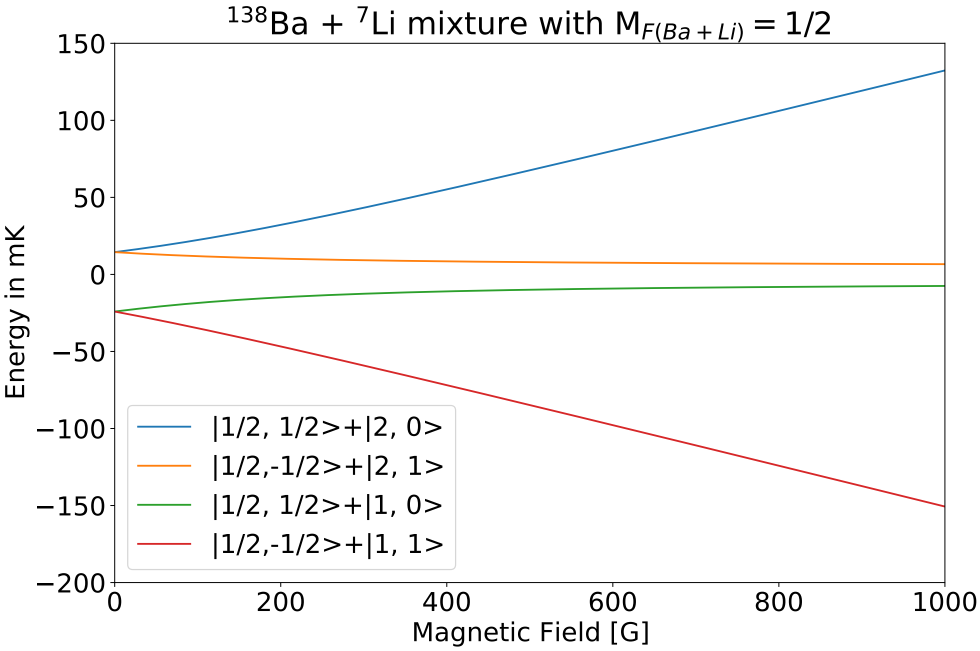

Figure 66: Hyperfine states of the Barium-Lithium mixture with total $M_F = 1/2$.

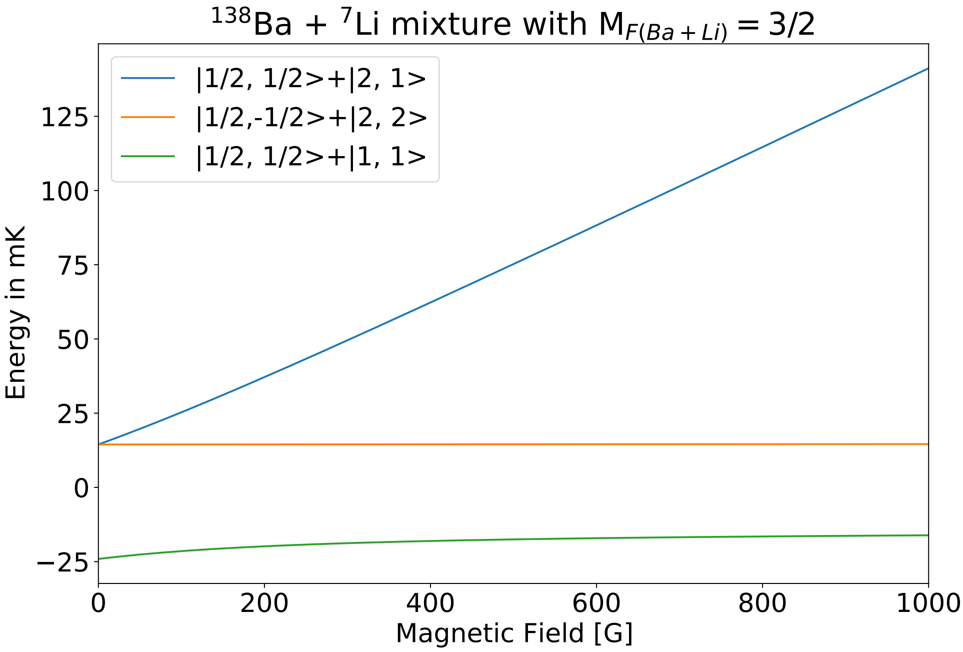

Figure 67: Hyperfine states of the Barium-Lithium mixture with total $M_F = 3/2$.

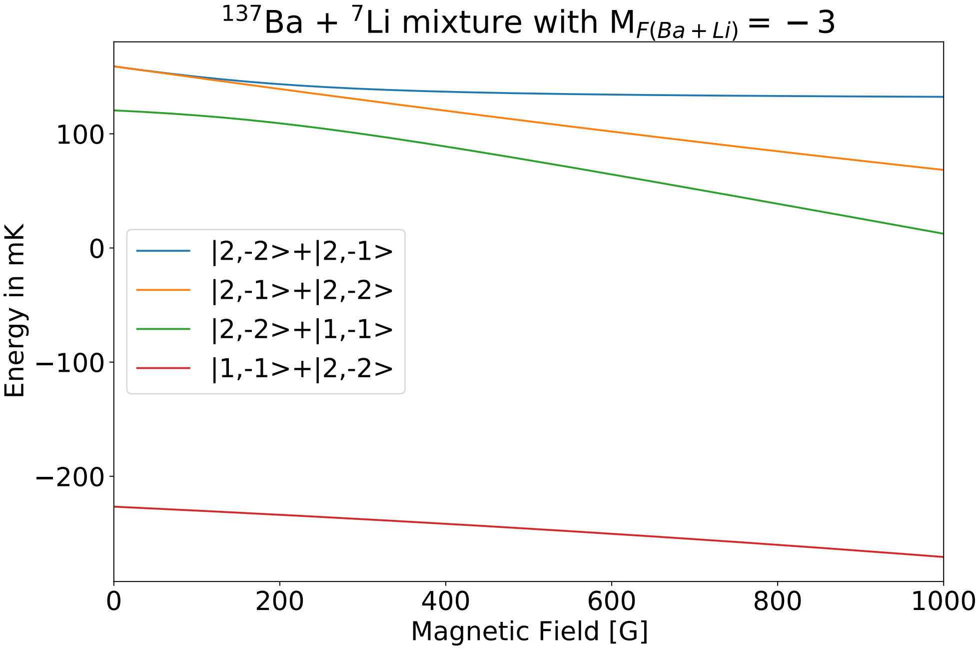

Figure 68: Hyperfine states of the Barium-Lithium mixture with total $M_F = -3$.

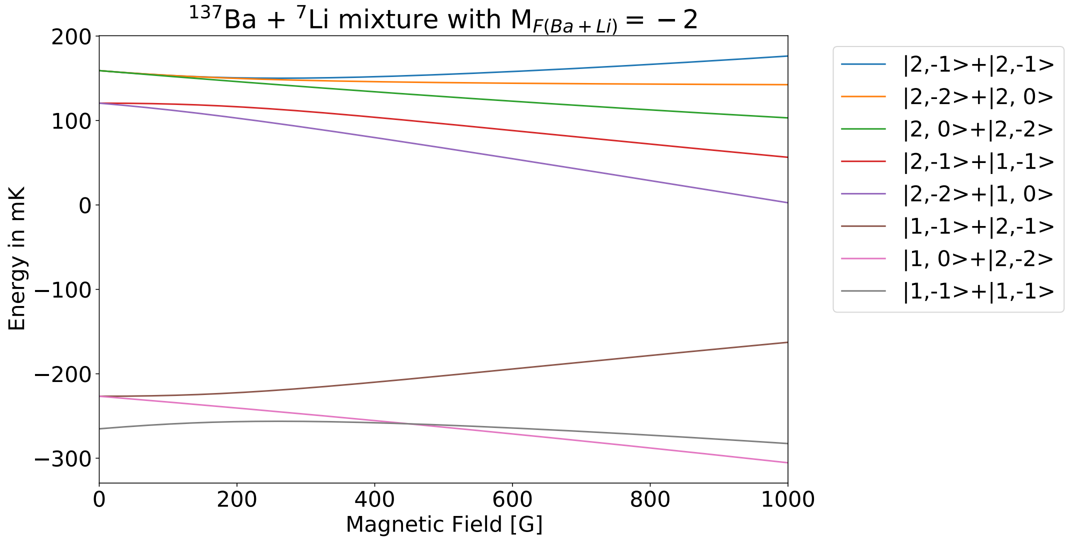

Figure 69: Hyperfine states of the Barium-Lithium mixture with total $M_F = -2$.

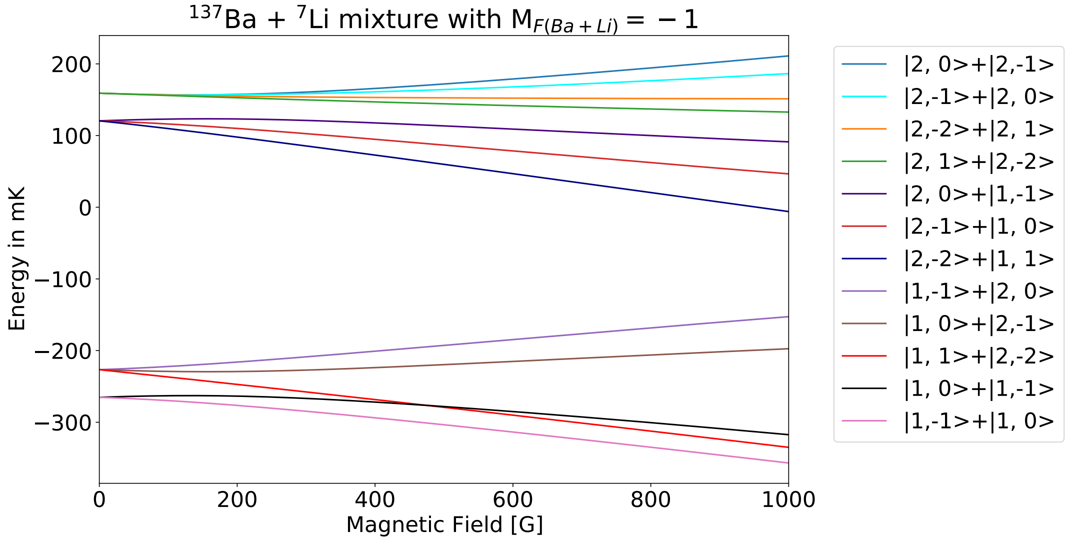

Figure 70: Hyperfine states of the Barium-Lithium mixture with total $M_F = -1$.

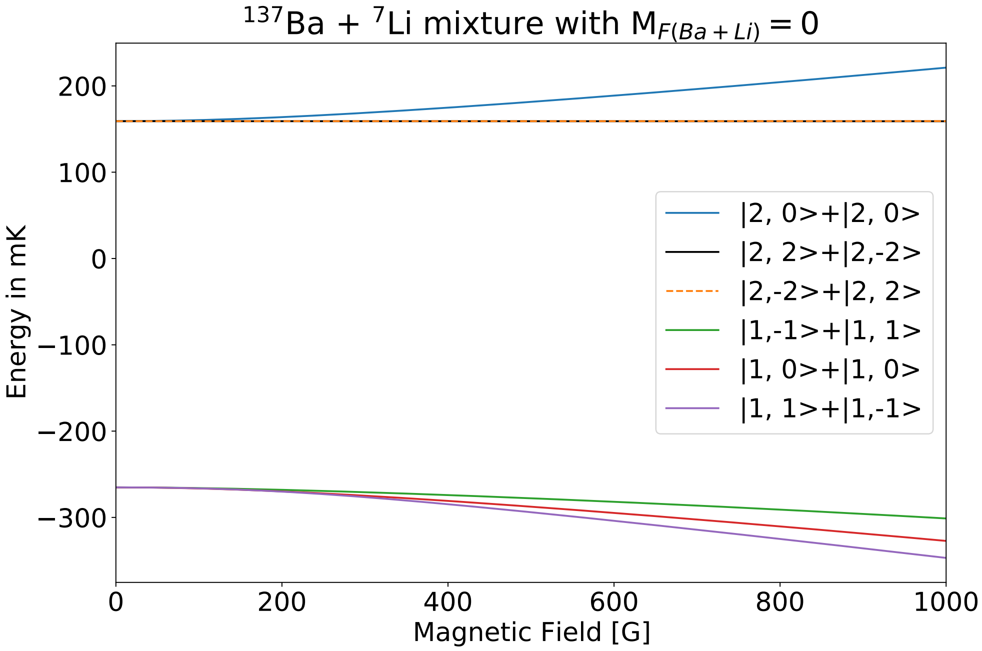

Figure 71: Hyperfine states of the Barium-Lithium mixture with total $M_F = 0$.

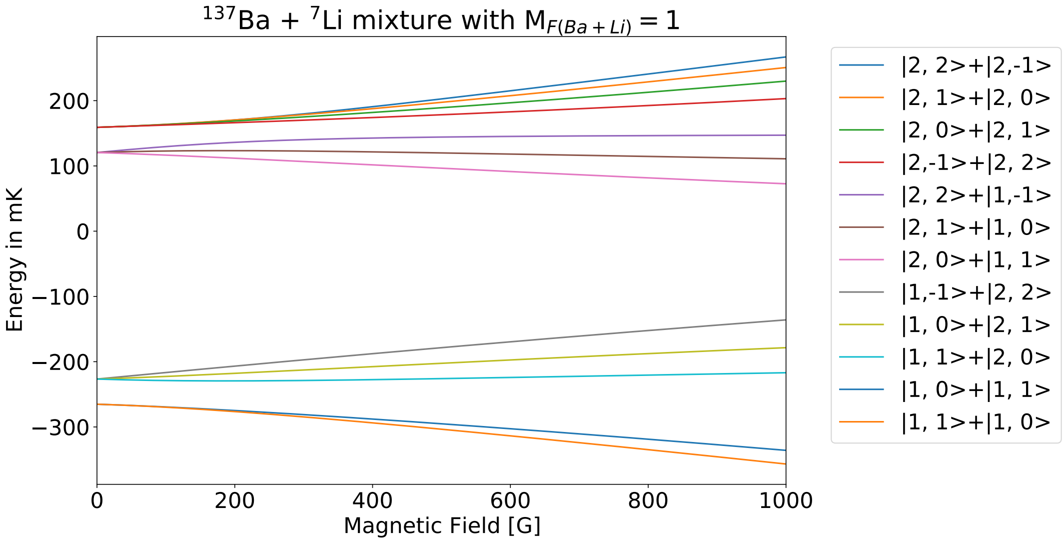

Figure 72: Hyperfine states of the Barium-Lithium mixture with total $M_F = 1$.

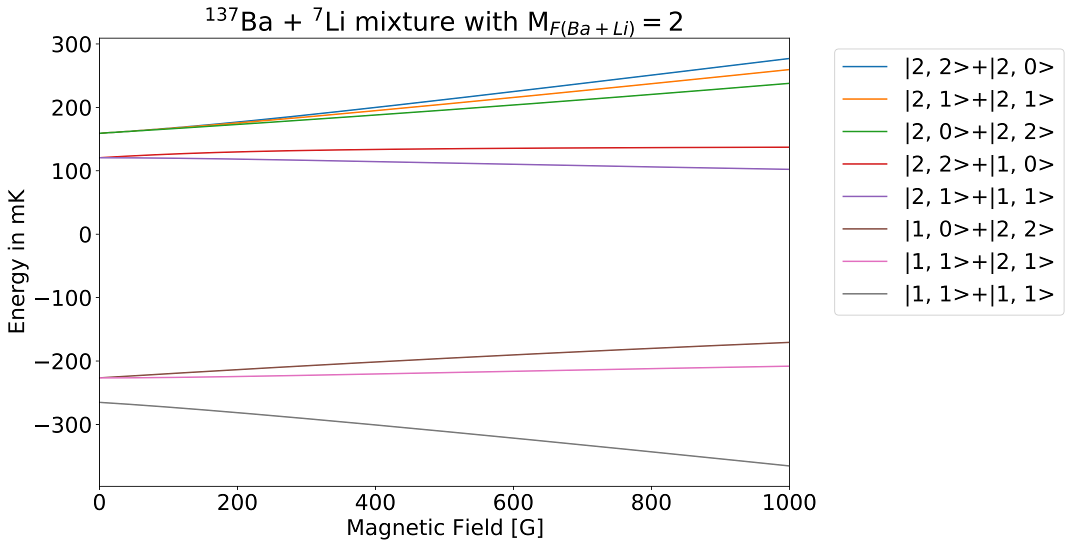

Figure 73: Hyperfine states of the Barium-Lithium mixture with total $M_F = 2$.

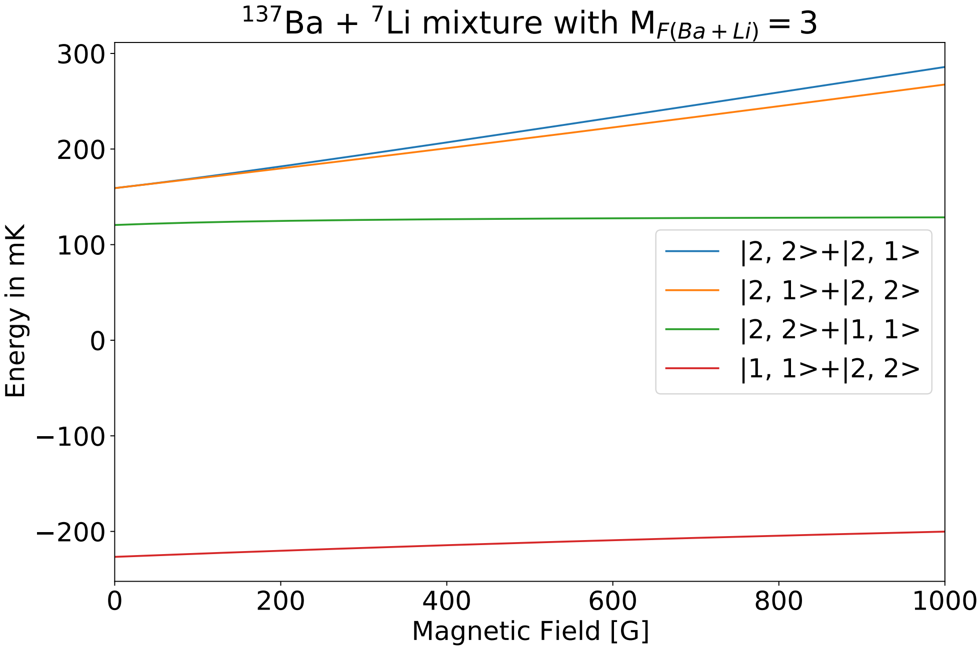

Figure 74: Hyperfine states of the Barium-Lithium mixture with total $M_F = 3$.

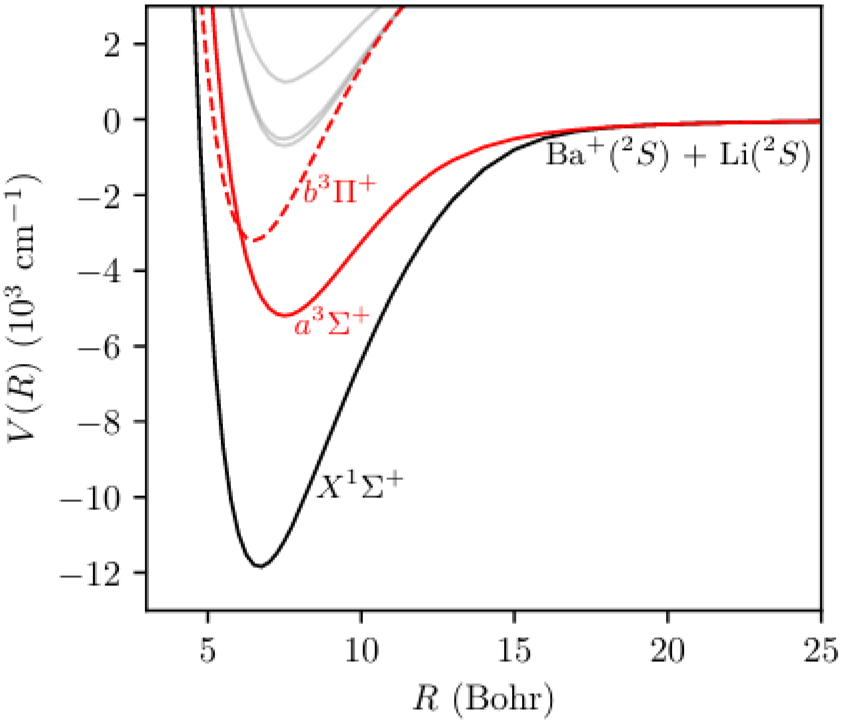

Figure 75: Nonrelativistic potential energy curves for the $(\mathrm{BaLi})^+$ molecular ion and spin-orbit coupling between the $a^3\Sigma^+$ and $b^3\Pi^+$ electronic states.

## 7.3 SPIN-ORBIT COUPLING

In a typical situation in alkaline gases, we observe collisions in which $M_F$ is conserved, thus we deal with Feshbach resonances between states with the same $M_F$. However, anisotropic interactions like dipolar spin-spin or second order spin-orbit coupling can mix internal spins with rotational motion. In this case, only the total projection $M_F + m_l$ is conserved. This mechanism significantly increases the number of resonances, but in the case of alkali atoms, this type of resonance is usually very narrow. The second order spin-orbit coupling for the $\mathrm{Ba}^+/\mathrm{Li}$ system is predicted to be very large, however its strength is not obvious to estimate because the positions of the molecular levels (related to scattering lengths) are unknown. The crossing of the $a^3\Sigma^+$ and $b^3\Pi$ molecular levels is expected below the collision energy threshold (Fig.75), for a distance of about $6a_0$, this is the mechanism responsible for the large spin-orbit coupling. The spin-orbit coupling coefficient in the second order can be calculated from the perturbation theory with the non-relativistic electronic states and matrix elements of the spin-orbit coupling Hamiltonian, where: $\langle a^3\Sigma^+ | H_{SO} | (n)^3\Pi \rangle$ is the matrix element of the spin-orbit coupling between the $a^3\Sigma^+$ and $(n)^3\Pi$ electronic states. It is well approximated by the first term

$$\lambda_{SO}(R) = \sum_{n} \frac{2}{3} \frac{|\langle a^3\Sigma^+|\, H_{SO}\, |(n)^3\Pi\rangle\,|^2}{V_{(n)^3\Pi}(R) - V_{a^3\Sigma^+}(R)} \approx \frac{2}{3} \frac{|\langle a^3\Sigma^+|\, H_{SO}\, |b^3\Pi\rangle\,|^2}{V_{b^3\Pi}(R) - V_{a^3\Sigma^+}(R)}. \tag{73}$$

This term decays exponentially with R for large distances, hence the following relationship can be obtained, the fit to the ab initio point at large distances:

$$\lambda_{SO}(R) = A \exp(-B(R - R_0)). \tag{74}$$

Finally, the effective dipolar-like spin-spin interaction resulting from the magnetic dipolar spin-spin and second-order spin-orbit couplings have form:

$$H_{ss} = \left(-\frac{\alpha^2}{R^3} + \lambda_{SO}(R)\right) \sqrt{6} \sum_{q=-2}^{2} (-1)^q C^2_{-q}(\phi, \theta) [\hat{s}_1 \otimes \hat{s}_2]^2_q, \tag{75}$$

where $C^2_q(\phi, \theta)$ is the reduced spherical harmonic defined as $C^k_q(\phi, \theta) = \sqrt{4\pi/(2k+1)}Y^k_q(\phi, \theta)$. and $[\hat{s}_1 \otimes \hat{s}_2]^{(2)}_q$ is the second-rank tensor formed from the spin operators of atom 1 and ion 2. The action of this operator on the states can be summarized as follows:

- $q = 0$ term of $\hat{H}_{ss}$ couples atomic and molecular states with the same $M_F = M_F'$ , $m_l = m_l'$ and different $l = l' \pm 2$. It also couples states with the same $M_F = M_F'$ and $l = l'$ for $l > 0$ and is then responsible for splittings of higher partial waves resonances in the first order of perturbation.

- $q = \pm 1$ term of $\hat{H}_{ss}$ couples atomic and molecular states having $M_F = M_F' \pm 1$ and $m_l = m_l' \mp 1$ and $l = l' \pm 2$ or $l = l' \pm 2$, $l'$ for $l > 0$.

- $q = \pm 2$ term of $\hat{H}_{ss}$ couples atomic and molecular states having $M_F = M_F' \pm 2$ and $m_l = m_l' \mp 2$ and and $l = l' \pm 2$ or $l = l' \pm 2$, $l'$ for $l > 1$.

The second order spin-orbit coupling is very large in the studied system. This not only makes $m_F$ changing resonances observable, but also splits higher partial wave resonances into multiple components. Perturbation theory can be employed to estimate energy splittings $\Delta E_{ml}$ of molecular levels:

$$\Delta E_{ml} \sim \langle l, m_l|\, C^2_0\, |l, m_l\rangle \, \langle \phi^l_{mol}| \lambda_{SO}(R) [\hat{s}_1 \otimes \hat{s}_2]^{(2)}_0 \, |\phi^l_{mol}\rangle , \tag{76}$$

which translate to splittings of resonance positions via difference of atomic and molecular magnetic susceptibilities $\delta\mu$:

$$\Delta B_{ml} = \frac{\Delta E_{ml}}{\delta\mu}. \tag{77}$$

## 7.4 INTERACTION POTENTIALS IN MOLSCAT

The Molscat program is a bit old-fashioned but very efficient software for quantum scattering calculations, including spin-orbit coupling. In order to use Molscat, it was necessary to modify the module responsible for loading the interaction potential. The original module interpolated the potential using the RKHS method. Unfortunately, with such a deep potential, wanting to additionally use scaling to set the selected scattering length, the method turned out to be unstable. Even the addition of higher terms in the method expansion turned out to be ineffective. The solution was to completely change this module to a different potential loading method. This method was to use the Morse – long-range potential-energy functions[141]. The singlet and triplet potentials were fitted to the formula below, and then implemented with the most optimal parameters as a module for the Molscat program

$$V_S(R) = D_e \left[1 - \frac{u_{LR}(R)}{u_{LR}(R_e)} \exp\left(-\phi(R) y_p(R)\right)\right]^2 - D_e, \tag{78}$$

where: $D_e$ and $R_e$ are the potential depth and equilibrium distance. The long-range part of the potential has following form:

$$u_{LR} = -\frac{C_4}{R^4} - \frac{C_6}{R^4}, \tag{79}$$

and other used functions:

$$y_p(R) = \frac{R^p - R_e^p}{R^p + R_e^p}, \tag{80}$$

$$\phi(R) = \varphi_\infty y_p(R) + (1 - y_p(R)) \sum_{i=0}^{4} \varphi_i y_q^i(R), \tag{81}$$

where: $\varphi_\infty = \ln\left(\frac{-2D_e}{u_{LR}(R_e)}\right)$. The interaction potentials were tested with different p, q parameters, the best fits are summarized in the Tab.2 below. In addition, we used the following coefficients: $C4 = 1.41125 \cdot 10^6$ and $C6 = 2.07908 \cdot 10^7$ in units that take into account that the measure of length is angstrom and the potential is expressed in inversed centimeters. After such an introduction of the potential to the calculations in the Molscat program, we achieved full compatibility of the results for the same scaling parameters with the earlier scattering calculations.

| List of the optimal parameters | | |
|---|---|---|
| parameters | singlet | triplet |
| p | 2 | 3 |
| q | 2 | 3 |
| $D_e[\mathrm{cm}^{-1}]$ | 11851.02546 | 5190.833438 |
| $R_e[\mathrm{Å}]$ | 3.54041 | 3.96856 |
| $\varphi_0$ | -2.69216 | -1.4696 |
| $\varphi_1$ | -1.39898 | -0.396147 |
| $\varphi_2$ | -3.72279 | -1.34978 |
| $\varphi_3$ | -2.87921 | -0.724098 |
| $\varphi_4$ | 7.52448 | 2.30637 |
| $\varphi_5$ | 15.4607 | 3.34419 |

Table 2: List of the optimal parameters of the Morse – long-range potential-energy functions in the Molscat

## 7.5 POSITION OF THE FESHBACH RESONANCES

### 7.5.1 *First estimation*

The first estimation of the position of the Feshbah resonances in the mixture consisting of barium ion and lithium atoms was made long before the experimental measurements began. As in the case of the ytterbium ion system (paragraph 6.3.3), we use the universal properties[140] of the ion-atom interaction and estimate the least-bound vibrational states. According to this approach, the resonance should be above the lower limit where the states intersect. The results were presented only for the mixture used in the experiment: Barium-138 with Lithium-6 (Figs.76-78). Of course, this type of estimation is not very precise, especially considering the mechanism of Feshbach resonances caused by the spin-orbit coupling.

### 7.5.2 *Multichannel quantum scattering calculations without Spin-Orbit coupling*

In order to reliably describe the processes taking place in the experiment, more accurate methods are needed. Our first approach was to use multichannel quantum scattering without spin-orbit coupling. At that time, we underestimated the importance of spin-orbit resonances. We thought that the experimental observations could be explained under the standard approach. We tested two spin configurations that were presented to us by the experimental group: $M_F = -1$ and $M_F = 0$, assuming lithium atoms in the state: $|f_{Li} = 1/2, m_{f,Li} = -1/2\rangle$. The

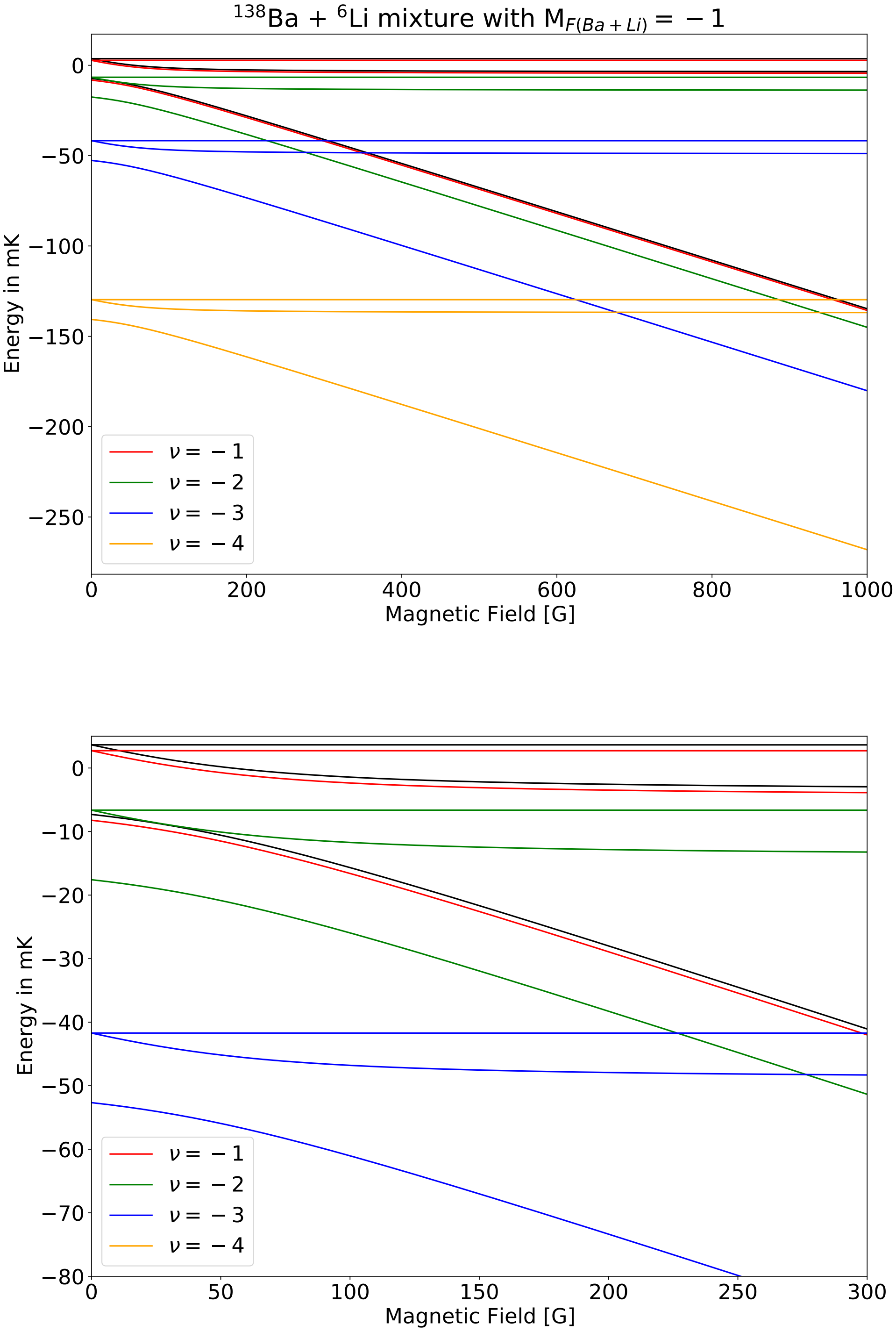

Figure 76: Hyperfine states of the Barium-Lithium mixture with $M_F = -1$ and four the least-bound states: full range and zoom.

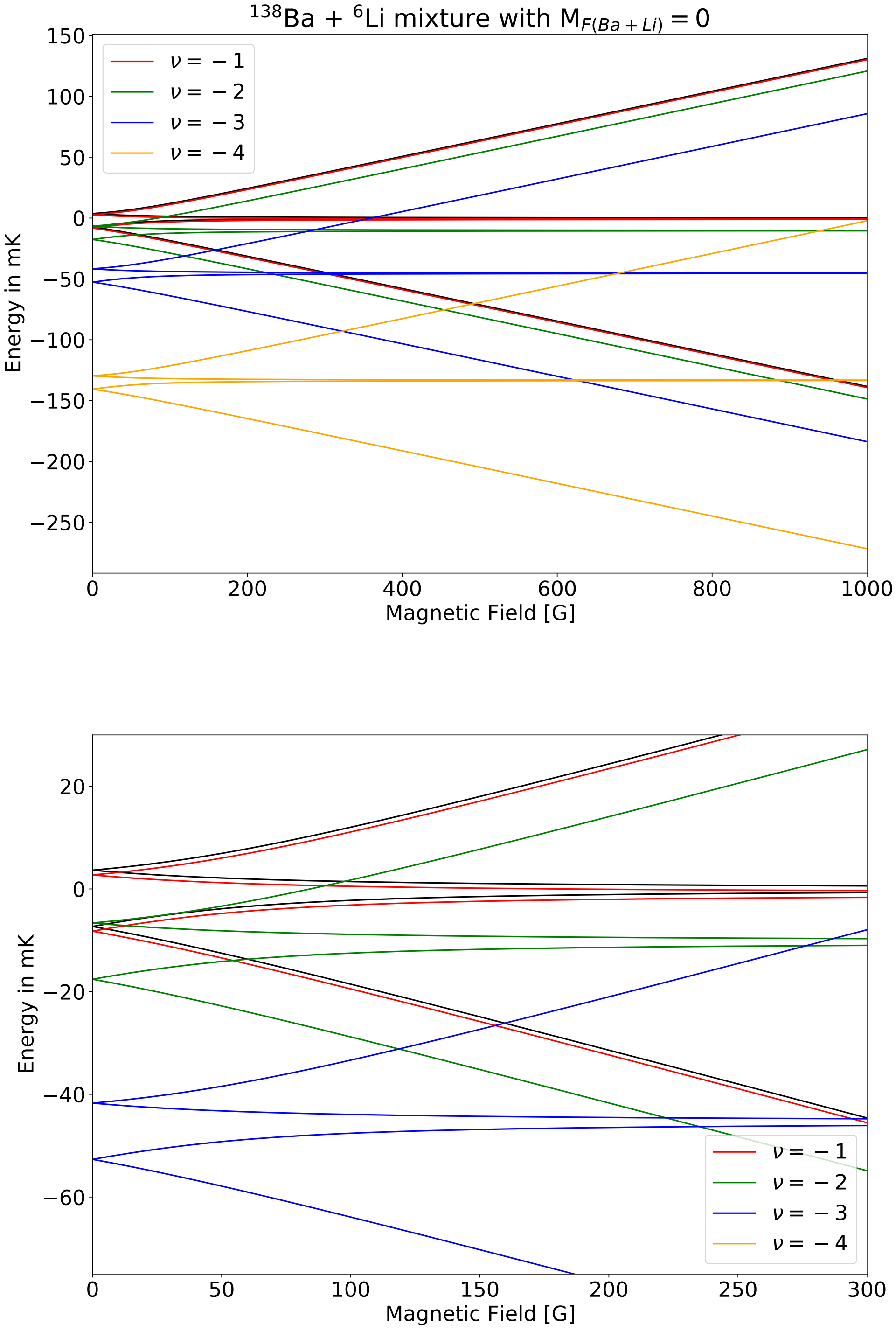

Figure 77: Hyperfine states of the Barium-Lithium mixture with $M_F = 0$ and four the least-bound states: full range and zoom.

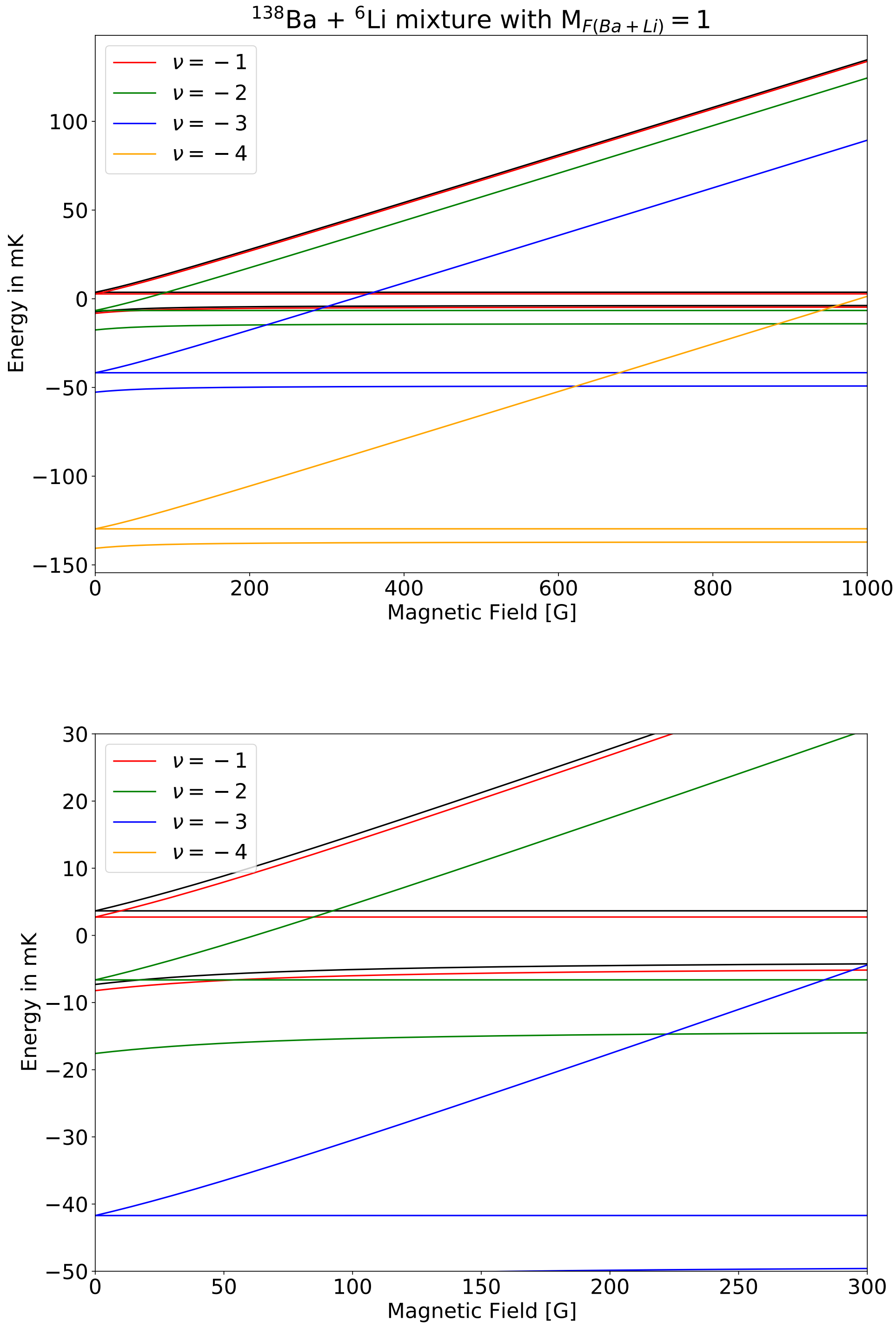

Figure 78: Hyperfine states of the Barium-Lithium mixture with $M_F = 1$ and four the least-bound states: full range and zoom.

calculation of the Feshbach resonances by the multichannel quantum scattering method is much more difficult than the calculation of the collisions in the quantum regime and the spin exchange in the ytterbium experiment. This is due to the fact that we do not know the singlet and triplet scattering lengths as before, but also the configuration of resonances and their number. we do not know how to scale the potential and what scattering length should be set, so it is necessary to test a reasonable scattering length grid. In the case of resonance configurations, the matter is more complicated, we know basically nothing at the starting point. We can expect resonances in s, p and d waves in the considered collision energy range. We do not know which of them correspond to which resonance in the observations and how many should be observed. Therefore, apart from the scattering length, we had to assume all possible variants of resonances and check how they influence the measure defined as the sum of the squares of the distance from the measured position.

$$\chi^2(a_S, a_T) = \sum_{i=1}^{N_{exp}} \left(B_i^{expt} - B_i^{theo}(a_S, a_T)\right)^2 . \tag{82}$$

Fig.79-80 show the resonances for several scattering length configurations both $M_F = 0$ and $M_F = -1$. The resonances have been divided into the three lowest partial waves: s, p, d. We can observe a large level of variability in the behavior of resonances depending on the change in scattering parameters. Both the number of resonances and the partial wave in which they occur changes. Fig.81 also shows the expected disappearance of resonances for the same singlet and triple scattering lengths. This confirms that the calibration of both potentials is correct and the propagation methods are properly convergent. Despite carrying out massive calculations for a large scattering length grid and numerical testing of all possible partial wave configurations, the multi-channel quantum scattering approach without spin-orbit coupling did not give fully satisfactory results. Even the best fit of the resonance positions was not good enough. There were discrepancies in the number of resonances and the acceptable accuracy with respect to the experiment. There were also doubts as to whether all resonances had been measured. At the same time, tests were performed using the asymptotic bound state model, which is much less demanding in terms of computer resources. It allows to determine the bound states in the system at a lower cost and thus to estimate the positions of resonances. Bound states determined by the Molscat module were compatible with those obtained from the asymptotic bound state model, but the preparation and obtaining of results were definitely less convenient and impractical. Therefore, the final estimation of resonances was based on the asymptotic bound state model.

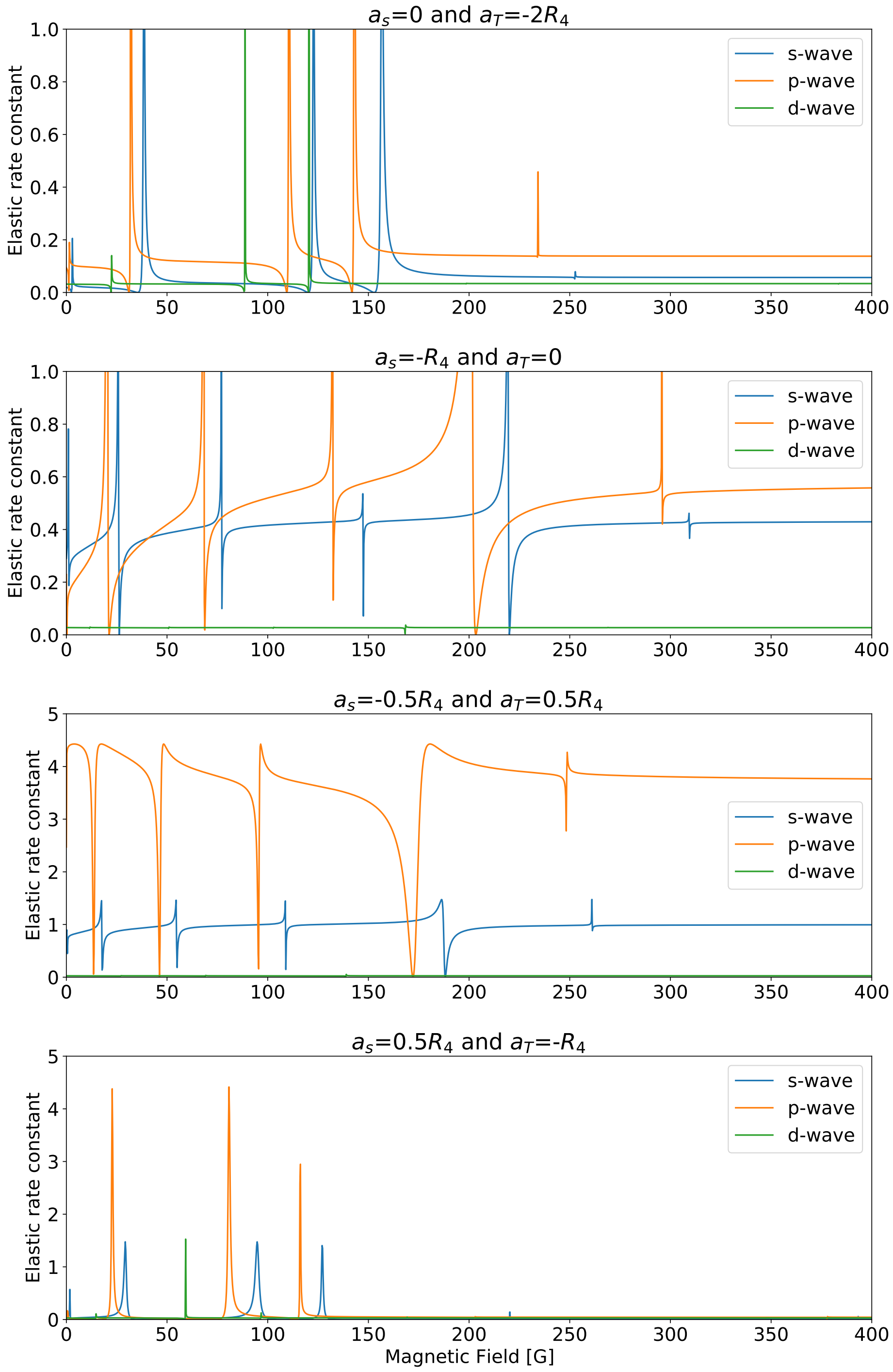

Figure 79: Feshbach resonances of the Barium-Lithium mixture with projection $M_F = 0$.

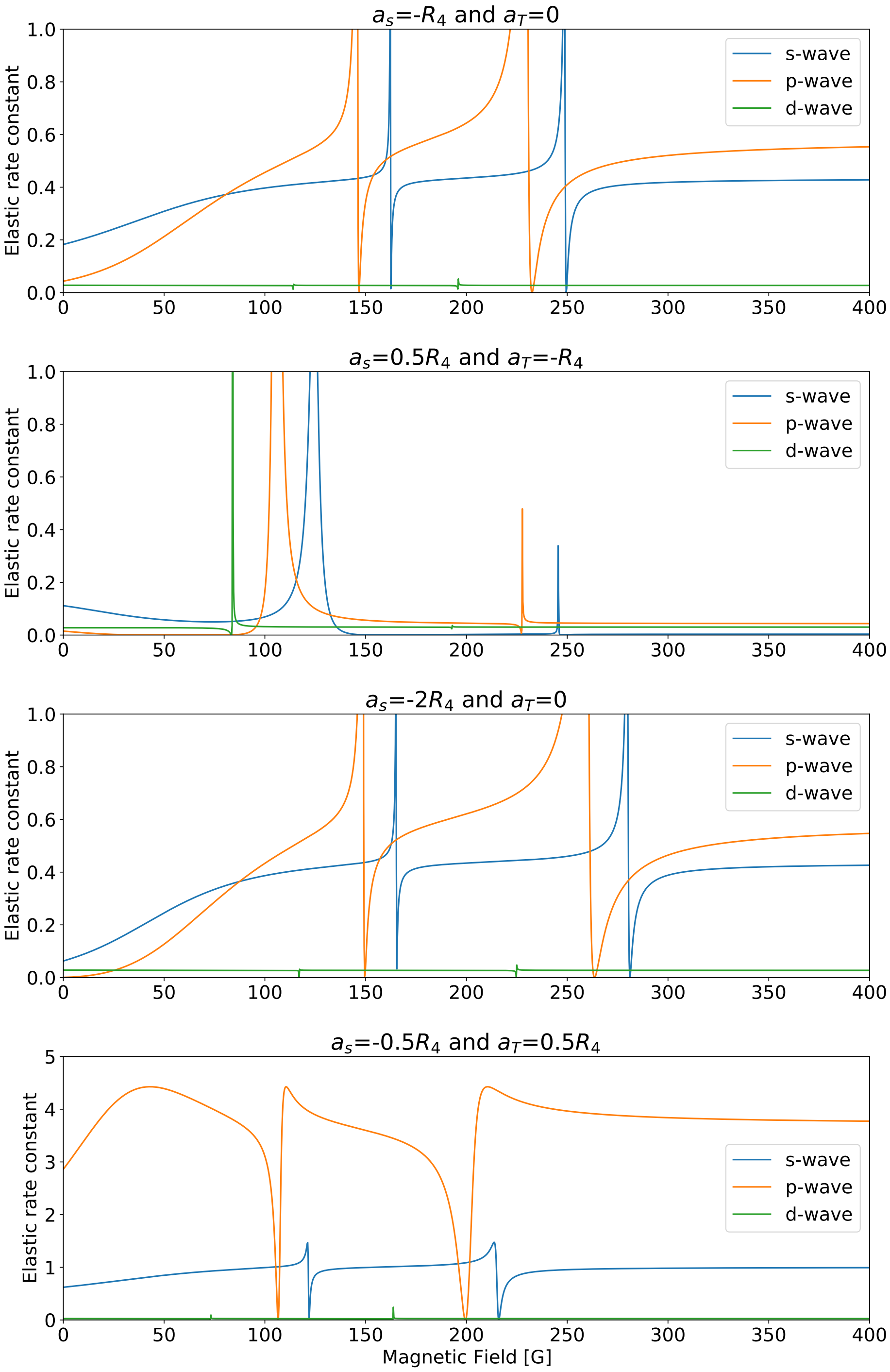

Figure 80: Feshbach resonances of the Barium-Lithium mixture with projection $M_F = -1$.

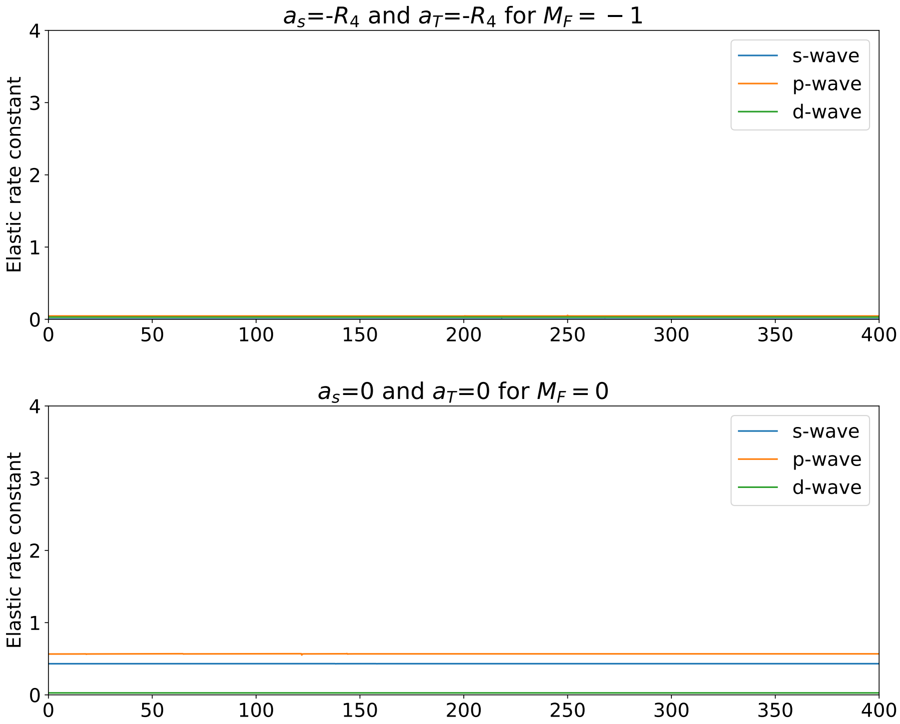

Figure 81: Feshbach resonances of the Barium-Lithium mixture for identical scattering lengths.

### 7.5.3 *Thermal distribution*

So far, when analyzing the ion-atom Feshbach resonances, we have completely ignored the role of thermal distribution of the ion in the radio-frequency trap. Considering that the ion is immersed in the buffer gas and is also subject to micromotion in the trap, we can expect that we need a more general energy distribution. Indeed, this scenario is confirmed by experimental observations and theoretical work. Its consequence is that the mean energy of the ion may in fact be several times greater than the energy of the buffer gas than would result from the thermodynamic equilibrium, moreover, the energy of the ion does not belong to thermal distribution. Experimental observations are often modeled by the Tsallis distribution[142–146]:

$$f(E) = \left(\frac{n_T}{\langle\beta\rangle}\right)^{-k-1} \frac{\Gamma(k+n_T+1)}{\Gamma(k+1)\Gamma(n_T)} \frac{E^k}{\left(\frac{\langle\beta\rangle E}{n_T}+1\right)^{k+n_T+1}} \tag{83}$$

where: E - the ion's energy, $E^k$ - corresponds to the density of states (k=2 for a 3D harmonic oscillator), $\langle\beta\rangle$ represents the mean value of the $\beta = 1/(k_B T)$ and the Tsallis exponent $n_T$ measures "distance" from the thermal equilibrium, with $n_T \to \infty$ for the thermal equilibrium. Therefore, our goal was to check how the Tsallis distribution affects the visibility of resonances, their width and position, including the identification of the correct value of the magnetic field. After carrying out the scattering calculations for the collision energy from 1 to 500 microkelvins and convolution with the Tsallis statistic, it turned out that the thermal effect introduces some corrections, but does not fundamentally affect the identification of resonances.

### 7.5.4 *Bound states*

As mentioned earlier, determining the correct set of resonances and scattering lengths was a process consisting of a combination of: hyperfine state analysis, multichannel quantum scattering without spin-orbit coupling in QDYN and Molscat, analysis of bound states using the asymptotic bound state model and the Molscat program and trials taking into account the spin-orbit coupling in the ABM model and the Molscat program. Each of these steps was important at some stage, because even if it was inefficient, it confirmed the effectiveness and correctness of another method. In this case, the asymptotic bound state model, due to its lightness, turned out to be much more effective in determining the position of resonances. In particular, the search for the right set of scattering lengths, potential scaling and the determination of bound states on this basis is much faster than in the case of quantum scattering calculations. Then the positions of the resonances are determined by the intersections of the bound states, which can be easily identified. Figs.82-83 show the states with four vibrational levels included related to the situation with optimal scattering lengths without spin-orbit coupling. Bound states are presented for $m_F$ = -1,0,1 in relation to atomic states -1,0,1 for partial waves l = 0 or l = 1.2. Details on how the identification of the optimal scattering lengths was achieved will be provided in the next section. At this point, it should be noted that in the general situation, for different sets of scattering lengths, the diagram of bound states is not clearly legible to the naked eye. Numerical analysis is required in order to extract relevant information and compare the diagrams with each other, so we only show the optimal set. As we know, the occurrence of spin-orbit coupling can cause $m_F$ changing resonances and splitting in higher partial waves. Undoubtedly, splitting resonances could appear in experimental observations, but at the moment there is no effective theoretical model that takes into account all these effects together. Finally, only the $m_F$ changing resonances in the s-wave were included in the model. This proved important enough to explain the resonances and assign the scattering lengths in a situation where standard resonances for physical reasons were not observed.

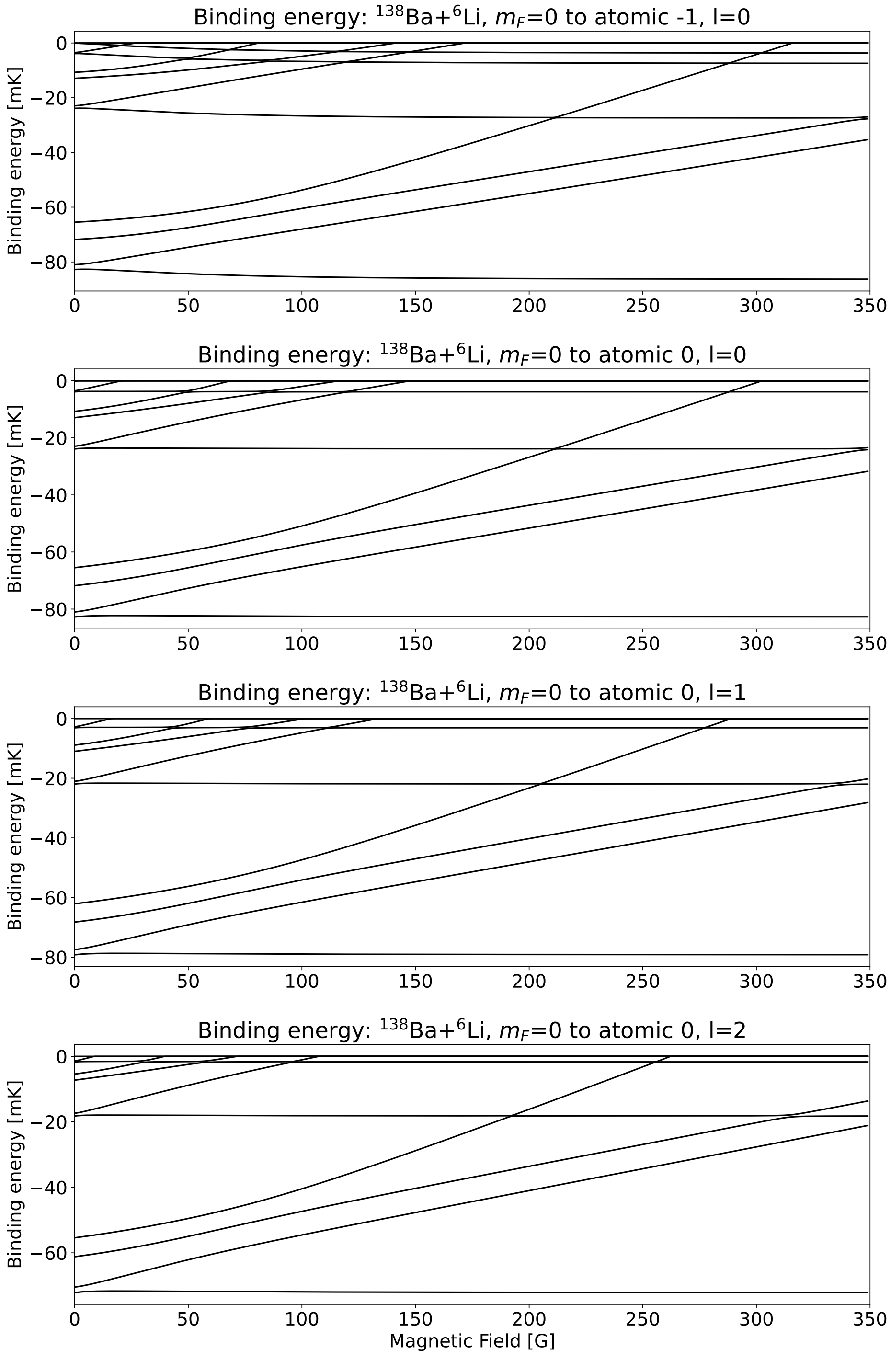

Figure 82: Binding energies without spin-orbit coupling for $Ba^+$/Li mixture for $a_S = 0.236R_4$ and $a_T = -0.053R_4$ ($R_4$=69nm) - $m_F = 0$

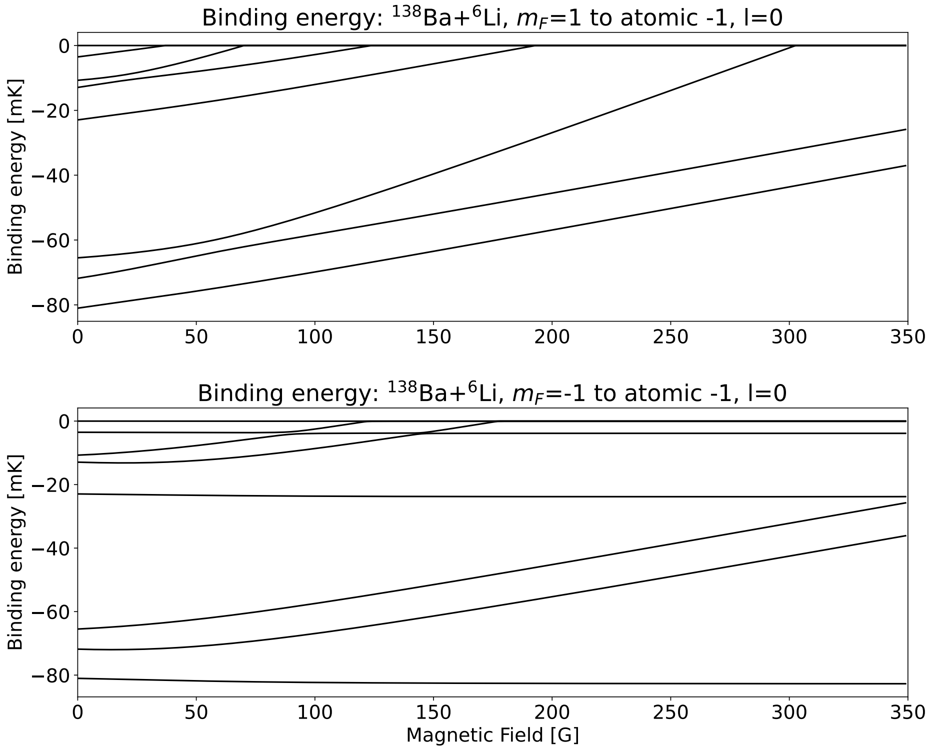

Figure 83: Binding energies without spin-orbit coupling for Ba$^+$/Li mixture for $a_S = 0.236R_4$ and $a_T = -0.053R_4$ ($R_4$=69nm) - $m_F = 1$ and $m_F = -1$

## 7.6 final conclusion on the experimental results.

After a long process of analyzing a very complex structure of all possible resonance configurations, we have reached the final stage, where we have managed to assign a reasonable theoretical explanation to the experimental observation. The full model including higher partial waves was still not well developed, so we limited ourselves only to s-wave resonances to avoid unwanted errors. The original theoretical best estimate, derived from multichannel quantum scattering, was to identify 5(1) resonances in the area under study. Unfortunately, this explanation assumed the possibility of only a spin-projection-conserving interaction ($\delta m_F = 0$), which turned out to be insufficient. Finally, in the experiment in the magnetic field in the range of $B \in [70, 330]$G: 11 resonances were observed (Fig.85). We know from the theoretical part that the spin-orbit coupling significantly influences the mixing of internal spins $m_F$ with rotational spins $(l, m_l)$, especially in the barium-lithium system, this coupling is very large. This means more observed resonances and $m_F$ changing couplings can also split or shift resonances in higher partial waves. At the same time, it has no effect on s-wave resonances up to the first order. In the context of this project, we used the term "l-wave resonance" to denote the situation in which the entrance channel is coupled to the l-wave molecular level. In the published work, resonances which couple the $m_F = -1$ entrance channel to the s-wave were located. Resonances were localized by minimizing the $\chi^2$ (Eq.82) function depending on the singlet and triplet scattering lengths. Initially, 9 resonances were measured: 80.47G, 93.59G, 143.29G, 157.42G, 270.86G, 272.59G, 296.31G, 307.41G, 316.31G, far too many to describe them as s-wave resonances.

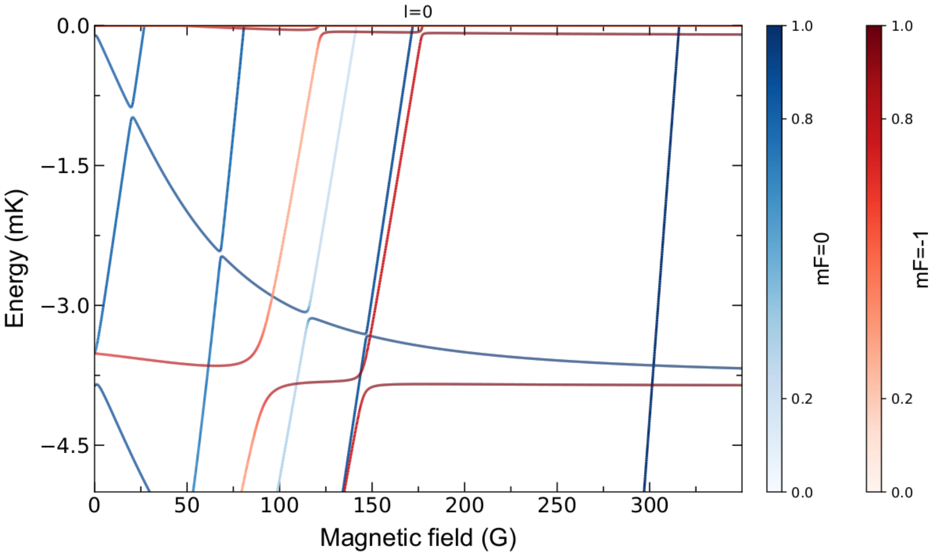

Figure 84: Binding energies of molecular $m_F$ = -1 and $m_F$ = 0 levels, that is relative energies of molecular levels vs atomic threshold for the optimal set of scattering lenghts. Internal data from unpublished preprint (A.Wojciechowska et al.)

The solution to this situation was the calculation of all possible combinations of subsets, where the 2-element subsets were too small to assign scattering lengths, while 4 and more-element subsets could not be described by the theoretical model used. One of the 3-element subsets required additional s-wave resonance for a 172 G magnetic field, which was later measured in the experiment. This allowed to find the best fit of the 4 s-wave resonances in the measured positions: 80.47G, 143.29G, 173.0G, 316.31 G for the scattering length: $a_S = 0.236R4$ and $a_T = -0.053R4$. The $\chi^2$ for other configurations was significantly larger, the model completely omits the explanation of resonances in higher partial waves. The Fig.84 shows the bound states for the optimal set of scattering lengths, from which the identified resonances can be recognized (where colors code triplet admixture). A summary of the measured Feshbach resonances is finally shown graphically in Fig.85 and in the table 3.

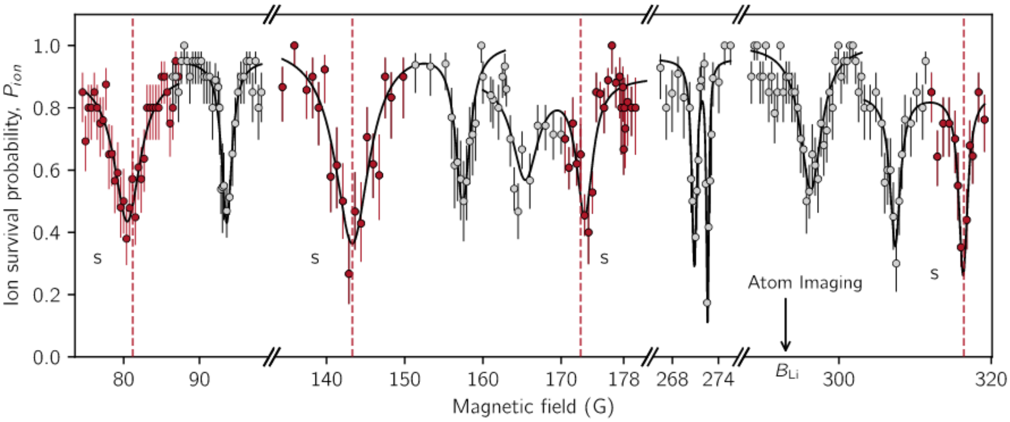

Figure 85: Experimental ion survival probability in the function of magnetic field for single $^{138}Ba^+$ ion embedded into $20(2) \times 10^3$ spin-polarized $^6Li$ atoms. The theoretical positions of the s-wave resonances are indicated by red dashed lines. From Ref.[93]

| List of the measured resonances | | | |
|---|---|---|---|
| $B^{exp}$[G] | $\Delta^{exp}$[G] | $B_s^{theo}$[G] | $t_{int}$[ms] |
| 80.47(21) | 4.2(1.1) | 81.2 | 300 |
| 93.59(9) | 1.6(4) | | 100 |
| 143.29(31) | 5.3(1.3) | 143.3 | 300 |
| 157.42(19) | 2.2(7) | | 300 |
| 165.4(4) | 4.0(1.1) | | 300 |
| 173.0(2) | 2.5(5) | 172.5 | 300 |
| 270.86(5) | 0.76(24) | | 300 |
| 272.59(3) | 0.4(1) | | 300 |
| 296.31(19) | 3.4(7) | | 300 |
| 307.38(14) | 1.6(5) | | 200 |
| 316.31(11) | 1.3(5) | 316.4 | 200 |

Table 3: List of the measured resonances for the entrance channel: $|s^{Ba^+} = 1/2, m_s^{Ba^+} = -1/2\rangle + |f^{Li} = 1/2, m_f^{Li} = -1/2\rangle$ with systematic errors including daily drifts and calibration uncertainties and theorethical prediction for s-wave resonances. Data from Ref.[93].

# 8

# ATOM-MOLECULE INTERACTION

## 8.1 INTRODUCTION

In physics, the problem of an impurity is a well-known issue. As mentioned in the introduction, it can be an impurity having translational degrees of freedom as well as rotational degrees of freedom. Here we would like to focus on the analytical approach to a rotating impurity, but only in the two-body description. This approach is more precisely a description of the effective atom-molecule interaction. Such an effective description of the atom-molecule interaction can be introduced mathematically with the aid of a pseudo-potential, which represents the properties of the system with mathematical simplicity, and also ensures the self-adjointness of the Hamiltonian. This approach to the problem has been used many times, starting with the famous work on the interaction of two cold atoms, where the regularized contact potential in the form of the Dirac delta was used[22]. In this case, the pseudopotential will be a bit more general, as it will contain the anisotropic character of the atom-molecule interactions and take into account the rotational structure of the molecule. To begin with, we introduce the general Hamiltonian representing the atom and molecule, specifically the kinetic terms, the isotropic harmonic potential, and the rotational structure

$$\hat{H}_0 = -\frac{1}{2m_1}\nabla_1^2 - \frac{1}{2m_2}\nabla_2^2 + \frac{1}{2}m_1 r_1^2 + \frac{1}{2}m_2 r_2^2 + B\hat{j}^2. \tag{84}$$

By introducing the following notations, we can divide the Hamiltonian into the motion of the center of mass and the relative motion

$$\begin{aligned} R &= \frac{m_1 r_1 + m_2 r_2}{m_1 + m_2} \quad \text{and} \quad r = r_1 - r_2 \\ \mu &= \frac{m_1 m_2}{m_1 + m_2} \quad \text{and} \quad M = m_1 + m_2 \end{aligned} \tag{85}$$

After transforming the coordinates, we get:

$$\hat{H}_0 = -\frac{1}{2M}\nabla_R^2 - \frac{1}{2\mu}\nabla_r^2 + B\hat{j}^2 + \frac{1}{2}MR^2 + \frac{1}{2}\mu r^2. \tag{86}$$

We assume that atom and molecule interact with each other via anisotropic potential:

$$\hat{H} = \hat{H}_0 + \hat{V}(r,\theta), \tag{87}$$

where the general form of the anisotropic potential can be divided into isotropic and anisotropic parts:

$$\hat{V}(r,\theta) = \hat{V}_{sph}(r) + \hat{V}_{anis}(r,\theta). \tag{88}$$

Having the initial information on the physical system and the notation used, we move on to the introduction of the anisotropic potential in the next section.

## 8.2 PSEUDO-POTENTIAL

As mentioned earlier, we are introducing the analytical effective potential, called a pseudopotential[7]. The pseudopotential represents the physical properties of the interaction and has correctly defined operators in the mathematical context. This approach has been used many times in various situations: anisotropic interactions[147–149], for dipoles[150], or for spin-orbit interactions[151, 152]. In our case, for the atom-molecule interaction, in particular, it contains the anisotropy of the interaction and the possibility of angular momentum flow between the rotation of the molecule and the relative rotation. We start with the general form of the expression with the reactance matrix $K_{lm}^{l'm'}$ parametrizing the multichannel scattering for the angular momentum of the relative rotation: $l, m, l', m'$:

$$\hat{V}_{JM}^{ps}\Phi = -\frac{\hbar^2}{2\mu}\sum_{lm,l'm'}\frac{\mathcal{K}_{lm}^{l'm'}}{k^{l+l'+1}}\hat{V}_{JM}^{lm,l'm'}\Phi, \tag{89}$$

and the operator $\hat{V}_{JM}^{lm,l'm'}$ for total angular momentum J, its action on states has the following form:

$$\hat{V}_{JM}^{lm,l'm'}\psi(\vec{r}) = \frac{(2l)!(2l+1)}{2^{l+l'}l!l'!}\sum_{jm_j} C_{lm_ljm_j}^{JM} Y_{jm_j}(\Omega_j)Y_{lm_l}(\Omega_l)\frac{1}{r^2}\frac{1}{l!}\left(\frac{\overleftarrow{\partial^l}}{\partial r^l}\right)\delta(r)$$
$$\times\left[\frac{\partial}{\partial r^{2l'+1}}\left(r^{l'+1}\int d\Omega_{j'}\sum_{j'm_{j'}} C_{l'm_{l'}j'm_{j'}}^{JM} Y_{j'm_{j'}}^*(\Omega_{j'})\int d\Omega_{l'}Y_{l'm_{l'}}^*(\Omega_{l'})\psi(\vec{r})\right)\right]_{r=0}, \tag{90}$$

where: $Y_{l,m_l}$ - spherical harmonics, $C_{lm_ljm_j}^{JM}$ - Clebsch-Gordan coefficients and indices $j, m_j$ correspond to the rotational states of the molecule. It can be shown that the scattering lengths for this type of contact anisotropic interaction can be introduced as follows:

$$a_{l,l'} = -\lim_{k\to 0}\frac{\mathcal{K}_{lm}^{l'm'}}{k^{l+l'+1}}, \tag{91}$$

We expand the wave function $\psi$ into eigenfunctions of the isotropic harmonic oscillator and spherical harmonics describing the relative rotation and the molecule rotation:

$$\psi(\vec{r}) = \sum_{n,l,jm_j} a_{lm_ljm_j}^{n} R_{nl}(r)Y_{lm_l}(\Omega_l)Y_{jm_j}(\Omega_j), \tag{92}$$

where:

$$R_{nl}(r) = \sqrt{\frac{2^{l+2}}{(2l+1)!!\pi^{1/2}L_n^{(l+1/2)}(0)}}e^{-r^2/2}r^l L_n^{(l+1/2)}(r^2) \tag{93}$$

and $L_n^{(\alpha)}$ - generalized Laguerre polynomials.

Using the introduced terminology, for selected values of the total angular momentum J = 0,1,2, we can act the pseudo-potential operator on the wave function, and then carry out a projection on the basis states. Then we will obtain equations, the solution of which will allow us to obtain the relationship between energy and scattering lengths.

### 8.2.1 *Solution for* $J = 0$

We start our analysis with the case $J = 0$, then the pseudo-potential has the following form:

$$\hat{V}^{ps}_{00}\psi = \frac{\hbar^2}{2\mu}\left[a_s\hat{V}^{00,00}_{00} + a_{sp}(\hat{V}^{10,00}_{00} + \hat{V}^{00,10}_{00}) + a_{pp}\hat{V}^{10,10}_{00}\right]\psi. \tag{94}$$

#### 8.2.1.1 *s-p coupling*

Using the general formula, we calculate the action of each term:

$$\hat{V}^{00,00}_{00}\psi = Y_{00}(\Omega_j)Y_{00}(\Omega_l)\frac{1}{r^2}\delta(r)\frac{\partial}{\partial r}\left(r\sum_n a_{n00}R_{n0}(r)\right) \tag{95}$$

$$\begin{aligned}\hat{V}^{10,00}_{00}\psi &= 3C^{00}_{10,10}Y_{10}(\Omega_j)Y_{10}(\Omega_l)\frac{1}{r^2}\left(\frac{\overleftarrow{\partial}}{\partial r}\right)\\ &\times \delta(r)\frac{\partial}{\partial r}\left(r\sum_n a_{n00}R_{n0}(r)\right)_{r=0}\end{aligned} \tag{96}$$

$$\begin{aligned}\hat{V}^{00,10}_{00}\psi &= \frac{1}{2}Y_{00}(\Omega_j)Y_{00}(\Omega_l)\frac{1}{r^2}\\ &\times \delta(r)\frac{\partial^3}{\partial r^3}\left(r^2C^{00}_{10,10}\sum_n a_{n11}R_{n1}(r)\right)_{r=0}\end{aligned} \tag{97}$$

$$\begin{aligned}\hat{V}^{10,10}_{00}\psi &= \frac{3}{2}C^{00}_{10,10}Y_{10}(\Omega_j)Y_{10}(\Omega_l)\frac{1}{r^2}\left(\frac{\overleftarrow{\partial}}{\partial r}\right)\\ &\times \delta(r)\frac{\partial^3}{\partial r^3}\left(r^2C^{00}_{10,10}\sum_n a_{n11}R_{n1}(r)\right)_{r=0}\end{aligned} \tag{98}$$

Finally, we get two equations that we can solve in a standard way by eliminating A and B, which are a shortened notation of the respective sums standing next to a given term. This is possible by inserting $a_{nlj}$ coefficients from the equations below into them

$$(\varepsilon_{k00} - \varepsilon)a_{k00} + R^*_{k0}(0)\left(\frac{a_s}{2}A + \frac{a_{sp}}{4}B\right) = 0, \tag{99}$$

$$(\varepsilon_{k11} - \varepsilon)a_{k11} + \left(\frac{\partial}{\partial r'}R^*_{k1}(r')\right)_{r'=0}\left(\frac{3a_{sp}}{2}A + \frac{3a_{pp}}{4}B\right)C^{00}_{10,10} = 0. \tag{100}$$

Then we get:

$$\frac{2}{S_{00}} - a_s - \frac{a^2_{sp}}{\left(\frac{4}{3S_{11}C^{00}_{10,10}} - a_{pp}\right)} = 0, \tag{101}$$

where sums:

$$S_{00} = 4\frac{\Gamma(-\varepsilon/2+3/4)}{\Gamma(-\varepsilon/2+1/4)}, \tag{102}$$

$$S_{11} = -\frac{2^5}{3}C^{00}_{10,10}\frac{\Gamma(-\varepsilon/2+B+5/4)}{\Gamma(-\varepsilon/2+B-1/4)}, \tag{103}$$

are calculated from the general rule shown in the appendix A.1.

$$\frac{\Gamma(-\varepsilon/2+1/4)}{2\Gamma(-\varepsilon/2+3/4)} - a_s - \frac{a^2_{sp}}{\left(-\frac{3\Gamma(-\varepsilon/2+B-1/4)}{2^3\Gamma(-\varepsilon/2+B+5/4)} - a_{pp}\right)} = 0. \tag{104}$$

### 8.2.2 *Solution for* $J = 1$

The next case we take into account is $J = 1$, then the pseudo-potential takes the form:

$$\begin{aligned}\hat{V}^{ps}_{10}\psi = \frac{\hbar^2}{2\mu}[a_s\hat{V}^{00,00}_{10} + a_{sp}(\hat{V}^{10,00}_{10} + \hat{V}^{00,10}_{10})\\ + a_{sd}(\hat{V}^{20,00}_{10} + \hat{V}^{00,20}_{10}) + a_{pp}\hat{V}^{10,10}_{10} + a_{dd}\hat{V}^{20,20}_{10}]\psi.\end{aligned} \tag{105}$$

#### 8.2.2.1 *s-p-d coupling*

Using the same technique as before (details in the appendix A.2), we get the equations:

$$(\varepsilon_{k01} - \varepsilon)a_{k01} + R^*_{k0}(0)\left(\frac{a_s}{2}C^{10}_{00,10}A + \frac{a_{sp}}{4}C^{10}_{00,10}B + \frac{a_{sd}}{16}C^{10}_{00,10}C\right) = 0, \tag{106}$$

$$(\varepsilon_{k10} - \varepsilon)a_{k10} + \left(\frac{\partial}{\partial r'}R^*_{k1}(r')\right)_{r'=0}\left(\frac{3a_{sp}}{2}C^{10}_{10,00}A + \frac{3a_{pp}}{4}C^{10}_{10,00}B\right) = 0,$$

(107)

$$(\varepsilon_{k21}-\varepsilon)a_{k21}+\left(\frac{1}{2}\frac{\partial^2}{\partial r'^2}R^*_{k2}(r')\right)_{r'=0}\left(\frac{15a_{sd}}{2}C^{10}_{20,10}A+\frac{15a_{dd}}{16}C^{10}_{20,10}C\right)=0. \tag{108}$$

Here again, A, B, C are shorthand for the sums appearing in expressions. After substituting the coefficients, they were changed to the shorthand notation X, Y, Z.

$$-X+\frac{a_s}{2}S_{01}X+\frac{a_{sp}}{4k}S_{10}Y+\frac{a_{sd}}{16k^2}S_{21}Z=0, \tag{109}$$

$$-Y+\frac{3a_{sp}}{2k}S_{01}X+\frac{3a_{pp}}{4k^2}S_{10}Y=0, \tag{110}$$

$$-Z+\frac{15a_{sd}}{2k^2}S_{01}C^{10}_{20,10}X+\frac{15a_{dd}}{16k^4}S_{21}C^{10}_{20,10}Z=0. \tag{111}$$

After solving the system of equations, we get:

$$-\frac{2}{S_{01}}+a_s+\frac{a_{sp}^2}{(\frac{4}{3S_{10}}-a_{pp})}+\frac{a_{sd}^2}{(\frac{16}{15S_{21}C^{10}_{20,10}}-a_{dd})}=0, \tag{112}$$

where:

$$S_{21}=-\sqrt{\frac{2}{5}}\frac{2^9}{15}\frac{\Gamma(-\varepsilon/2+B+7/4)}{\Gamma(-\varepsilon/2+B-3/4)}, \tag{113}$$

$$S_{10}=-\frac{2^5}{3}\frac{\Gamma(-\varepsilon/2+5/4)}{\Gamma(-\varepsilon/2-1/4)}, \tag{114}$$

$$S_{01}=4\frac{\Gamma(-\varepsilon/2+B+3/4)}{\Gamma(-\varepsilon/2+B+1/4)}, \tag{115}$$

which were calculated in appendix A.3 and finally:

$$\begin{aligned}&\frac{\Gamma(-\varepsilon/2+B+1/4)}{2\Gamma(-\varepsilon/2+B+3/4)}-a_s-\frac{a_{sp}^2}{(-\frac{\Gamma(-\varepsilon/2-1/4)}{2^3\Gamma(-\varepsilon/2+5/4)}-a_{pp})}\\&-\frac{a_{sd}^2}{(\frac{5\Gamma(-\varepsilon/2+B-3/4)}{2^6\Gamma(-\varepsilon/2+B+7/4)}-a_{dd})}=0.\end{aligned} \tag{116}$$

### 8.2.3 *Solution for* $J=2$

In the last analyzed case, $J=2$, we consider only the p-d coupling, because we assume that the molecule is in the rotational ground state or only the first excited state

$$\hat{V}^{ps}_{20}\psi=\frac{\hbar^2}{2\mu}\left[a_{pp}\hat{V}^{10,10}_{20}+a_{pd}(\hat{V}^{20,10}_{20}+\hat{V}^{10,20}_{20})+a_{dd}\hat{V}^{20,20}_{20}\right]\psi. \tag{117}$$

#### 8.2.3.1 *p-d coupling*

Similarly as before, we get the following equations (details in appendix A.4):

$$(\varepsilon_{k11}-\varepsilon)a_{k11}+\left(\frac{\partial}{\partial r'}R^{*}_{k1}(r')\right)_{r'=0}\left(\frac{3a_{pp}}{4}C^{20}_{10,10}A+\frac{3a_{pd}}{16}C^{20}_{10,10}B\right)=0, \tag{118}$$

$$(\varepsilon_{k20}-\varepsilon)a_{k20}+\frac{1}{2}\left(\frac{\partial^{2}}{\partial r'^{2}}R^{*}_{k2}(r')\right)_{r'=0}\left(\frac{15a_{pd}}{4}C^{20}_{20,10}A+\frac{15a_{dd}}{16}C^{20}_{20,00}B\right)=0. \tag{119}$$

Substituting the coefficients and changing symbols we get:

$$-X+\frac{3}{4}a_{pp}C^{20}_{10,10}S_{11}X+\frac{3}{16}a_{pd}C^{20}_{10,10}S_{20}Y=0, \tag{120}$$

$$-Y+\frac{15}{4}a_{pd}C^{20}_{20,00}S_{11}X+\frac{15}{16}a_{dd}C^{20}_{20,00}S_{20}Y=0, \tag{121}$$

and hence the solution:

$$\frac{-4}{3S_{11}}+a_{pp}C^{20}_{10,10}+\frac{C^{20}_{10,10}a^{2}_{pd}}{\left(\frac{16}{15S_{20}C^{20}_{20,00}}-a_{dd}\right)}=0. \tag{122}$$

# 9

# SUMMARY

The results of experimental and theoretical research have shown cross-sectional topics of contemporary research in the field of ultracold ion-atom collisions. The first ever observation of ion-atom collisions in the quantum regime was a spectacular experimental project, but also a computational challenge. The final success and obtaining a reliable confirmation of the measured data would not be possible without theoretical and experimental cooperation. The same conclusion applies to the history of the experiment with the first-ever observation of Feshbach resonances in the ion-atom system. A very important experiment from the perspective of the further development of this field. The ability to reach temperatures in the quantum regime and to control interactions is an excellent starting point for further research and development of methods for controlling ion-atom systems. Regardless of this, there are still open questions about the properties of the barium-lithium mixture itself, such as the very large spin-orbit coupling, a full explanation of the processes generated by this coupling and the description of resonances in higher partial waves. We can certainly expect many more great results from this mixture. Also, the results obtained by the anisotropic atom-molecule pseudopotential, if skillfully used, can be useful in describing rotating impurities or simply used to the description of real atom-molecule collisions.

# Part V

# APPENDIX

# A

# APPENDIX

## A.1 CALCULATION OF THE SUM

$$\nu = \varepsilon/2 - l/2 - Bj(j+1)/2 - 3/4, \tag{123}$$

$$\begin{aligned}
&\sum_{n=0}^{\infty} \frac{L_n^{(l+1/2)}(r^2)}{n-\nu} \\
&= \sum_{n=0}^{\infty} \int_0^{\infty} \frac{dy}{(1+y)^2} \left(\frac{y}{1+y}\right)^{n-\nu-1} L_n^{(l+1/2)}(r^2) \\
&= \int_0^{\infty} \frac{(y+1)^{l+3/2}}{(1+y)^2} \left(\frac{y}{1+y}\right)^{-\nu-1} e^{-r^2 y} dy \\
&= \int_0^{\infty} (y+1)^{l+1/2+\nu} y^{-\nu-1} e^{-r^2 y} dy = \Gamma(-\nu) \\
&\times U(-\nu, l+3/2, r^2),
\end{aligned} \tag{124}$$

$$\begin{aligned}
&\Gamma(-\nu)[U(-\nu, l+3/2, r^2)]_{r=0} \\
&= \frac{\pi}{\sin(\pi(l+3/2))} \frac{\Gamma(-\nu)}{\Gamma(-\nu-l-1/2)\Gamma(l+3/2)}.
\end{aligned} \tag{125}$$

## A.2 S-P-D COUPLING FOR $J = 1$

$$\begin{aligned}
&\hat{V}_{10}^{00,00}\psi = C_{00,10}^{10} Y_{10}(\Omega_j) Y_{00}(\Omega_l) \frac{1}{r^2} \\
&\times \delta(r) \frac{\partial}{\partial r} \left( r C_{00,10}^{10} \sum_n a_{n01} R_{n0}(r) \right)_{r=0},
\end{aligned} \tag{126}$$

$$\begin{aligned}
&\hat{V}_{10}^{10,00}\psi = 3 C_{10,00}^{10} Y_{00}(\Omega_j) Y_{10}(\Omega_l) \frac{1}{r^2} \left( \frac{\overleftarrow{\partial}}{\partial r} \right) \\
&\times \delta(r) \frac{\partial}{\partial r} \left( r C_{00,10}^{10} \sum_n a_{n01} R_{n0}(r) \right)_{r=0},
\end{aligned} \tag{127}$$

$$\begin{aligned}
&\hat{V}_{10}^{00,10}\psi = \frac{1}{2} C_{00,10}^{10} Y_{10}(\Omega_j) Y_{00}(\Omega_l) \frac{1}{r^2} \\
&\times \delta(r) \frac{\partial^3}{\partial r^3} \left( r^2 C_{10,00}^{10} \sum_n a_{n10} R_{n1}(r) \right)_{r=0},
\end{aligned} \tag{128}$$

$$\begin{aligned}\hat{V}_{10}^{10,10}\psi &= \frac{3}{2}C_{10,00}^{10}Y_{00}(\Omega_j)Y_{10}(\Omega_l)\frac{1}{r^2}\left(\frac{\overleftarrow{\partial}}{\partial r}\right)\\ &\times \delta(r)\frac{\partial^3}{\partial r^3}\left(r^2 C_{10,00}^{10}\sum_n a_{n10}R_{n1}(r)\right)_{r=0},\end{aligned} \tag{129}$$

$$\begin{aligned}\hat{V}_{10}^{20,20}\psi &= \frac{15}{8}C_{20,10}^{10}Y_{10}(\Omega_j)Y_{20}(\Omega_l)\frac{1}{2r^2}\left(\frac{\overleftarrow{\partial^2}}{\partial r^2}\right)\\ &\times \delta(r)\frac{\partial^5}{\partial r^5}\left(r^3 C_{20,10}^{10}\sum_n a_{n21}R_{n2}(r)\right)_{r=0},\end{aligned} \tag{130}$$

$$\begin{aligned}\hat{V}_{10}^{00,20}\psi &= \frac{1}{8}C_{00,10}^{10}Y_{10}(\Omega_j)Y_{00}(\Omega_l)\frac{1}{r^2}\\ &\times \delta(r)\frac{\partial^5}{\partial r^5}\left(r^3 C_{20,10}^{10}\sum_n a_{n21}R_{n2}(r)\right)_{r=0},\end{aligned} \tag{131}$$

$$\begin{aligned}\hat{V}_{10}^{20,00}\psi &= 15C_{20,10}^{10}Y_{10}(\Omega_j)Y_{20}(\Omega_l)\frac{1}{2r^2}\left(\frac{\overleftarrow{\partial^2}}{\partial r^2}\right)\\ &\times \delta(r)\frac{\partial}{\partial r}\left(rC_{00,10}^{10}\sum_n a_{n01}R_{n0}(r)\right)_{r=0}.\end{aligned} \tag{132}$$

## A.3 CALCULATION OF THE ADDITIONAL SUMS

$$S_{21} = \frac{\partial^5}{\partial r^5}\left(r^3 C_{20,10}^{10}\sum_n \frac{\frac{1}{2}\left(\frac{\partial^2}{\partial r'^2}R_{n2}^*(r')\right)_{r'=0}R_{n2}(r)}{\varepsilon-\varepsilon_{n21}}\right)_{r=0}, \tag{133}$$

$$\nu = \varepsilon/2 - l/2 - Bj(j+1)/2 - 3/4, \tag{134}$$

$$\begin{aligned}S_{21} &= -C_{20,10}^{10}\frac{2^4}{15\pi^{1/2}}\frac{\partial^5}{\partial r^5}\left(r^3\sum_n \frac{e^{-r^2/2}r^2L_n^{(5/2)}(r^2)}{2(n-\nu)}\right)_{r=0}\\ &= -C_{20,10}^{10}\frac{2^4}{15\pi^{1/2}}60\sum_n\frac{L_n^{(5/2)}(0)}{n-\nu},\end{aligned} \tag{135}$$

$$\begin{aligned}S_{21} &= -C_{20,10}^{10}\frac{2^4}{15\pi^{1/2}}60\frac{2^3}{15\pi^{1/2}}(-\pi)\frac{\Gamma(-\nu)}{\Gamma(-\nu-l-1/2)}\\ &= -\sqrt{\frac{2}{5}}\frac{2^9}{15}\frac{\Gamma(-\varepsilon/2+B+7/4)}{\Gamma(-\varepsilon/2+B-3/4)}.\end{aligned} \tag{136}$$

## A.4 P-D COUPLING FOR $J = 2$

$$\begin{aligned}\hat{V}_{20}^{10,10}\psi = {}& \frac{3}{2}C_{10,10}^{20}Y_{10}(\Omega_j)Y_{10}(\Omega_l)\frac{1}{r^2}\left(\frac{\overleftarrow{\partial}}{\partial r}\right) \\ & \times \delta(r)\frac{\partial^3}{\partial r^3}\left(r^2 C_{10,10}^{20}\sum_n a_{n11}R_{n1}(r)\right)_{r=0},\end{aligned} \tag{137}$$

$$\begin{aligned}\hat{V}_{20}^{20,10}\psi = {}& \frac{15}{2}C_{20,00}^{20}Y_{00}(\Omega_j)Y_{20}(\Omega_l)\frac{1}{2r^2}\left(\frac{\overleftarrow{\partial^2}}{\partial r^2}\right) \\ & \times \delta(r)\frac{\partial^3}{\partial r^3}\left(r^2 C_{10,10}^{20}\sum_n a_{n11}R_{n1}(r)\right)_{r=0},\end{aligned} \tag{138}$$

$$\begin{aligned}\hat{V}_{20}^{10,20}\psi = {}& \frac{3}{8}C_{10,10}^{20}Y_{10}(\Omega_j)Y_{10}(\Omega_l)\frac{1}{r^2}\left(\frac{\overleftarrow{\partial}}{\partial r}\right) \\ & \times \delta(r)\frac{\partial^5}{\partial r^5}\left(r^3 C_{20,00}^{20}\sum_n a_{n20}R_{n2}(r)\right)_{r=0},\end{aligned} \tag{139}$$

$$\begin{aligned}\hat{V}_{20}^{20,20}\psi = {}& \frac{15}{8}C_{20,00}^{20}Y_{00}(\Omega_j)Y_{20}(\Omega_l)\frac{1}{2r^2}\left(\frac{\overleftarrow{\partial^2}}{\partial r^2}\right) \\ & \times \delta(r)\frac{\partial^5}{\partial r^5}\left(r^3 C_{20,00}^{20}\sum_n a_{n20}R_{n2}(r)\right)_{r=0}.\end{aligned} \tag{140}$$

# BIBLIOGRAPHY

[1] M. Tomza, K. Jachymski, R. Gerritsma, A. Negretti, T. Calarco, Z. Idziaszek, and P. S. Julienne, "Cold hybrid ion-atom systems," Rev. Mod. Phys. **91**, 035001 (2019).

[2] I. Bloch, J. Dalibard, and W. Zwerger, "Many-body physics with ultracold gases," Rev. Mod. Phys. **80**, 885–964 (2008).

[3] M. Lewenstein, A. Sanpera, V. Ahufinger, B. Damski, A. Sen(De), and U. Sen, "Ultracold atomic gases in optical lattices: mimicking condensed matter physics and beyond," Adv. Phys. **56**, 243–379 (2007).

[4] C. Chin, R. Grimm, P. Julienne, and E. Tiesinga, "Feshbach resonances in ultracold gases," Rev. Mod. Phys. **82**, 1225–1286 (2010).

[5] M. Lewenstein, A. Sanpera, and V. Ahufinger, *Ultracold Atoms in Optical Lattices* (Oxford University Press, 2012).

[6] C. J. Pethick and H. Smith, *Bose–Einstein Condensation in Dilute Gases* (Cambridge University Press, 2008).

[7] K. Huang and C. N. Yang, "Quantum-mechanical many-body problem with hard-sphere interaction," Phys. Rev. **105**, 767–775 (1957).

[8] I. Bloch, "Ultracold quantum gases in optical lattices," Nature Phys. **1**, 23–30 (2005).

[9] O. Dutta, M. Gajda, P. Hauke, M. Lewenstein, D.-S. Lühmann, B. A. Malomed, T. Sowiński, and J. Zakrzewski, "Non-standard hubbard models in optical lattices: a review," Rep. Prog. Phys. **78**, 066001 (2015).

[10] P. W. Anderson, "Absence of diffusion in certain random lattices," Phys. Rev. **109**, 1492–1505 (1958).

[11] G. Roati, C. D'Errico, L. Fallani, M. Fattori, C. Fort, M. Zaccanti, G. Modugno, M. Modugno, and M. Inguscio, "Anderson localization of a non-interacting bose–einstein condensate," Nature **453**, 895–898 (2008).

[12] J. Billy, V. Josse, Z. Zuo, A. Bernard, B. Hambrecht, P. Lugan, D. Clément, L. Sanchez-Palencia, P. Bouyer, and A. Aspect, "Direct observation of anderson localization of matter waves in a controlled disorder," Nature **453**, 891–894 (2008).

[13] M. Serbyn, Z. Papić, and D. A. Abanin, "Local conservation laws and the structure of the many-body localized states," Phys. Rev. Lett. **111**, 127201 (2013).

[14] M. Serbyn, Z. Papić, and D. A. Abanin, "Universal slow growth of entanglement in interacting strongly disordered systems," Phys. Rev. Lett. **110**, 260601 (2013).

[15] M. Žnidarič, T. c. v. Prosen, and P. Prelovšek, "Many-body localization in the heisenberg xxz magnet in a random field," Phys. Rev. B **77**, 064426 (2008).

[16] F. Alet and N. Laflorencie, "Many-body localization: An introduction and selected topics," C. R. Phys. **19**, 498–525 (2018).

[17] M. Schreiber, S. S. Hodgman, P. Bordia, H. P. Lüschen, M. H. Fischer, R. Vosk, E. Altman, U. Schneider, and I. Bloch, "Observation of many-body localization of interacting fermions in a quasirandom optical lattice," Science **349**, 842–845 (2015).

[18] P. Sierant, D. Delande, and J. Zakrzewski, "Many-body localization due to random interactions," Phys. Rev. A **95**, 021601 (2017).

[19] J. yoon Choi, S. Hild, J. Zeiher, P. Schauß, A. Rubio-Abadal, T. Yefsah, V. Khemani, D. A. Huse, I. Bloch, and C. Gross, "Exploring the many-body localization transition in two dimensions," Science **352**, 1547–1552 (2016).

[20] D. Wiater and J. Zakrzewski, "Impact of geometry on many-body localization," Phys. Rev. B **98**, 094202 (2018).

[21] T. Grining, M. Tomza, M. Lesiuk, M. Przybytek, M. Musiał, R. Moszynski, M. Lewenstein, and P. Massignan, "Crossover between few and many fermions in a harmonic trap," Phys. Rev. A **92**, 061601 (2015).

[22] T. Busch, B.-G. Englert, K. Rzażewski, and M. Wilkens, Found. Phys. **28**, 549–559 (1998).

[23] T. Sowiński, T. Grass, O. Dutta, and M. Lewenstein, "Few interacting fermions in a one-dimensional harmonic trap," Phys. Rev. A **88**, 033607 (2013).

[24] A. Dawid, M. Lewenstein, and M. Tomza, "Two interacting ultracold molecules in a one-dimensional harmonic trap," Phys. Rev. A **97**, 063618 (2018).

[25] B. Paredes, A. Widera, V. Murg, O. Mandel, S. Fölling, I. Cirac, G. V. Shlyapnikov, T. W. Hänsch, and I. Bloch, "Tonks–girardeau gas of ultracold atoms in an optical lattice," Nature **429**, 277–281 (2004).

[26] G. Pagano, M. Mancini, G. Cappellini, P. Lombardi, F. Schäfer, H. Hu, X.-J. Liu, J. Catani, C. Sias, M. Inguscio, and L. Fallani, "A one-dimensional liquid of fermions with tunable spin," Nature Phys. **10**, 198–201 (2014).

[27] F. Serwane, G. Zürn, T. Lompe, T. B. Ottenstein, A. N. Wenz, and S. Jochim, "Deterministic preparation of a tunable few-fermion system," Science **332**, 336–338 (2011).

[28] T. Kinoshita, T. Wenger, and D. S. Weiss, "Observation of a one-dimensional tonks-girardeau gas," Science **305**, 1125–1128 (2004).

[29] L. Anderegg, L. W. Cheuk, Y. Bao, S. Burchesky, W. Ketterle, K.-K. Ni, and J. M. Doyle, "An optical tweezer array of ultracold molecules," Science **365**, 1156–1158 (2019).

[30] L. R. Liu, J. D. Hood, Y. Yu, J. T. Zhang, N. R. Hutzler, T. Rosenband, and K.-K. Ni, "Building one molecule from a reservoir of two atoms," Science **360**, 900–903 (2018).

[31] A. N. Wenz, G. Zürn, S. Murmann, I. Brouzos, T. Lompe, and S. Jochim, "From few to many: Observing the formation of a fermi sea one atom at a time," Science **342**, 457–460 (2013).

[32] D. Leibfried, R. Blatt, C. Monroe, and D. Wineland, "Quantum dynamics of single trapped ions," Rev. Mod. Phys. **75**, 281–324 (2003).

[33] H. Haffner, C. Roos, and R. Blatt, "Quantum computing with trapped ions," Phys. Rep. **469**, 155–203 (2008).

[34] R. Blatt and D. Wineland, "Entangled states of trapped atomic ions," Nature **453**, 1008–1015 (2008).

[35] B. P. Lanyon, C. Hempel, D. Nigg, M. Müller, R. Gerritsma, F. Zähringer, P. Schindler, J. T. Barreiro, M. Rambach, G. Kirchmair, M. Hennrich, P. Zoller, R. Blatt, and C. F. Roos, "Universal digital quantum simulation with trapped ions," Science **334**, 57–61 (2011).

[36] F. Zähringer, G. Kirchmair, R. Gerritsma, E. Solano, R. Blatt, and C. F. Roos, "Realization of a quantum walk with one and two trapped ions," Phys. Rev. Lett. **104**, 100503 (2010).

[37] J. Casanova, L. Lamata, I. L. Egusquiza, R. Gerritsma, C. F. Roos, J. J. García-Ripoll, and E. Solano, "Quantum simulation of quantum field theories in trapped ions," Phys. Rev. Lett. **107**, 260501 (2011).

[38] R. Gerritsma, G. Kirchmair, F. Zähringer, E. Solano, R. Blatt, and C. F. Roos, "Quantum simulation of the dirac equation," Nature **463**, 68–71 (2010).

[39] T. Monz, P. Schindler, J. T. Barreiro, M. Chwalla, D. Nigg, W. A. Coish, M. Harlander, W. Hänsel, M. Hennrich, and R. Blatt, "14-qubit entanglement: Creation and coherence," Phys. Rev. Lett. **106**, 130506 (2011).

[40] R. Blatt and C. F. Roos, "Quantum simulations with trapped ions," Nature Phys. **8**, 277–284 (2012).

[41] L. D. Landau, "Über Die Bewegung der Elektronen in Kristallgitter," Phys. Z. Sowjetunion **3**, 644–645 (1933).

[42] L. D. Landau and S. I. Pekar, "Effective mass of a polaron," Zh. Eksp. Teor. Fiz. **18**, 419 (1948).

[43] H. Fröhlich, "Electrons in lattice fields," Adv. Phys. **3**, 325–361 (1954).

[44] R. P. Feynman, "Slow electrons in a polar crystal," Phys. Rev. **97**, 660–665 (1955).

[45] J. Devreese, *Moles agitat mentem : ontwikkelingen in de fysika van de vaste stof* (Technische Hogeschool Eindhoven, 1979).

[46] J. Kondo, "Resistance Minimum in Dilute Magnetic Alloys," Prog. Theor. Phys. **32**, 37–49 (1964).

[47] P. W. Anderson, "Infrared catastrophe in fermi gases with local scattering potentials," Phys. Rev. Lett. **18**, 1049–1051 (1967).

[48] A. P. Chikkatur, A. Görlitz, D. M. Stamper-Kurn, S. Inouye, S. Gupta, and W. Ketterle, "Suppression and enhancement of impurity scattering in a Bose-Einstein condensate," Phys. Rev. Lett. **85**, 483–486 (2000).

[49] P. Massignan, M. Zaccanti, and G. M. Bruun, "Polarons, dressed molecules and itinerant ferromagnetism in ultracold fermi gases," Rep. Prog. Phys. **77**, 034401 (2014).

[50] R. Schmidt, M. Knap, D. A. Ivanov, J.-S. You, M. Cetina, and E. Demler, "Universal many-body response of heavy impurities coupled to a fermi sea: a review of recent progress," Rep. Prog. Phys. **81**, 024401 (2018).

[51] M. Cetina, M. Jag, R. S. Lous, I. Fritsche, J. T. M. Walraven, R. Grimm, J. Levinsen, M. M. Parish, R. Schmidt, M. Knap, and E. Demler, "Ultrafast many-body interferometry of impurities coupled to a fermi sea," Science **354**, 96–99 (2016).

[52] S. P. Rath and R. Schmidt, "Field-theoretical study of the bose polaron," Phys. Rev. A **88**, 053632 (2013).

[53] Y. E. Shchadilova, R. Schmidt, F. Grusdt, and E. Demler, "Quantum dynamics of ultracold bose polarons," Phys. Rev. Lett. **117**, 113002 (2016).

[54] F. Grusdt, R. Schmidt, Y. E. Shchadilova, and E. Demler, "Strong-coupling bose polarons in a Bose-Einstein condensate," Phys. Rev. A **96**, 013607 (2017).

[55] R. Schmidt and M. Lemeshko, "Rotation of quantum impurities in the presence of a many-body environment," Phys. Rev. Lett. **114**, 203001 (2015).

[56] R. Schmidt and M. Lemeshko, "Deformation of a quantum many-particle system by a rotating impurity," Phys. Rev. X **6**, 011012 (2016).

[57] B. Midya, M. Tomza, R. Schmidt, and M. Lemeshko, "Rotation of cold molecular ions inside a Bose-Einstein condensate," Phys. Rev. A **94**, 041601 (2016).

[58] M. Lemeshko, "Quasiparticle approach to molecules interacting with quantum solvents," Phys. Rev. Lett. **118**, 095301 (2017).

[59] B. Shepperson, A. A. Søndergaard, L. Christiansen, J. Kaczmarczyk, R. E. Zillich, M. Lemeshko, and H. Stapelfeldt, "Laser-induced rotation of iodine molecules in helium nanodroplets: Revivals and breaking free," Phys. Rev. Lett. **118**, 203203 (2017).

[60] G. Bighin and M. Lemeshko, "Diagrammatic approach to orbital quantum impurities interacting with a many-particle environment," Phys. Rev. B **96**, 085410 (2017).

[61] G. Bighin, T. V. Tscherbul, and M. Lemeshko, "Diagrammatic monte carlo approach to angular momentum in quantum many-particle systems," Phys. Rev. Lett. **121**, 165301 (2018).

[62] E. Yakaboylu, M. Shkolnikov, and M. Lemeshko, "Quantum groups as hidden symmetries of quantum impurities," Phys. Rev. Lett. **121**, 255302 (2018).

[63] E. Yakaboylu, B. Midya, A. Deuchert, N. Leopold, and M. Lemeshko, "Theory of the rotating polaron: Spectrum and self-localization," Phys. Rev. B **98**, 224506 (2018).

[64] R. Côté, V. Kharchenko, and M. D. Lukin, "Mesoscopic molecular ions in Bose-Einstein condensates," Phys. Rev. Lett. **89**, 093001 (2002).

[65] K. S. Kleinbach, F. Engel, T. Dieterle, R. Löw, T. Pfau, and F. Meinert, "Ionic impurity in a Bose-Einstein condensate at submicrokelvin temperatures," Phys. Rev. Lett. **120**, 193401 (2018).

[66] G. E. Astrakharchik, L. A. P. Ardila, R. Schmidt, K. Jachymski, and A. Negretti, "Ionic polaron in a Bose-Einstein condensate," Comm. Phys. **4** (2021).

[67] T. Dieterle, M. Berngruber, C. Hölzl, R. Löw, K. Jachymski, T. Pfau, and F. Meinert, "Transport of a single cold ion immersed in a Bose-Einstein condensate," Phys. Rev. Lett. **126**, 033401 (2021).

[68] M. Cetina, A. T. Grier, and V. Vuletić, "Micromotion-induced limit to atom-ion sympathetic cooling in paul traps," Phys. Rev. Lett. **109**, 253201 (2012).

[69] M. Tomza, C. P. Koch, and R. Moszynski, "Cold interactions between an $Yb^+$ ion and a Li atom: Prospects for sympathetic cooling, radiative association, and Feshbach resonances," Phys. Rev. A **91**, 042706 (2015).

[70] J. Joger, H. Fürst, N. Ewald, T. Feldker, M. Tomza, and R. Gerritsma, "Observation of collisions between cold Li atoms and $Yb^+$ ions," Phys. Rev. A **96**, 030703 (2017).

[71] T. Schmid, C. Veit, N. Zuber, R. Löw, T. Pfau, M. Tarana, and M. Tomza, "Rydberg molecules for ion-atom scattering in the ultracold regime," Phys. Rev. Lett. **120**, 153401 (2018).

[72] A. D. Dörfler, P. Eberle, D. Koner, M. Tomza, M. Meuwly, and S. Willitsch, "Long-range versus short-range effects in cold molecular ion-neutral collisions," Nature Commun. **10** (2019), 10.1038/s41467-019-13218-x.

[73] H. Fürst, T. Feldker, N. V. Ewald, J. Joger, M. Tomza, and R. Gerritsma, "Dynamics of a single ion-spin impurity in a spin-polarized atomic bath," Phys. Rev. A **98**, 012713 (2018).

[74] R. J. Bartlett and M. Musiał, "Coupled-cluster theory in quantum chemistry," Rev. Mod. Phys. **79**, 291–352 (2007).

[75] P. J. Knowles, C. Hampel, and H. Werner, "Coupled cluster theory for high spin, open shell reference wave functions," J. Chem. Phys. **99**, 5219–5227 (1993).

[76] O. Christiansen, H. Koch, and P. Jo/rgensen, "Response functions in the cc3 iterative triple excitation model," J. Chem. Phys. **103**, 7429–7441 (1995).

[77] H. Koch, O. Christiansen, P. Jo/rgensen, A. M. Sanchez de Merás, and T. Helgaker, "The cc3 model: An iterative coupled cluster approach including connected triples," J. Chem. Phys. **106**, 1808–1818 (1997).

[78] T. Helgaker, S. Coriani, P. Jørgensen, K. Kristensen, J. Olsen, and K. Ruud, "Recent advances in wave function-based methods of molecular-property calculations," Chemical Reviews **112**, 543–631 (2012).

[79] W. Skomorowski, F. Pawłowski, C. P. Koch, and R. Moszynski, "Rovibrational dynamics of the strontium molecule in the $A^1\Sigma_u^+$, $c^3\Pi_u$, and $a^3\Sigma_u^+$ manifold from state-of-the-art ab initio calculations," J. Chem. Phys. **136**, 194306 (2012).

[80] M. Krych, W. Skomorowski, F. Pawłowski, R. Moszynski, and Z. Idziaszek, "Sympathetic cooling of the $Ba^+$ ion by collisions with ultracold Rb atoms: Theoretical prospects," Phys. Rev. A **83**, 032723 (2011).

[81] L. Landau and E. Lifshitz, *Mechanics: Volume 1*, t. 1 (Elsevier Science, 1982).

[82] R. Krems, B. Friedrich, and W. C. Stwalley, eds., *Cold Molecules* (CRC Press, 2009).

[83] L. Landau and E. Lifshitz, *Quantum Mechanics: Non-Relativistic Theory* (Elsevier Science, 2013).

[84] A. Messiah, *Quantum Mechanics* (Dover Publications, 2014).

[85] Z. Idziaszek, T. Calarco, P. S. Julienne, and A. Simoni, "Quantum theory of ultracold atom-ion collisions," Phys. Rev. A **79**, 010702 (2009).

[86] Z. Idziaszek, A. Simoni, T. Calarco, and P. S. Julienne, "Multichannel quantum-defect theory for ultracold atom–ion collisions," New J. Phys. **13**, 083005 (2011).

[87] T. V. Tscherbul, P. Brumer, and A. A. Buchachenko, "Spin-orbit interactions and quantum spin dynamics in cold ion-atom collisions," Phys. Rev. Lett. **117**, 143201 (2016).

[88] V. Barbé, A. Ciamei, B. Pasquiou, L. Reichsöllner, F. Schreck, P. S. Żuchowski, and J. M. Hutson, "Observation of Feshbach resonances between alkali and closed-shell atoms," Nature Phys. **14**, 881–884 (2018).

[89] S. Inouye, M. R. Andrews, J. Stenger, H.-J. Miesner, D. M. Stamper-Kurn, and W. Ketterle, "Observation of Feshbach res-

onances in a bose–einstein condensate," Nature **392**, 151–154 (1998).

[90] T. Köhler, K. Góral, and P. S. Julienne, "Production of cold molecules via magnetically tunable Feshbach resonances," Rev. Mod. Phys. **78**, 1311–1361 (2006).

[91] L. Tanzi, C. R. Cabrera, J. Sanz, P. Cheiney, M. Tomza, and L. Tarruell, "Feshbach resonances in potassium bose-bose mixtures," Phys. Rev. A **98**, 062712 (2018).

[92] H. Yang, D.-C. Zhang, L. Liu, Y.-X. Liu, J. Nan, B. Zhao, and J.-W. Pan, "Observation of magnetically tunable Feshbach resonances in ultracold $^{23}$Na$^{40}$K-$^{40}$K," Science **363**, 261–264 (2019).

[93] P. Weckesser, F. Thielemann, D. Wiater, A. Wojciechowska, L. Karpa, K. Jachymski, M. Tomza, T. Walker, and T. Schaetz, "Observation of Feshbach resonances between a single ion and ultracold atoms," Nature **600**, 429–433 (2021).

[94] M.-S. Heo, T. T. Wang, C. A. Christensen, T. M. Rvachov, D. A. Cotta, J.-H. Choi, Y.-R. Lee, and W. Ketterle, "Formation of ultracold fermionic NaLi Feshbach molecules," Phys. Rev. A **86**, 021602 (2012).

[95] S. B. Papp and C. E. Wieman, "Observation of heteronuclear Feshbach molecules from a $^{85}$Rb $-^{87}$ Rb gas," Phys. Rev. Lett. **97**, 180404 (2006).

[96] G. Thalhammer, K. Winkler, F. Lang, S. Schmid, R. Grimm, and J. H. Denschlag, "Long-lived Feshbach molecules in a three-dimensional optical lattice," Phys. Rev. Lett. **96**, 050402 (2006).

[97] C.-H. Wu, J. W. Park, P. Ahmadi, S. Will, and M. W. Zwierlein, "Ultracold fermionic Feshbach molecules of $^{23}$Na$^{40}$**K**," Phys. Rev. Lett. **109**, 085301 (2012).

[98] A. Chotia, B. Neyenhuis, S. A. Moses, B. Yan, J. P. Covey, M. Foss-Feig, A. M. Rey, D. S. Jin, and J. Ye, "Long-lived dipolar molecules and Feshbach molecules in a 3d optical lattice," Phys. Rev. Lett. **108**, 080405 (2012).

[99] T. Kraemer, M. Mark, P. Waldburger, J. G. Danzl, C. Chin, B. Engeser, A. D. Lange, K. Pilch, A. Jaakkola, H.-C. Nägerl, and R. Grimm, "Evidence for efimov quantum states in an ultracold gas of caesium atoms," Nature **440**, 315–318 (2006).

[100] P. Naidon and S. Endo, "Efimov physics: a review," Rep. Prog. Phys. **80**, 056001 (2017).

[101] P. Massignan and H. T. C. Stoof, "Efimov states near a Feshbach resonance," Phys. Rev. A **78**, 030701 (2008).

[102] S. Knoop, F. Ferlaino, M. Mark, M. Berninger, H. Schöbel, H.-C. Nägerl, and R. Grimm, "Observation of an efimov-like trimer resonance in ultracold atom–dimer scattering," Nature Phys. **5**, 227–230 (2009).

[103] M. H. Anderson, J. R. Ensher, M. R. Matthews, C. E. Wieman, and E. A. Cornell, "Observation of Bose-Einstein condensation in a dilute atomic vapor," Science **269**, 198–201 (1995).

[104] C. C. Bradley, C. A. Sackett, J. J. Tollett, and R. G. Hulet, "Evidence of Bose-Einstein condensation in an atomic gas with attractive interactions," Phys. Rev. Lett. **75**, 1687–1690 (1995).

[105] G. Modugno, G. Ferrari, G. Roati, R. J. Brecha, A. Simoni, and M. Inguscio, "Bose-Einstein condensation of potassium atoms by sympathetic cooling," Science **294**, 1320–1322 (2001).

[106] S. L. Cornish, N. R. Claussen, J. L. Roberts, E. A. Cornell, and C. E. Wieman, "Stable $^{85}$Rb Bose-Einstein condensates with widely tunable interactions," Phys. Rev. Lett. **85**, 1795–1798 (2000).

[107] K. B. Davis, M. O. Mewes, M. R. Andrews, N. J. van Druten, D. S. Durfee, D. M. Kurn, and W. Ketterle, "Bose-Einstein condensation in a gas of sodium atoms," Phys. Rev. Lett. **75**, 3969–3973 (1995).

[108] D. G. Fried, T. C. Killian, L. Willmann, D. Landhuis, S. C. Moss, D. Kleppner, and T. J. Greytak, "Bose-Einstein condensation of atomic hydrogen," Phys. Rev. Lett. **81**, 3811–3814 (1998).

[109] A. Robert, O. Sirjean, A. Browaeys, J. Poupard, S. Nowak, D. Boiron, C. I. Westbrook, and A. Aspect, "A Bose-Einstein condensate of metastable atoms," Science **292**, 461–464 (2001).

[110] T. Weber, J. Herbig, M. Mark, H.-C. Nägerl, and R. Grimm, "Bose-Einstein condensation of cesium," Science **299**, 232–235 (2003).

[111] V. Barbé, A. Ciamei, B. Pasquiou, L. Reichsöllner, F. Schreck, P. S. Żuchowski, and J. M. Hutson, "Observation of Feshbach resonances between alkali and closed-shell atoms," Nature Phys. **14**, 881–884 (2018).

[112] T. G. Tiecke, M. R. Goosen, J. T. M. Walraven, and S. J. J. M. F. Kokkelmans, "Asymptotic-bound-state model for Feshbach resonances," Phys. Rev. A **82**, 042712 (2010).

[113] B. R. Johnson, "The renormalized numerov method applied to calculating bound states of the coupled-channel schroedinger equation," J. Chem. Phys. **69**, 4678–4688 (1978).

[114] C. Ticknor, C. A. Regal, D. S. Jin, and J. L. Bohn, "Multiplet structure of Feshbach resonances in nonzero partial waves," Phys. Rev. A **69**, 042712 (2004).

[115] Y. Cui, C. Shen, M. Deng, S. Dong, C. Chen, R. Lü, B. Gao, M. K. Tey, and L. You, "Observation of broad d-wave Feshbach resonances with a triplet structure," Phys. Rev. Lett. **119**, 203402 (2017).

[116] W. D. Phillips and H. Metcalf, "Laser deceleration of an atomic beam," Phys. Rev. Lett. **48**, 596–599 (1982).

[117] D. E. Pritchard, "Cooling neutral atoms in a magnetic trap for precision spectroscopy," Phys. Rev. Lett. **51**, 1336–1339 (1983).

[118] W. D. Phillips, "Nobel lecture: Laser cooling and trapping of neutral atoms," Rev. Mod. Phys. **70**, 721–741 (1998).

[119] D. J. Wineland and W. M. Itano, "Laser cooling of atoms," Phys. Rev. A **20**, 1521–1540 (1979).

[120] T. Hänsch and A. Schawlow, "Cooling of gases by laser radiation," Opt. Commun. **13**, 68–69 (1975).

[121] G. Reinaudi, C. B. Osborn, K. Bega, and T. Zelevinsky, "Dynamically configurable and optimizable zeeman slower using permanent magnets and servomotors," J. Opt. Soc. Am. B **29**, 729–733 (2012).

[122] I. Courtillot, A. Quessada, R. P. Kovacich, J.-J. Zondy, A. Landragin, A. Clairon, and P. Lemonde, "Efficient cooling and trapping of strontium atoms," Opt. Lett. **28**, 468–470 (2003).

[123] F. Schreck and K. van Druten, "Laser cooling for quantum gases," Nature Phys. **17**, 1296–1304 (2021).

[124] D. M. Stamper-Kurn, M. R. Andrews, A. P. Chikkatur, S. Inouye, H.-J. Miesner, J. Stenger, and W. Ketterle, "Optical confinement of a Bose-Einstein condensate," Phys. Rev. Lett. **80**, 2027–2030 (1998).

[125] W. Paul, "Electromagnetic traps for charged and neutral particles," Rev. Mod. Phys. **62**, 531–540 (1990).

[126] D. Leibfried, R. Blatt, C. Monroe, and D. Wineland, "Quantum dynamics of single trapped ions," Rev. Mod. Phys. **75**, 281–324 (2003).

[127] S. Chu and C. Wieman, "Laser cooling and trapping of atoms," J. Opt. Soc. Am. B **6**, 2020–2288 (1989).

[128] H. F. Hess, "Evaporative cooling of magnetically trapped and compressed spin-polarized hydrogen," Phys. Rev. B **34**, 3476–3479 (1986).

[129] W. Ketterle and N. V. Druten, "Evaporative cooling of trapped atoms," Adv. At. Mol. Opt. Phys., **37**, 181–236 (1996).

[130] E. L. Raab, M. Prentiss, A. Cable, S. Chu, and D. E. Pritchard, "Trapping of neutral sodium atoms with radiation pressure," Phys. Rev. Lett. **59**, 2631–2634 (1987).

[131] R. Grimm, M. Weidemüller, and Y. B. Ovchinnikov, "Optical dipole traps for neutral atoms," in *Adv. At. Mol. Opt. Phys.* (Elsevier, 2000) pp. 95–170.

[132] S. Schmid, A. Härter, and J. H. Denschlag, "Dynamics of a cold trapped ion in a Bose-Einstein condensate," Phys. Rev. Lett. **105**, 133202 (2010).

[133] D. J. Berkeland, J. D. Miller, J. C. Bergquist, W. M. Itano, and D. J. Wineland, "Minimization of ion micromotion in a paul trap," J. Appl. Phys. **83**, 5025–5033 (1998).

[134] H. Hirzler, T. Feldker, H. Fürst, N. V. Ewald, E. Trimby, R. S. Lous, J. D. Arias Espinoza, M. Mazzanti, J. Joger, and R. Gerritsma, "Experimental setup for studying an ultracold mixture of trapped $\mathrm{Yb}^{+}$–$^{6}\mathrm{Li}$," Phys. Rev. A **102**, 033109 (2020).

[135] T. Feldker, H. Fürst, H. Hirzler, N. V. Ewald, M. Mazzanti, D. Wiater, M. Tomza, and R. Gerritsma, "Buffer gas cooling of a trapped ion to the quantum regime," Nature Phys. **16**, 413–416 (2020).

[136] J. Schmidt, P. Weckesser, F. Thielemann, T. Schaetz, and L. Karpa, "Optical traps for sympathetic cooling of ions with ultracold neutral atoms," Phys. Rev. Lett. **124**, 053402 (2020).

[137] A. Lambrecht, J. Schmidt, P. Weckesser, M. Debatin, L. Karpa, and T. Schaetz, "Long lifetimes and effective isolation of ions in optical and electrostatic traps," Nature Photon. **11**, 704–707 (2017).

[138] J. Schmidt, A. Lambrecht, P. Weckesser, M. Debatin, L. Karpa, and T. Schaetz, "Optical trapping of ion coulomb crystals," Phys. Rev. X **8**, 021028 (2018).

[139] P. Langevin, "Une formule fondamentale de théorie cinétique," Ann. Chim. et Physique **5**, 245 (1905).

[140] B. Gao, "Universal properties in ultracold ion-atom interactions," Phys. Rev. Lett. **104**, 213201 (2010).

[141] R. J. Le Roy, Y. Huang, and C. Jary, "An accurate analytic potential function for ground-state n2 from a direct-potential-fit analysis of spectroscopic data," J. Chem. Phys. **125**, 164310 (2006).

[142] I. Rouse and S. Willitsch, "Superstatistical energy distributions of an ion in an ultracold buffer gas," Phys. Rev. Lett. **118**, 143401 (2017).

[143] Z. Meir, T. Sikorsky, R. Ben-shlomi, N. Akerman, Y. Dallal, and R. Ozeri, "Dynamics of a ground-state cooled ion colliding with ultracold atoms," Phys. Rev. Lett. **117**, 243401 (2016).

[144] R. G. DeVoe, "Power-law distributions for a trapped ion interacting with a classical buffer gas," Phys. Rev. Lett. **102**, 063001 (2009).

[145] I. Rouse and S. Willitsch, "Energy distributions of an ion in a radio-frequency trap immersed in a buffer gas under the influence of additional external forces," Phys. Rev. A **97**, 042712 (2018).

[146] C. Tsallis, "Possible generalization of boltzmann-gibbs statistics," J. Stat. Phys. **52**, 479–487 (1988).

[147] A. Derevianko, "Anisotropic pseudopotential for polarized dilute quantum gases," Phys. Rev. A **67**, 033607 (2003).

[148] A. Derevianko, "Revised huang-yang multipolar pseudopotential," Phys. Rev. A **72**, 044701 (2005).

[149] Z. Idziaszek, "Analytical solutions for two atoms in a harmonic trap: p-wave interactions," Phys. Rev. A **79**, 062701 (2009).

[150] K. Kanjilal, J. L. Bohn, and D. Blume, "Pseudopotential treatment of two aligned dipoles under external harmonic confinement," Phys. Rev. A **75**, 052705 (2007).

[151] X. Y. Yin, S. Gopalakrishnan, and D. Blume, "Harmonically trapped two-atom systems: Interplay of short-range $s$-wave interaction and spin-orbit coupling," Phys. Rev. A **89**, 033606 (2014).

[152] Q. Guan, X. Y. Yin, S. E. Gharashi, and D. Blume, "Energy spectrum of a harmonically trapped two-atom system with spin–orbit coupling," J. Phys. B: At. Mol. Opt. Phys. **47**, 161001 (2014).